MICHELE SPADA
PHD THESIS 2015

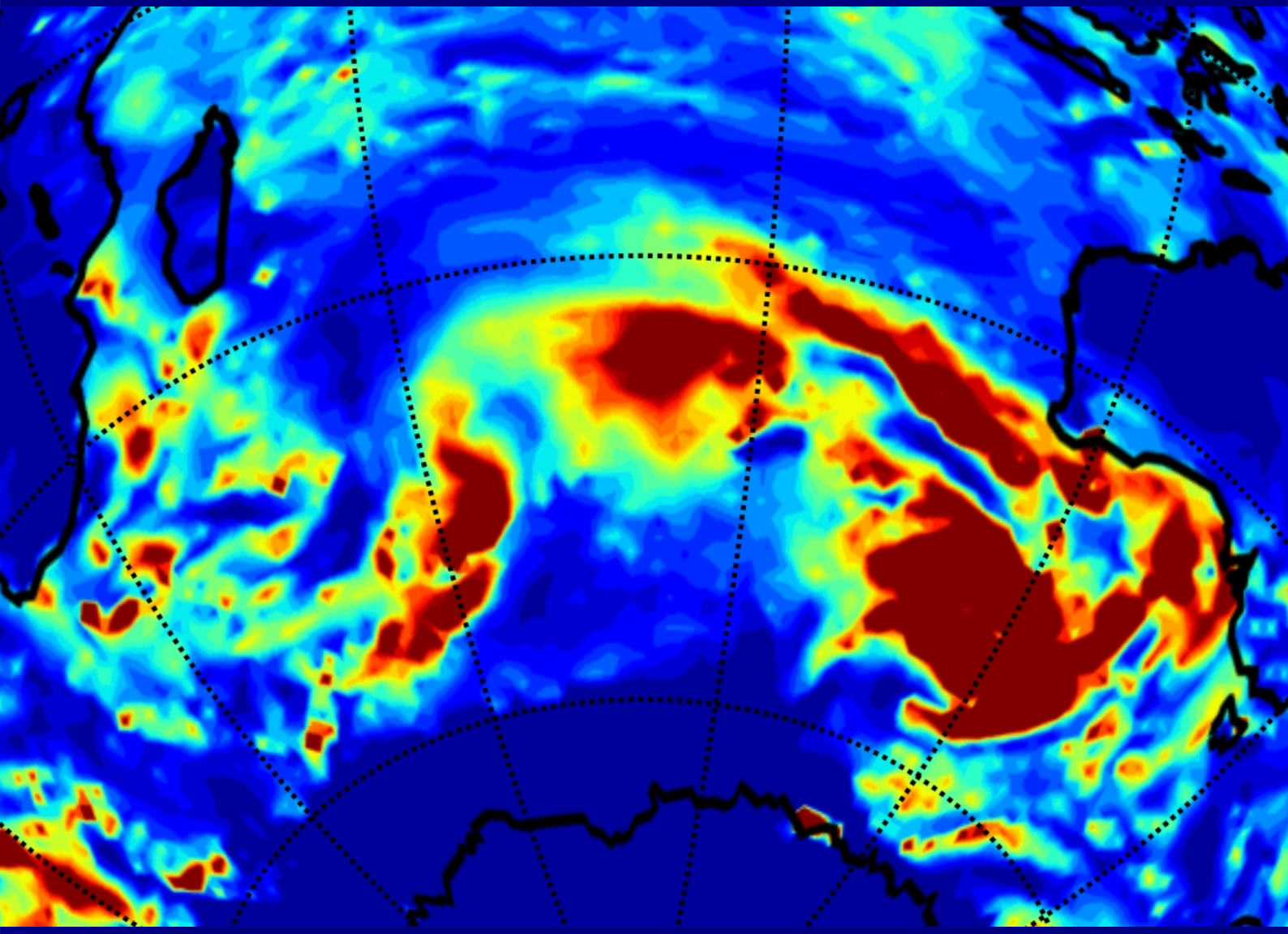

DEVELOPMENT AND EVALUATION OF AN ATMOSPHERIC AEROSOL MODULE IMPLEMENTED WITHIN THE NMMB/BSC-CTM

Cover image: global sea-salt surface concentration simulated by the NMMB/BSC-CTM from a Roaring Forties' point of view.

UNIVERSITAT POLITÈCNICA
DE CATALUNYA
BARCELONATECH

Barcelona
Supercomputing
Center
Centro Nacional de Supercomputación

UNIVERSITAT POLITÈCNICA DE CATALUNYA
INSTITUT DE SOSTENIBILITAT
PROGRAMA DE DOCTORAT EN ENGINYERIA AMBIENTAL

DEVELOPMENT AND EVALUATION OF AN ATMOSPHERIC AEROSOL MODULE IMPLEMENTED WITHIN THE NMMB/BSC-CTM

Memòria presentada per Michele Spada
per optar al títol de Doctor per la Universitat Politècnica de Catalunya

Treball realitzat en el Barcelona Supercomputing Center

Michele Spada
Setembre del 2015

Doctorant	*Director*	*Director*
Michele Spada	*Oriol Jorba*	*Jose Maria Baldasano*

This thesis has been achieved under the external advice of:

Carlos Pérez García-Pando

NASA-Goddard Institute for Space Studies, NY, USA
Dep. of App. Phys. and App. Math., Columbia Univ., NY, USA

A mio papà Piero

Acknowledgements

En primer lugar quiero agradecer al Oriol, por su apoyo científico y humano. Por haberse gastado sus vacaciones para viajar a Roma y ayudarme con la maldida química del sulfato. Y por haberme encontrado piso en Barcelona en los tiempos difíciles (gracias también a Ester!).

Agradezco al Carlos, por haberme enseñado todo lo que sé (y otras cosas que todavía no he entendido) sobre los aerosoles.

I acknowledge Zavisa Janjic to develop the NMMB during the years, all my thesis is based on your Work. It is true that we are dwarves on the shoulders of Giants (like you).

Agradezco a Jose Maria Baldasano por su apoyo como director de mi tesis y a Santiago Gassó por el apoyo logístico.

I would like to thank the researchers which collaborate to the model development, Kostas Tsigaridis (Columbia Univ.) and Joana Soares (Finnish Meteorological Institute).

Tambien agradezco a los científicos con los cuales he tenido la grande oportunidad de hablar en Barcelona, que me han enseñado mucho y que mucho han aportado a este trabajo: Marco Pandolfi (*fondamentale!*), Xavier Querol, Andrés Alastuey, Mari Cruz Minguillón, Antonis Gkikas, Arnau Folch, Pedro Jimenez y Enric Tarradellas.

I acknowledge Slobodan Nickovic, Yuhan Lee, and Paul Ginoux for the precious conversations on the aerosol modeling. I thank the researchers providing the aerosol measurements and model intercomparison studies used in this work, Michael Schulz (AEROCOM/EBAS-NILU), John Prospero (University of Miami), Andrew Tait (NIWA), and the scientists of the the AERONET Program, the MODIS and MISR satellites, the South African Weather Service, the IMPROVE, EMEP, EANET, NOAA ESRL-GMD, and DOE-ARM Networks.

Agradezco a mis compañeros de trabajo por el apoyo, la paciencia con mis bromas y los desayunos slow-food: Kasten, Angel, Sara, Maria Teresa, Vincenzo, Francesc, Montse y todos los otros que me olvido.

Unas gracias particulares van a mi familia Barcelonesa, que he tenido la suerte de encontrar y que ha cuidado de mi en todo este tiempo: el Jordi Comas, Enric Lleopart y el Josep Pastor, Alba (mi germaneta), Simone, Amparo, Rocío, Gisnena, los Francescos, Valentina y Super-Enza. Gracias a Enza para revisarme el inglés (y el manuscrito!), a Amparo para traducirme al español, y a Francesco para ayudarme con el Python!

Thanks to Roger Ridley who accompanied me with his songs.

Ringrazio gli amici di Roma che ho "abbandonato" per intraprendere l'avventura Barcellonese ma che la distanza non ha allontanato: Andrea, Matteo, Andrea Romano, Giulia, Stefano (tutta la Sezione Camilla Ravera!) e tanti altri che per la fretta mi dimentico e si arrabbieranno. Ringrazio Sandro Finardi e Roberto Sozzi per avermi fatto appassionare ai modelli atmosferici.

Un ringraziamento speciale va alla Prof. Renzi, che tanto ha sempre creduto nelle mie capacità (speriamo che abbia ben riposto la sua fiducia).

Ultimi ma buoni, ringrazio la mia famiglia allargata: papà Piero, mamma Rita, mio fratello Stefano, i miei nonni e i miei zii/cugini Spada/Bucci, Zio Lillo e Cristiana, Elio e Empiria, Riccardo, i nonni Pietro e Petrina, il gatto Tonino, gli zii Paoli e Barbara.

Valeria e Grenyas sono sempre al mio fianco, anche mentre scrivo adesso.

"The future is unwritten"
(Joe Strummer)

Abstract

This PhD Thesis presents and discusses the developments of a hybrid sectional-bulk multi-component aerosol module coupled with the multiscale chemical weather prediction system NMMB/BSC-CTM. The module is designed to provide short and medium range forecast of the atmospheric aerosols for a wide range of scales (from global to regional) and applications (from the simulation of the aerosol-radiation interaction to the study of air pollution). The module represents the processes controlling the life cycle of dust, sea-salt, black carbon, organic matter (both primary and secondary), and sulfate aerosols. The dust module was previously implemented in the model and it can be considered the starting point of this work. For the production of secondary organic aerosol, a 2-product scheme was implemented in the model. A simplified gas-aqueous-aerosol mechanism was introduced in the module to account for the sulfur chemistry. The module also accounts for the hydrophobic-to-hydrophilic conversion of carbonaceous aerosols.

In a first step, we implemented the sea-salt aerosol module and we compared global simulations using five state-of-the-art open-ocean emission schemes with AOD measurements from selected AERONET sun photometers, surface concentration measurements from the University of Miami's Ocean Aerosol Network, and measurements from two NOAA/PMEL cruises. The sea-salt global distribution was found to be highly sensitive to the introduction of SST-dependent emissions and to the accounting of spume particles production. Our results indicate that SST-dependent emission schemes improve the overall model performance in reproducing surface concentrations. On the other hand, they lead to an overestimation of the coarse AOD at tropical latitudes.

Since we found that our global simulations of the sea-salt distribution in orographic/coastal regions are affected by positive biases (regardless of the source function applied), we investigated the effect of high model resolution (0.1°x0.1° vs. 1°x1.4°) upon sea-salt patterns in four stations from the University of Miami Network: Baring Head, Chatam Island, and Invercargill in New Zealand, and Marion Island in the sub-antarctic Indian Ocean. We found that normalized biases improved and correlation increased compared to the use of a lower resolution. In particular we found that the representation of sea/land interfaces, mesoscale circulations, and precipitation with the higher resolution model played a major role in the simulation of annual concentration trends. Our results recommend caution when comparing or constraining global models using surface concentration observations from coastal stations.

In a second step, we implemented carbonaceous and sulfate aerosols and we performed a benchmark experiment at global scale by applying emissions from the AEROCOM-ACCMIP dataset together with online biogenic emissions from the MEGAN model. The biomass-burning emissions were injected in the vertical model layers according to the satellite-derived climatologies of the IS4FIRES algorithm. The results were evaluated with observations from several networks, both for surface concentrations and optical depth (AERONET and satellites). We found that the model scores lie in the higher part of the range provided by the global models involved in the AEROCOM and ACCMIP studies. The main sources of uncertainty affecting our global results can be identified with the estimates of biomass-burning emissions and with the size distribution applied to the dust aerosol at the emission.

Abstract (Spanish version)

Se ha desarrollado un módulo de aerosoles acoplado con el modelo multiescala de predicción atmosférica NMMB/BSC-CTM. El módulo está diseñado para producir predicciones a corto y medio alcance de los aerosoles atmosféricos para un amplio rango de escalas (de global a regional y urbana) y de aplicaciones (desde la simulación de la interacción aerosol-radiación al estudio de la contaminación del aire). El módulo describe los procesos que caracterizan el ciclo de vida del polvo mineral, de la sal marina, del carbono negro, del carbono orgánico y del sulfato. Para describir la producción de aerosoles orgánicos secundarios se ha implementado en el modelo un esquema de dos productos; mientras que para representar la química del azufre se ha introducido un mecanismo simplificado gas-acuoso-aerosol.

En primer lugar, se ha implementado un modulo para el aerosol de sal marina empleando cinco esquemas de emisiones en océano abierto y se han comparado simulaciones globales con medidas de AOD observadas por fotómetros de la red AERONET, con medidas de concentración en superficie de la Red de Aerosoles Oceánicos de la Universidad de Miami, y con medidas de dos buques oceanográficos de NOAA/PMEL. Los resultados son altamente sensibles a la introducción en el modelo de esquemas de emisión dependientes de la temperatura de la SST y de la producción de partículas de espuma. Los resultados indican que el uso de esquemas de emisión dependientes de la SST mejora el rendimiento del modelo en su capacidad de reproducir las concentraciones en superficie. Por otro lado, estos esquemas conducen a una sobrestimación de la fracción gruesa de la AOD en latitudes tropicales.

Para investigar los errores encontrados en regiones costeras o caracterizadas por fuertes gradientes de orografía, se ha investigado también el efecto de trabajar a una alta resolución ($0.1°$x$0.1°$ vs $1°$x$1.4°$) sobre los patrones de sal marina en correspondencia con cuatro estaciones de la Red de la Universidad de Miami: Baring Head, Isla Chatam y Invercargill en Nueva Zelanda, y Isla Marion en el Océano Índico sub-antártico. Se ha encontrado que al aumentar de la resolucíon espacial, los errores disminuyen y la correlación aumenta. En particular la representación de la interfaz mar/tierra, las circulaciones a mesoescala y las precipitaciones con el modelo de alta resolución juegan un papel principal en la simulación de las concentraciónes anuales. Nuestros resultados recomiendan cautela al comparar o constreñir modelos globales empleando concentraciones en superficie observadas en estaciones costeras.

En un segundo paso se han implementado los aerosoles carbonosos y el sulfato. Se ha efectuado un experimento de referencia a escala global, aplicando emisiones de la base de datos de AEROCOM-ACCMIP junto con emisiones biogénicas online del modelo MEGAN. Las emisiones de quema de biomasa se han inyectado en las capas verticales del modelo, de acuerdo con la climatología derivada de satélites por el IS4FIRES. Los resultados han sido evaluados con observaciones procedentes de varias redes, tanto para concentraciones en superficie como para el espesor óptico (AERONET y satélites). Se ha encontrado que el modelo se desempeña en la parte alta del rango proporcionado por los modelos globales involucrados en los estudios de AEROCOM y ACCMIP. Las principales fuentes de incertidumbre que afectan los resultados globales se pueden identificar con las estimaciones de emisiones de quema de biomasa y con la distribución en tamaño aplicada al polvo mineral durante su proceso de emisión.

Publications derived from the thesis

- Spada, M., Jorba, O., Pérez García-Pando, C., Janjic, Z., and Baldasano, J. M.: Modeling and evaluation of the global sea-salt aerosol distribution: sensitivity to size-resolved and sea-surface temperature dependent emission schemes, Atmos. Chem. Phys., 13, 11735–11755, doi:10.5194/acp-13-11735-2013, 2013.
- Spada, M., Jorba, O., Pérez García-Pando, C., Janjic, Z., and Baldasano, J. M.: On the evaluation of global sea-salt aerosol models at coastal/orographic sites, Atmos. Env., 101, 41–48, doi:10.1016/j.atmosenv.2014.11.019, 2015.
- Spada, M., Jorba, O., Pérez García-Pando, C., Tsigaridis, K., Soares, J., and Janjic, Z.: Global aerosols in the online multiscale NMMB/BSC Chemical Transport Model, in preparation for Geosci. Model Dev.

Other publications related to the PhD studies:

- Jorba, O., Dabdub, D., Blaszczak-Boxe, C., Pérez, C., Janjic, Z., Baldasano, J. M., Spada, M., Badia, A., and Gonçalves, M.: Potential significance of photoexcited NO2 on global air quality with the NMMB/BSC chemical transport model, J. Geophys. Res., 117, D13301, doi:10.1029/2012JD017730, 2012.
- Jorba, O., Pandolfi, M., Spada, M., Baldasano, J. M., Pey, J., Alastuey, A., Arnold, D., Sicard, M., Artiñano, B., Revuelta, M. A., and Querol, X.: Overview of the meteorology and transport patterns during the DAURE field campaign and their impact to PM observations, Atmos. Env., 77, 607–620, doi:10.1016/j.atmosenv.2013.05.040, 2013.
- Jorba, O., Pérez, C., Haustein, K., Janjic, Z., Baldasano, J. M., Dabdub, D., Badia, A., and Spada, M.: Multiscale Air Quality with the NMMB/BSC Chemical Transport Model. Chapter of "Air Pollution Modeling and its Application XXII", Part of the series NATO Science for Peace and Security Series C: Environmental Security pages 315–320. Edited by Steyn, D. G., Builtjes, P., Timmermans, J. H., and Renske, M.A., ISBN 978-94-007-5577-2, 2013.

Contents

List of acronyms

ACCMIP Atmospheric Chemistry and Climate Model Intercomparison Project
ACE1 first Aerosol Characterization Experiment
AEROCOM AEROsol model interCOMparison initiative
AEROINDOEX AEROsolS99 and INDian Ocean EXperiment
AERONET AEROsol RObotics NETwork
AOD Aerosol Optical Depth
BSC-CTM Barcelona Supercomputing Center Chemical Transport Model
CTM Chemical Transport Model
EANET Acid Deposition Monitoring in East Asia
EMEP European Monitoring and Evaluation Programme
GCM Global Climate Model
ICAP International Cooperative for Aerosol Prediction
IMPROVE Interagency Monitoring of Protected Visual Environments
IS4FIRES Integrated monitoring and modelling System For wildland FIRES
MEGAN Model of Emissions of Gases and Aerosols from Nature
NCEP National Centers for Environmental Prediction
NIWA National Institute of Water and Atmospheric research
NOAA National Oceanic and Atmospheric Administration
NMMB Non-hydrostatic Multiscale Model on the B-grid
POA Primary Organic Aerosol
POC Primary Organic Carbon
PM Particulate Matter
PM2.5 Particulate Matter with diameter lesser or equal to $2.5\mu m$
PM10 Particulate Matter with diameter lesser or equal to $10\mu m$
PMEL Pacific Marine Environmental Laboratory
SOA Secondary Organic Aerosol
SOC Secondary Organic Carbon
SST Sea Surface Temperature
SWAS South African Weather Service
UMIAMI University of Miami Oceanic Aerosol Network
VOC Volatile Organic Compound

Acronyms defined by the author and frequently used in the manuscript†:

BC Black Carbon
DU mineral DUst
EC Elemental Carbon
OC Organic Carbon
OA Organic Aerosol
SS Sea-Salt
SU SUlfate

† other specific acronyms are defined in the text.

Chapter 1 – Introduction

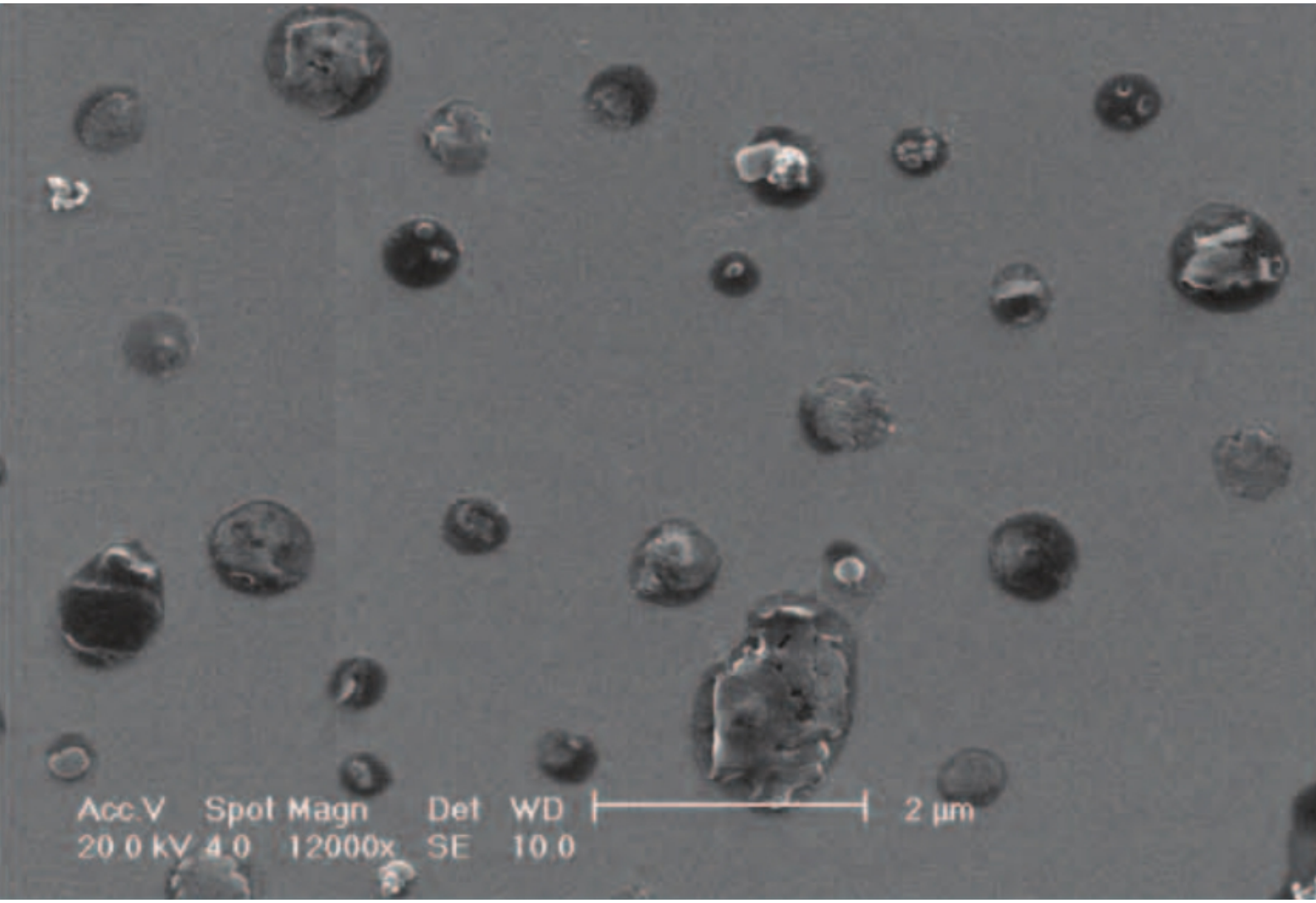

SEM image of particles collected during a transport event at Mexico City.
Photo credits: Moffet et al., 2010 (Atmos. Chem. Phys., 10)

1 Introduction

Aerosols play an important role in the prediction of the Earth's environment (IPCC, 2013). Understanding atmospheric aerosol processes is crucial for the investigations of issues related to climate, air quality and health, aviation (visibility), radiative forcings, and clouds. Also, there is evidence that the inclusion of the aerosol radiative effects in Numerical Weather Prediction (NWP) models may lead to an improvement of both short and medium range forecasts (Pérez et al., 2006; Sessions et al., 2015). Strong uncertainties still affect the simulation of the aerosol life-cycles. Major sources of uncertainty include emissions (Textor et al., 2007) and wet deposition (Prospero et al., 2010; Schulz et al., 2012), although relevant uncertainties are related to the secondary production of aerosols (Tsigaridis et al., 2014), and to the influence of the model scales (Spada et al., 2013). Some of the recent efforts by the aerosol modeling community have focused on intercomparison studies including most of the state-of-the-art models. Examples are the experiments performed in the AEROCOM (Textor et al., 2006, 2007; Kinne et al., 2006; Tsigaridis et al., 2014) and ACCMIP (Shindell et al., 2013; Lee et al., 2013) frameworks, the ICAP (Sessions et al., 2015) initiative at global scale, and the Air Quality Model Evaluation International Initiative (AQMEII) at regional scale (Solazzo et al., 2012) among others. Despite the large variety of parameterizations included in models, and their different level of complexity, these studies have found model errors of a factor of two (or more) in the simulation of aerosol concentration and optical depth (AOD), with consequent implications on the simulation of radiative effects. Aerosol modules are typically coupled to GCMs, which often work on long-term predictions at coarse resolution by applying an approximation of hydrostatic atmosphere (e.g. the ECHAM-HAM model (Stier et al., 2005)) and to short/medium term weather forecast models, in order to provide air quality applications by using CTMs (e.g. the CMAQ model (Binkowski and Roselle, 2003)). As a consequence, aerosol modules work at global or regional scales, depending on the scales solved by the meteorological driver model. There have been also some efforts to bridge the gap (and relative uncertainties) between the scales involved by global and regional models. In this sense, only few multiscale models are currently available, such as the PNNL-MMF (Wang et al., 2011), the GEM-AQ/EC (Gong et al., 2012), the GU-WRF/Chem (Zhang et al., 2012c), and the ICON-ART (Rieger et al., 2015).

1.1 State-of-the-art of the aerosol modeling

The compilation of an exhaustive review of the state-of-the-art is challenging because of the incessant activity of the modeling community in the development of new parameterizations, new models, and model upgrades. Here we present a review of key processes and parameterizations, with the aim to illustrate the large variety of approaches used by models. The main characteristics of a number of aerosol models, both GCMs and CTMs, are highlighted in Table 1.

Prognostic variables. In the literature, we found that the aerosol transport equations are solved for both number and mass concentrations or only for mass concentrations, depending on the modeling focus. GCMs typically predict both number and mass, in order to simulate both direct and indirect radiative effects. Note that the use of prognostic number concentrations requires a treatment of particles' coagulation, which is often neglected by models which only predict the aerosol mass.

Microphysics. A key feature of aerosol models is given by the ability to solve global and/or regional scales. A second key feature is provided by the approach to represent the aerosol microphysics, i.e. size distribution, mixing state, and particles' geometry. The size distribution can be described by applying modal, sectional, or bulk representations. The modal approach is computationally efficient and allows the prediction of number concentrations (and thus, the simulation of the aerosol-cloud effects in climate models). However, it has been shown that the small number of modes (nucleation, Aitken, accumulation, and coarse) may lead to a lower accuracy in the simulation of the aerosol life-cycle with respect to the sectional approach (Zhang et al., 1999; Zhang, 2002). Sectional/modal approaches involving only one single bin/mode are considered equivalent to bulk representations.

Experimental observations show that primary particles are externally mixed close to their sources (Textor et al., 2006), but can become internally mixed by coagulation with other particles or by condensation of gases on their surfaces. Most models assume either completely externally or internally mixed state aerosols, while a small number of them work both with externally and internally mixed particles (e.g. MPI-HAM, see Stier et al. (2005)). Usually, models do not account for external-to-internal mixing conversion. Typically aerosols are parameterized as homogeneous spheres, although the assumption of spherical particles may be unrealistic for some particles (for example chain-like soot particles) (Zhang, 2008). The representation of aerosol microphysics can strongly influence the aerosol optical properties and a number of aerosol processes, such as the particles' scavenging or more generally aerosol-cloud interactions (Zhang, 2002, 2008).

Chemical mechanism and secondary formation. Models can be coupled on-line or off-line with a gas-phase chemical mechanism. On-line models are able to describe feedback processes between aerosol and gas phase photochemistry, and a fully prognostic treatment of the chemical reactions involved in the formation of secondary aerosols, such as sulfate and secondary organic aerosol. However, most global models include sulfur and SOA chemical schemes that are uncoupled with the gas-phase chemistry of oxidants, (i.e. they apply prescribed off-line concentrations of oxidants).
The gas-phase sulfur chemistry is characterized by the production of sulfuric acid due to oxidation of SO_2 and Dimethyl Sulfide (DMS) (Barth et al., 2000; Tie et al., 2001). The gaseous sulfuric acid can either nucleate new aerosol particles or condensate onto pre-existent particles, and finally dissociate into sulfate. The homogeneous nucleation process is often neglected in CTMs (see Textor et al. (2006)).

The aqueous phase sulfur chemistry involves equilibrium reactions for SO_2, H_2O_2, and O_3. While SO_2 (and H_2O_2 in some models, see for ex. Koch et al. (2006) and Goto et al. (2011)) is usually transported by global models, O_3 is assumed as an off-line field in most of them. The transport of aqueous species is predicted by regional Air Quality Models (AQMs) but neglected in most of the global models. In most of the global aerosol models, the dissolved species are returned to the cloud-free portion of the grid box after each cloud time step (see for ex. Koch et al. (1999)). However Koch et al. (2003) found that the use of a dissolved species budget scheme results in a decreased sulfate burden since the parameterization allowed more precipitation scavenging.

The gas/particle partitioning is described by applying a wide range of parameterizations, ranging from simplified approaches (assuming that all the sulfuric acid is avalaible to instantaneously condense into sulfate aerosol, as in Chin et al. (2002)), to the use of thermodinamic

equilibrium modules (such as ISORROPIA (Fontoukis and Nenes, 2007) or EQSAM (Metzger et al., 2002) among others), up to dynamical parameterizations (see for ex. Vignati et al. (2004)).

SOA formation can also be parameterized with a large variety of schemes with different levels of complexity (for an exhaustive review see Kanakidou et al. (2005)). Biogenic and anthropogenic emissions of gases (isoprene, monoterpenes, toluene, xylene, etc.) are usually linked to the formation of SOA. Anthropogenic emissions can also lead to an enhancement in secondary organic aerosol formation from naturally emitted precursors (Hoyle et al., 2011).
The most simplified approach is represented by the assumption that the SOA aerosol production is a constant yield of precursor Volatile Organic Compounds (VOCs) (which are assumed to condense instantaneously into organic aerosol, see for ex. Dentener et al. (2006)). A more complex approach is represented by the 2-product schemes (see for ex. Tsigaridis and Kanakidou (2007)), which involve the formation and transport of product gases, which can in turn condense into aerosol particles. The highest level of complexity in the literature is provided by the Volatility Basis Set (VBS) approaches. They use a set of semi-volatile organic aerosol species whose volatility is equally spaced in a logarithmic scale (the basis set), and they react further in the atmosphere (chemical aging) leading to changes in their volatilities (i.e., shifting between volatility bins, see for ex. the scheme implemented in CMAQ-v5 Koo et al. (2014)).
As found by the recent model intercomparison study of Tsigaridis et al. (2014), there is not a clear evidence that an increased level of complexity of the SOA scheme corresponds to an increased performance of global models.

Emissions. Emissions are one of the most important and uncertain input in atmospheric chemistry/aerosol modeling (Russell and Dennis, 2000; Zhang, 2008; Textor et al., 2006). Depending on their source, the emissions can be categorized into two main groups: anthropogenic and natural emissions. While anthropogenic (including biomass-burning) emissions are typically introduced as an input from inventories, the natural emissions may depend upon meteorological parameters, and thus they are online coupled with the meteorological equations. Different parameterizations exist for the production of sea-salt and soil dust particles. A detailed review of the state-of-the-art in sea-salt emission modeling is given in Section 3.1. Since the parameterization of the dust life-cycle is beyond the scope of this thesis, we do not provide here a review of the dust emission parameterization (two comprehensive reviews of dust modeling can be found in Shao (2008) and Kok et al. (2012)).
It is a well known problem that the top-down and bottom-up inventories of biomass-burning emissions (which are usually applied by models) tend to miss fires and underestimate emission fluxes up to a factor of four with respect to satellite observations (Kaiser et al., 2012; Soares et al., 2015). Recently, satellite-derived estimates of the biomass-burning emission fluxes were calculated by the IS4FIRES (Sofiev et al., 2012). These estimates also provide a vertical distribution of fires' emissions, which still represents an open issue for the aerosol community (Martin et al., 2010).
The DMS produced by phytoplankton represents the most important contribution of oceans to the atmospheric chemistry (Kloster et al., 2006). In order to parameterize the emission rates of DMS, coupled marine biogeochemical, ocean circulation, and atmospheric models are needed. Both off- and on-line coupled approaches can be found in the literature.
Natural emissions of volcanic SO_2, both continuous and explosive, are typically included from estimates of inventories. Their vertical injection is usually performed by applying pre-

scriptions depending on the volcanic plume height or the volcanic explosivity index (VEI) (Dentener et al., 2006). If sectional or modal aerosols are represented, the emissions have to be distributed into the different bins or modes. On the other hand, the emission inventories usually do not present any information about size distributions, thus prescribed recommendations are tipically assumed (see for ex. Dentener et al. (2006)). This task is obviously simplified when using bulk aerosol species.

Another important issue is represented by the distribution of the carbonaceous emissions into fractions of hydrophobic and hydrophilic species (or modes). The hydrophobic/hydrophilic fractions of the carbonaceous emissions are usually calculated by using different available prescriptions, such as in Mayol-Bracero et al. (2002) and in Chin et al. (2002) among others.
The most comprehensive models typically transform hydrophobic particles (or modes) to hydrophilic particles by condensation of sulfate on their surface or by coagulation with soluble particles (see for ex. Stier et al. (2005)), while the most simplified models use prescribed conversion rates (for example an e-folding time of 1.6 days as found in Cooke and Wilson (1996)).

Wet removal. The wet removal of aerosols is one of the major source of uncertainty of aerosol modeling (Textor et al., 2006). It is the dominant removal mechanism for certain species (around 90% of the total deposition of sulfate, as observed in the median results of the model intercomparison study of Textor et al. (2006)). The wet deposition of particles is due both to in- and below- cloud scavenging. In-cloud scavenging is due to the conversion of aerosol particles into precipitating cloud droplets or cloud ice crystals. It is typically parameterized by coupling the aerosol equations with the microphysics scheme of the meterological driver model. Models which predict both cloud droplets and cloud ice crystals concentrations are able to explictly account for the aerosol activation as cloud condensation nuclei (CCN)/ice nuclei (IN) and the coagulation of aerosols with cloud droplets (see for example Hoose et al. (2008a).

Below-cloud scavenging is due to the interactions of the aerosol particles with the falling hydrometeors (directional interception, intertial impaction, and Brownian diffusion). In the literature, there is a large number of different parameterizations of these scavenging processes (see for example Table 1). In- and below-cloud scavenging parameterizations have been typically developed separately for both grid-scale and sub-grid clouds.

Convective mixing. At coarse horizontal resolutions i.e. when the area of an updraft is small compared to the area of the model grid cell (Seaman, 1998) ($\Delta x > 12$km (Wang and Seaman, 1997)), the characteristic scales of convective clouds are not solved: thus, a parameterization of the sub-grid clouds is required. The convective mixing is typically parameterized by applying mass-flux schemes. The sub-grid cloud is splitted into vertical layers and the concentrations of aerosols (and gases) is parameterized as functions of the vertical transport from below the cloud layer, of the entrainment from above the cloud layer (for precipitating clouds), and of the entrainment from the sides of the clouds (see for ex. Roselle and Binkovski (1999)). A novel and original approach is represented by the adjustment scheme of Pérez et al. (2011). In this scheme, the change in aerosol mass concentration due to the convective timestep is calculated by relaxing to a reference profile (following the moisture

profile) within a characteristic timescale (see for ex. Pérez et al. (2011)).

Dry removal. The dry removal process can be the dominant removal process for some aerosol species, such as sea-salt and dust (around 80% of the total deposition in the study of Textor et al. (2006)). The dry removal of particles is due both to the sedimentation and to the dry deposition. While the gas sedimentation can be neglected, aerosol models have to account for the sinking due to the gravitational field. The sedimentation of aerosols depends on particle size (and shape), thus on the model microphysics. It is typically parameterized following the Stokes-Cunningham approximation for spherical particles. Sedimentation is implicitly (layer by layer) or explicitly solved by models, or neglected in others (Textor et al., 2006; Zhang, 2008). The sedimentation process is usually solved for all the aerosol tracers, however it is only solved for dust and sea-salt in some models (Textor et al., 2006).

The dry deposition velocity of aerosol particles can be described as the inverse sum of a number of resistance terms (see for ex. Slinn et al. (1978) which depend on the surface properties and on the turbulence of the boundary layer. Thus the deposition parameterization is usually coupled to the turbulence scheme, although most simplified models use constant dry deposition velocities.

Water uptake. The growth due to the water uptake significantly affects the particle size and density, and consequently all the related processes, such as the interaction with the radiative scheme (optical properties), sedimentation, and coagulation. For example, because of their fast growth with ambient RH, sea-salt particles are removed quickly from the atmosphere. There is a large number of different treatments of the water uptake in the literature, leading to high diversities in the calculation of the water aerosol (Textor et al., 2006). Thermodynamically, the water uptake by an aqueous spherical particle can be described by using the Köhler equation (Köhler, 1936). Several parameterizations of the particles activation and of the in-cloud nucleation of cloud droplets are used by models that predict/diagnose the cloud droplets' number (see Ghan et al. (1993), Lin and Leaitch (1997), Abdul-Razzak and Ghan (2000), and Croft et al. (2010) among others), but most of the models use a simplified approach to the calculation of the wet radius by applying prescribed hygroscopic growth factors at different RH fixed values (see for ex. Chin et al. (2002)) or prescribed equations (see Gerber (1985)). Another technique based on regression fits of the solutions of the generalized Kelvin equation for sulfate can be found in the aerosol microphysics module M7 (Vignati et al., 2004).
With increasing the ambient relative humidity (RH), when RH reaches the deliquescent relative humidity (DHR) the particles grow spontaneously by water uptake. With decreasing ambient humidity, the particles release the up-taken water not until a threshold well below DRH, the so-called crystallization or efflorescence relative humidity. This hysteresys phenomenon is parameterized only in few models (see Ghan et al. (2001)), while is not treated in most of the other models (Zhang, 2008).

Coagulation. Coagulation occurs when a completely inelastic collision between two particles takes place: the aerosol number changes, while the volume is conserved. The coagulation rates depend on both the particle number concentrations and particle sizes: thus, as already stated, it is not possible to account for coagulation if only mass concentrations are predicted by model. The change in number concentration is described within a coagulation kernel ac-

counting for different physical mechanisms, which is usually parameterized following Fuchs (1964), as for example in Jacobson (1999) and Vignati et al. (2004). Brownian coagulation is dominant for small particles, while other contributes to the kernel have to be considered for larger particles. Since at typical ambient concentrations the characteristic timescales for coagulation of large particles (among them and with smaller particles) are sufficiently long (several days), these processes can be ignored in regional/global aerosol modeling (Vignati et al., 2004). The neglection of coagulation may lead to overestimates of the concentration of smaller particles, which can in turn affect the calculation of the AOD (Zhang, 2008).

Radiative effects and optical properties. Aerosol models can be on-line or off-line coupled with the meteorological equations. On-line models are able to predict feedback processes between aerosols and meteorology, such as the direct (aerosol-radiation), the semi-direct, and the indirect effects (aerosol-cloud microphysics interactions, that are beyond the scope of this thesis and thus not reviewed in this Section). As already reported in the introduction, the simulation of aerosol effects (mainly of the direct effect) may lead to improvements of short/medium range meteorological forecasts (Sessions et al., 2015; Pérez et al., 2006).
To simulate the direct effect, the radiative transfer scheme has to be coupled with the aerosol optical properties. Specifically, the relevant properties are the AOD, the single-scattering albedo, and the asymmetry factor of particles for each employed spectral band. The optical properties are usually calculated by applying the Mie-theory, depending on the assumptions done for the representation of the mixing state/geometry of particles. Several approaches to the Mie-theory calculations are found, such as the schemes of Chylek et al. (1995), Mitchell (1999), and Mishchenko et al. (2002), among others. To calculate the aerosol optical properties, models have to use estimates of the refractive indices, such as those provided by the data of Downing and Williams (1975), Köepke et al. (1997), and Hess et al. (1998), among others.

Table 1: State-of-the-art aerosol models and their main characteristics. Labels ref., typ. appl., microphys., mix. stand for references, typical application, microphysics, and mixing state, respectively. Labels glob. and reg. stand for global and regional, label sect. for sectional, and labels int./ext. for internally/externally mixed. Meteo coupl. and gas-phase chem. coupl. stand for the coupling with meteorology and gas-phase chemistry, respectively. SOA mech. and SOA prec. stand for SOA formation mechanism and precursor gases.

model	ref.	type	typ. appl.	micro phys.	mix.	meteo coupl.	gas-phase chem. coupl.	SOA mech.	SOA prec.
BCC	Zhang et al. (2012a)	GCM	glob.	sect.	ext.	on		const. yield	monoterpenes
CAM4-Oslo	Kirkevåg et al. (2013)	GCM	glob.	size classes		on	on	const. yield	monoterpenes
CAM5-MAM3	Liu et al. (2012)	GCM	glob.	modal		on	on	1-product	isoprene, terpenes, aromatics, alkanes, alkenes
ECHAM-HAM2	Stier et al. (2005); Zhang et al. (2012b)	GCM	glob.	modal	int./ext.	on	on	2-product	isoprene, monoterpenes, benzene, toluene, xylene
ECMWF-GEMS	Benedetti et al. (2009); Morcrette et al. (2009)	CTM	glob.	sect./ bulk	ext.	off	sulfate from SO_2 sources	const. yield	monoterpenes
GEOS-Chem	Henze and Seinfeld (2006); Liao et al. (2007)	CTM	glob. (reg.†)	modal/ sect./ bulk		off	on	2-product	isoprene, monoterpenes, sesquiterpenes
GISS-MATRIX	Bauer et al. (2008)	GCM	glob.	moments		on	on	const. yield	monoterpenes
GISS-ModelE	Koch et al. (2006, 2007); Tsigaridis and Kanakidou (2007); Tsigaridis et al. (2013)	GCM	glob.	sect. and bulk.	ext.	on	on	2-product	isoprene, monoterpenes, sesquiterpenes
GISS-TOMAS	Lee and Adams (2010, 2012); Lee et al. (2014)	GCM	glob.	sect.		on	on	1-product	monoterpenes
GISS-CMU-VBS	Farina et al. (2010); Jathar et al. (2011)	GCM	glob.	sect.		on	on	VBS	isoprene, monoterpenes, sesquiterpenes, alkanes, aromatics
GOCART	Chin et al. (2000); Ginoux et al. (2001); Chin et al. (2002)	CTM	glob.	sect./ bulk	ext.	off	SO_2, DMS on	const. yield	monoterpenes
HadGEM2	Bellouin et al. (2011)	GCM	glob.	modal	int.	off/on	clim.	terpenes	
IMPACT	Lin et al. (2012)	CTM	glob.	sect./ bulk	ext.	off	H_2O_2 on	organic nitrates and peroxides partitioning	isoprene, monoterpenes, aromatics
LMDz-INCA	Schulz et al. (2007); Myhre et al. (2009); Balkanski (2011)	GCM	glob.	modal	int./ ext.	off/on	on	const. yield	monoterpenes
MOZART-4	Emmons et al. (2010)	CTM	glob.	bulk	ext.	off	on	oxidation of monoterpenes and toluene	monoterpenes, toluene
OsloCTM2	Hoyle et al. (2007, 2009); Myhre et al. (2009)	CTM	glob.	sect./ bulk	ext.	off	on	2-product	isoprene, terpenoid, aromatics
SPRINTARS	Takemura et al. (2000, 2002, 2005, 2009)	GCM	glob.	sect./ bulk	ext.	off/on	SO_2, DMS, H_2O_2 on	const. yield	monoterpenes
TM5	Huijnen et al. (2010); Aan de Brugh et al. (2011); van Noije et al. (2014)	CTM	reg. (glob.†)	modal	ext.	off	on	const. yield	monoterpenes
WRF/Chem	Grell et al. (2005); Peckham et al. (2011); Zhang et al. (2012c)	CTM	reg./ glob.	modal/ sect.⋆	int./ ext.	on	on	n-product/ VBS	α-pinene, limonene, isoprene, sesquiterpenes, alkanes, alkenes, aromatics
CHIMERE	Bessagnet et al. (2004, 2009); Menut et al. (2013)	CTM	reg.	sect.	int.	off	on	2-product	monoterpenes, alkanes, aromatics
CMAQ	Binkowski and Roselle (2003); Kelly et al. (2010); Koo et al. (2014)	CTM	reg.	modal	int.	off	on	n-product/ VBS	*alpha*-pinene, limonene, isoprene, sesquiterpenes, alkanes, alkenes, aromatics

⋆ depending on the aerosol module (more than one module implemented)
† depending on the off-line meteorological fields

1.2 Aim of the thesis and organization of the manuscript

The objective of the present thesis is the development and the evaluation of an aerosol module implemented within the NMMB. The module is designed to provide short and medium range forecast of aerosols for different purposes, from the simulation of the global aerosol distribution to the prediction of regional scales. The implementation is based on the developments of the NMMB/BSC-Dust model. To perform regional simulations of the chemical weather, the module is also coupled with the gas-phase chemical scheme of the NMMB/BSC-CTM).

Specifically, this thesis is devoted to the modeling of sea-salt, organic aerosol, both primary and secondary, black carbon, and sulfate, with the aim to extend the dust model to an aerosol module able to provide simulations of the total AOD. The modeling of ammonium/nitrate aerosols and nitrogen chemistry (that is currently under development) is beyond the scope of this thesis. Even if the modeling system is designed to solve both global and regional scales, the model is evaluated only at the global scale in this work. High-resolution regional simulations of the sea-salt aerosol at specific coastal/orographic sites are additionally discussed.

In Chapter 2 we present the general formulation of the aerosol module.

In Chapter 3, as a first step of development, we present on the modeling of the sea-salt aerosol. Five emission schemes have been implemented and evaluated at global scale by comparison with several observational networks (Section 3.1). Then, we investigated the effects of the model resolution on the simulation of the sea-salt transport at specific coastal/orographic sites, also performing regional simulations (Section 3.2).

As a second step, we implemented and evaluated (at global scale) the carbonaceous and sulfate aerosols (Chapter 4). The AOD simulated by the full module (including dust and sea-salt) was also evaluated by comparison with ground-based and satellite observations (Section 4.2.4).

Note that the AOD evaluation presented in Section 3.1 only refers to the dust+sea-salt (the only available aerosols at that step of development) coarse fraction. Since Sections 3.1, 3.2 and Chapter 4 are extracted from published/submitted works, some observational sites (used for different model evaluations) can be used with a different labeling depending on the considered Section (for ex. the Invercargill station, which is itemized as “Invercargill (g)” in Section 3.1 and as “Invercargill (15)” in Chapter 4). In this case, we recommend to refer to the explicit site name (in our ex.: “Invercargill”). The labeling used in each Section has to be intended valid only inside its own Section.

Finally, we present the conclusions in Chapter 5.

Chapter 2 – Model formulation

Based on:

Spada, M., Jorba, O., Pérez García-Pando, C., Janjic, Z., and Baldasano, J. M.: Modeling and evaluation of the global sea-salt aerosol distribution: sensitivity to size-resolved and sea-surface temperature dependent emission schemes, Atmos. Chem. Phys., 13, 11735-11755, doi:10.5194/acp-13-11735-2013, 2013.

Spada, M., Jorba, O., Pérez García-Pando, C., Tsigaridis, K., Soares, J., and Janjic, Z.: Global aerosols in the online multiscale NMMB/BSC Chemical Transport Model, in preparation for Geosci. Model Dev.

Amazon clouds. Photo credits: pielkeclimatesci.wordpress.com

2 Model formulation

The NMMB/BSC-CTM is a fully online chemical transport model coupling the atmospheric equations of NMMB with the gas-phase and aerosol continuity equations of BSC-CTM. The mineral dust model (NMMB/BSC-Dust) of Pérez et al. (2011) and the gas-phase mechanism of Jorba et al. (2012) represented the starting point of our work. This thesis focused on the inclusion of sea-salt, organic aerosol, black carbon, and sulfate into the module. The implementation and evaluation of other globally relevant aerosols (such as nitrate) is underway. According to the features of its unified meteorological core, NMMB/BSC-CTM was conceived for short- and medium-range forecasting for a wide range of spatial scales as well as for climate studies. Due to its fully online coupling, several feedback processes among gases, aerosol particles and radiation are taken into account by the model. In particular, the radiative effect of aerosols is considered, while cloud–aerosol interactions are neglected at present. The online coupling of aerosol optical properties and gas-phase photolysis reactions is also under development.

2.1 Modeling background

As a short introduction to the developments presented in this Section, we describe the NMMB, the meteorological core of the model and of the BSC-CTM dust module (BSC-Dust).

2.1.1 The non-hydrostatic multiscale model NMMB

The NMMB allows simulations of scales ranging from global to large eddy simulations (LES) in global and regional domains. The regional NMMB has been used at NCEP as the regional North American Mesoscale (NAM) model since October 2011. The global model is formulated on the latitude-longitude grid, by applying conservative polar boundary conditions and polar filtering, slowing down the tendencies of basic dynamic variables (Janjic, 2009; Janjic and Gall, 2012). Rotated latitude-longitude grids are employed for regional simulations in order to obtain more uniform grid distances. In both cases, the horizontal discretization is performed on the Arakawa B-grid. In the vertical, the general hybrid sigma-pressure coordinate (Simmons and Burridge, 1981) is used with the Lorenz staggering. The "isotropic" horizontal finite volume differencing technique assures the conservation of a number of dynamical and quadratic quantities (among these, energy and enstrophy). More details about the numerical schemes of the NMMB can be found in Janjic (1977, 1979, 1984, 2003) and in Janjic et al. (2001, 2011).

A variety of physical schemes are implemented in the model. A list of these parameterizations and their respective references were presented in Pérez et al. (2011) and further details can be found in Janjic (1990, 1994, 1996, 2001). For our purposes, we shortly recall the parameterizations involved in the modeling of the aerosol life-cycle, i.e., surface layer, grid-scale cloud microphysics, convective adjustment and precipitation, and radiation schemes. Boundary layer, and free atmosphere turbulence are parameterized using the Mellor-Yamada-Janjic (MYJ) turbulence closure scheme (Mellor and Yamada, 1982; Janjic, 2001). In the surface layer the Monin–Obukhov similarity theory (Monin and Obukhov, 1954) is applied (Janjic, 1996) in combination with a viscous sub-layer parameterization over oceans (Janjic, 1994). The wind speed at 10 m (U_{10}), which is the key parameter of sea-salt production schemes is computed consistently with the surface layer parameterization. The friction velocity u^* is computed as the square root of the surface layer vertical momentum transport.

Grid-scale clouds are parameterized with the scheme of Ferrier et al. (2002) including five prognostic cloud variables. The relevant quantities for the coupling with aerosol processes are the mixing ratios of both liquid and ice cloud water and their conversion rates to precipitation. The Betts-Miller-Janjic convective adjustment scheme (Betts, 1986; Betts and Miller, 1986; Janjic, 1994, 2000) is used for sub-grid-scale clouds. Using conservational constraints, the convective clouds are represented by reference humidity and temperature profiles. Both water vapor mixing ratio and temperature are relaxed toward reference values within a convection time step. In the case of deep convection, the reference profiles and the relaxation time are governed by the cloud efficiency E which depends on convective regime. This is a non-dimensional parameter obtained as a combination of entropy change, precipitation, and mean cloud temperature (Janjic, 1994, 2000). The shallow convection parameterization closure uses the constraint that the entropy change must be non-negative Janjic (1994, 2000). The NMMB uses the operational Geophysical Fluid Dynamics Laboratory (GFDL) radiation package, which includes shortwave (Lacis and Hansen, 1974) and longwave (Fels and Schwarzkopf, 1975) schemes. Since the coupling with aerosols is not allowed by the operational GFDL scheme, the Rapid Radiative Transfer Model (RRTM) (Mlawer et al., 1997) was implemented in the model (Pérez et al., 2011). By using RRTM, it is possible to couple radiation (both long- and shortwave) and aerosols by providing AOD, asymmetry factor, and single-scattering albedo.

2.1.2 The BSC-CTM dust module

The development of the aerosol module is conceived as an extension of the implementation of BSC-Dust (Pérez et al., 2011; Haustein et al., 2012), i.e., the dust module of NMMB/BSC-CTM. BSC-Dust includes 8 transport bins ranging from $0.1\,\mu$ m to $10\,\mu$m in dry radius. Within each transport bin a log-normal time-invariant sub-bin distribution is assumed. The processes considered by the module are dust emission, horizontal and vertical advection, horizontal diffusion and vertical transport by turbulence and convection, dry deposition and sedimentation, and wet removal including in- and below- cloud scavenging from grid- and sub-grid scale clouds. Water uptake was not considered.

The online emission process accounts for surface wind speed and turbulence, land use type, vegetation cover, erodibility, surface roughness, soil texture and soil moisture. The dust vertical flux is calculated from the horizontal flux following the empirical relationship of Marticorena and Bergametti (1995) and Marticorena et al. (1997). Then, the vertical flux is distributed over each size transport bin according to the 3 lognormal background source modes of D'Almeida (1987).

Both global and regional simulations of dust AOD have been exhaustively evaluated in Pérez et al. (2011) and Haustein et al. (2012), respectively. The evaluation at global scale performed by Pérez et al. (2011) for the year 2000 showed high annual correlations of model with observations (0.87 for surface concentration and 0.89 for AOD). However, an overestimate of small (clay) dust particles was found near source areas, due to either inaccuracies in the size distribution of the emissions, vertical transport and/or removal.

2.2 Aerosol transport parameterization

Aerosols are assumed to be externally mixed in our implementation. Details on the assumptions done concerning aerosol size representation and physical properties can be found in

Chapters 3 and 4. Assumptions are listed in Table 2. The full aerosol package includes eight bins for dust and eight bins for sea-salt aerosols, eight transport modes for carbonaceous aerosols (both primary and secondary), and one mode for sulfate. The continuity equation is separately solved for each prognostic size-bin/mode k:

$$\partial_t q_k + (\vec{v} \cdot \nabla)_h q_k = F_k^{(\text{prod})} - \sum_n F_{n,k}^{(\text{sink})} + F_k^{(\text{diff})}, \tag{1}$$

where q_k are the aerosol dry mass mixing-ratios, $\vec{v}$ is the wind velocity, subscript h stands for horizontal operator, and $F_k^{(\text{prod})}$, $F_{n,k}^{(\text{sink})}$, $F_k^{(\text{diff})}$ represent aerosol production (both primary and secondary), sink/mixing, and turbulent diffusion terms, respectively. Advection and diffusion are analogous to those of moisture in NMMB (i.e. Eulerian, positive definite, and monotonic) (Janjic and Gall, 2012). Below, we give an overview of the sink/mixing term parameterizations included in the dust model that have been extended to the other aerosol species, in order to point out the extension to wet particles. A more detailed description of each scheme can be found in Pérez et al. (2011).

The discussion of primary and secondary production schemes and additional specific sink terms (such as those involved in the chemical mechanism) are further presented in Chapters 3 and 4.

2.2.1 Extension to wet particles

The aerosol life cycle may be strongly affected by water uptake. Hygroscopic growth may increase particles' radii by a factor of four or more. Following Chin et al. (2002) we introduced prescribed RH-dependent growth factors $\phi(\text{RH}) = r_\text{w}/r_\text{d}$, derived from the Global Aerosol Data Set of Köepke et al. (1997) and the database of D'Almeida (1991) (Table 2). r_w and r_d are the wet and the dry particle radius, respectively. We assume the same factors for any radius-moment representation, such as effective and volume-mean radii.

Given $\phi(\text{RH})$, the water-uptake process is fully described by extending any dry particle parameter to its respective wet value. In particular we obtain wet particle radius and density as

$$r_\text{d} \rightarrow r_\text{w} = \phi \cdot r_\text{d} \tag{2}$$

$$\rho_\text{d} \rightarrow \rho_\text{w} = f_\text{d}\rho_\text{d} + (1 - f_\text{d})\rho_\text{water} \tag{3}$$

where ρ_water is the density of water and f_d is the volume fraction of dry aerosol ($f_\text{d} = \phi^{-3}$). By using this simplified approach, all aerosol processes affected by hygroscopic growth are easily reformulated by extending the parameterizations used in Pérez et al. (2011) (dry aerosol) to the wet-particle case, i.e., by applying Eqs. (2) and (3), as described below.

2.2.2 Sedimentation and dry deposition

Sedimentation is governed by the gravitational settling velocity $v_{g,k}$, calculated following the Stokes–Cunningham approximation. v_g depends on the particle size and thus on the water uptake:

$$v_g = \frac{4r_w^2 g(\rho_w - \rho_a)C_c}{18\nu} \tag{4}$$

where g is the gravitational constant, ρ_a the air density, ν the air viscosity, and C_c the Cunningham correction factor:

$$C_c = 1 + \frac{\lambda}{r_w}(1.257 + 0.4\exp -1.1 r_w/\lambda) \tag{5}$$

where λ is the mean free path of air molecules. The sedimentation is implictly solved for the aerosol mixing ration q at the time $t + \Delta t$ from column top to bottom:

$$q(t + \Delta t, L) = \frac{q(t, L-1) v_g \Delta t / \Delta z(t, L-1) + q(t, L)}{(1 + v_g \Delta t / \Delta z(t, L))} \tag{6}$$

where Δt is the timestep, L the vertical level, and Δz the vertical layer depth.

The dry deposition velocity $v_{\rm d}$, acting at the bottom layer, is parameterized following Zhang et al. (2001):

$$v_d = v_g + \frac{1}{R_a + R_s} \tag{7}$$

The aerodynamic resistance R_a accounts for turbulence and it is calculated using the NMMB surface layer scheme which is based on the well established Monin-Obukhov similarity theory (Monin and Obukhov, 1954) and the parameterizations of a viscous sub-layer for land (Zilitinkevich, 1965) and water (Janjic, 1994). The dependence on ϕ is introduced in the surface resistance calculation (R_s), which accounts for particle size and density (Slinn, 1982).

2.2.3 Wet deposition and mixing

Wet scavenging fluxes are parameterized both for grid-scale (stratiform) and sub-grid scale (convective) clouds.

Grid-scale deposition. The aerosol grid-scale wet deposition scheme is coupled with the scheme of Ferrier et al. (2002) implemented within the NMMB. The aerosol wet deposition is calculated sequentially from model column top ($L = 1$) down to the surface ($L = LM$):

$$F^{(\rm wet)}(L) = F^{(\rm wet)}(L-1)[1 - \alpha f_{\rm evp}(L)] + \Delta F^{(\rm wet)}(L) \tag{8}$$

The in-cloud scavenging flux is parameterized using a solubility parameter ϵ_k that is defined as the fraction of aerosol contained in cloud which may eventually precipitate:

$$\Delta F^{(\rm wet)}(L)|_{\rm in} = \epsilon \Big[f_{\rm l} \frac{P_{\rm CR}}{Q_w} + f_{\rm i} \frac{P_{\rm IR}}{Q_i} \Big] M \tag{9}$$

M is the dry mass loading of aerosol in the gridcell, $P_{\rm CR}$ is the conversion rate of cloud water to rain by autoconversion, accretion, and shedding of accreted cloud water, $P_{\rm IR}$ is the conversion rate of cloud ice to precipitation through melting, f_l is the fraction of cloud water, f_i is the fraction of cloud ice, Q_w is the cloud water mixing ratio, and Q_i is the cloud ice mixing ratio. The ϵ values assumed in the model are resumed in Table 2). The values found in Zakey et al. (2006) for dust represent an intermediate between pure hydrophobic and pure hydrophilic hypothesis. For the sea-salt we assume $\epsilon_{\rm ss} = 2\epsilon_{\rm du}$, obtaining values that are consistent with those used in other state-of-the-art models (see for ex. the sensitivity study in Fan and Toon, 2011). For hydrophilic carbonaceous and sulfate particles we fix ϵ to 0.8,

close to the scavenging parameter assumed by Stier et al. (2005) for the soluble accumulation mode in stratiform liquid clouds.

Grid-scale below cloud scavenging is parameterized following Slinn (1984) in which capture efficiencies E depend on the wet radius and density of the aerosol particles:

$$\Delta F^{(\mathrm{wet})}(L)|_{\mathrm{below}} = \sum_{p=l,s} \frac{\gamma_p P_p E_p(r_w, D)}{D} M \tag{10}$$

where l and i stand for liquid and ice precipitations, respectively. γ is a numerical factor (1.5 for liquid precipitation according to Loosmore and Cederwall (2004) and 0.6 for ice precipitation), P is the precipitation rate, D is the characteristic diameter of raindrops/ice crystals, and M is the dry mass loading of aerosol in the gridcell.

Convective deposition and mixing. For sub-grid (convective) clouds, the scavenging fluxes are coupled with the Betts–Miller–Janjic scheme (BMJ) of the NMMB. The convective in-cloud scavenging parameterization employs solubility factors ϵ as well:

$$\Delta F^{(\mathrm{wet})}(L)|_{\mathrm{in}} = -\epsilon \frac{\Delta Q_{\mathrm{tot}}}{Q_{\mathrm{tot}}} M \tag{11}$$

where ΔQ_{tot} is the total change of moisture in the convective cloud between calls to convection, and Q_{tot} and M are the total moisture and the total aerosol dry mass loading within the convective cloud at the beginning of the time step.

After the in-cloud scavenging, the remaining aerosol is assumed vertically mixed by performing a conservative relaxation towards reference profiles:

$$\Delta q = (q_{\mathrm{ref}} - q) \frac{\Delta t}{\tau_{\mathrm{adj}}/F(E)} \tag{12}$$

where τ_{adj} is the characteristic time-scale of adjustment and $F(E)$ a cloud efficiency factor (Janjic, 1994). q_{ref} follows the shape of the reference moisture profile and the total mass loading of the aerosol reference profile equals the eventual remaining mass of aerosol after the in-cloud scavenging during the convective timescale.

The parameterization of sub-grid below-cloud scavenging is analogous to the case of grid-scale clouds Within shallow non-precipitating convective clouds aerosol is homogeneously mixed within the cloud.

2.3 Radiation and AOD calculation

In order to couple aerosol and radiation processes, the RRTM radiative transfer model (Mlawer et al., 1997) including aerosol effects has been implemented into the model as an alternative option to the operational Geophysical Fluid Dynamics Laboratory radiation package (Lacis and Hansen, 1974; Fels and Schwarzkopf, 1975). The new radiation module allow aerosols to interact with both short and longwave radiation. For each size bin/mode, wavelength, and RH range (see Fig. 1 for calculations at 500nm) we calculate extinction efficiency $Q^{\mathrm{ext}}_{\lambda,k}(\phi)$, single-scattering albedo and asymmetry factor with the Mie-algorithm of Mishchenko et al. (2002). Spherical homogeneous particles are assumed. The refractive indices were derived from the Global Aerosol Data Set (GADS) of Köepke et al. (1997). Extinction efficiencies

Table 2: Aerosol tracers implemented in the NMMB/BSC-CTM and their transport/optical characteristics. phob/phil stand for hydrophobic and hydrophilic aerosol (label interm points out the intermediate assumption taken for dust). r_{eff}, ρ, and ϵ indicate effective radius, density, and wet scavenging factor of particles, respectively. ϕ is the hygroscopic growth factor at seven increasing values of RH (0%, 50%, 70%, 80%, 90%, 95%, 99%).

bin	phob/phil	precursors	$r_{\text{eff}}(\mu m)$	$\rho(g/cm^3)$	ϵ	$\vec{\phi}$(RH)
organic aerosol						
POA1	phob	–	0.1003	1.80	0	–
POA2	phil	–	0.1003	1.80	0.8	[1.0, 1.2, 1.4, 1.5, 1.6, 1.8, 2.2]
SOA1	phil	TERP	0.1003	1.80	0.8	[1.0, 1.2, 1.4, 1.5, 1.6, 1.8, 2.2]
SOA2	phil	TERP	0.1003	1.80	0.8	[1.0, 1.2, 1.4, 1.5, 1.6, 1.8, 2.2]
SOA3	phil	ISOP	0.1003	1.80	0.8	[1.0, 1.2, 1.4, 1.5, 1.6, 1.8, 2.2]
SOA4	phil	ISOP	0.1003	1.80	0.8	[1.0, 1.2, 1.4, 1.5, 1.6, 1.8, 2.2]
black carbon						
BC1	phob	–	0.0430	1.00	0	–
BC2	phil	–	0.0430	1.00	0.8	[1.0, 1.0, 1.0, 1.2, 1.4, 1.5, 1.9]
sulfate						
SU	phil	SO_2, DMS	0.2434	1.70	0.8	[1.0, 1.4, 1.5, 1.6, 1.8, 1.9, 2.2]
dust						
DU1	interm	–	0.15	2.50	0.6	–
DU2	interm	–	0.25	2.50	0.6	–
DU3	interm	–	0.45	2.50	0.6	–
DU4	interm	–	0.78	2.50	0.3	–
DU5	interm	–	1.32	2.65	0.3	–
DU6	interm	–	2.24	2.65	0.1	–
DU7	interm	–	3.80	2.65	0.1	–
DU8	interm	–	7.11	2.65	0.1	–
sea-salt						
SS1	phil	–	0.14	2.16	0.6	[1.0, 1.6, 1.8, 2.0, 2.4, 2.9, 4.8]
SS2	phil	–	0.24	2.16	0.6	[1.0, 1.6, 1.8, 2.0, 2.4, 2.9, 4.8]
SS3	phil	–	0.45	2.16	0.6	[1.0, 1.6, 1.8, 2.0, 2.4, 2.9, 4.8]
SS4	phil	–	0.79	2.16	0.3	[1.0, 1.6, 1.8, 2.0, 2.4, 2.9, 4.8]
SS5	phil	–	1.36	2.16	0.3	[1.0, 1.6, 1.8, 2.0, 2.4, 2.9, 4.8]
SS6	phil	–	2.32	2.16	0.1	[1.0, 1.6, 1.8, 2.0, 2.4, 2.9, 4.8]
SS7	phil	–	4.13	2.16	0.1	[1.0, 1.6, 1.8, 2.0, 2.4, 2.9, 4.8]
SS8	phil	–	8.64	2.16	0.1	[1.0, 1.6, 1.8, 2.0, 2.4, 2.9, 4.8]

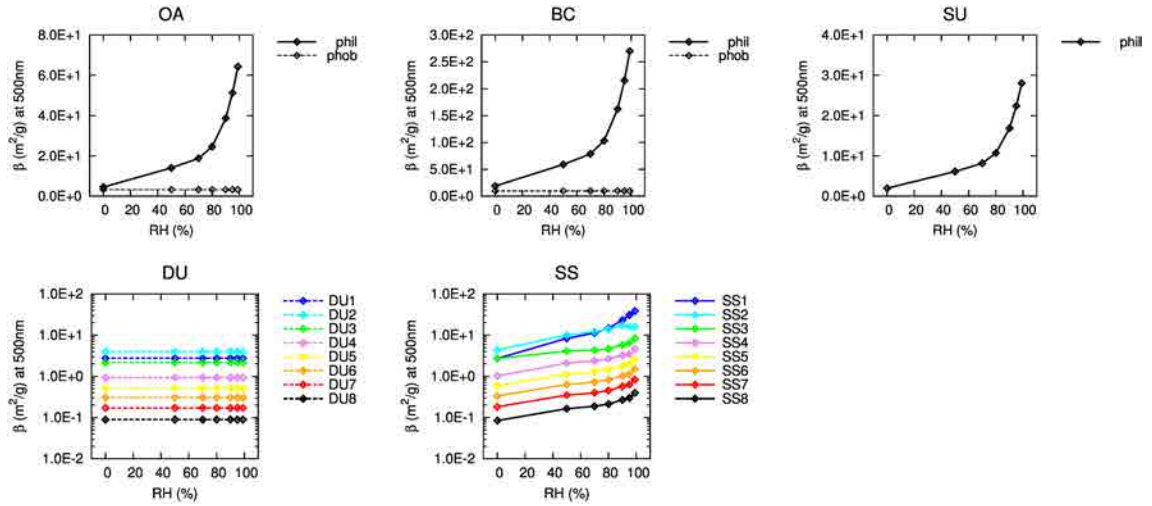

Figure 1: Mass extinction efficiencies (β) at 500nm depending on RH values. Dust and sea-salt bins are shown with different colors; phobic/philic aerosols with solid/dotted lines, respectively. Sulfate and sea-salt are assumed to be completely philic; dust is assumed to be phobic in the optical calculations. Dust and sea-salt efficiencies are shown with logarithmic scales.

also depend on the modal or sub-bin log-normal geometric parameters r^{g} and σ^{g}. The AOD is obtained as

$$\tau_{\lambda,k} = \beta_{\lambda,k}\tilde{M}_k, \tag{13}$$

where $\tilde{M}_k$ is the columnar dry mass loading of each bin/mode and $\beta_{\lambda,k}$ is a mass extinction coefficient which accounts for water uptake:

$$\beta_{\lambda,k} = \frac{3\phi^3 Q^{\mathrm{ext}}_{\lambda,k}(\phi, r^{\mathrm{g}}_{\mathrm{w}}, \sigma^{\mathrm{g}}_{\mathrm{w}})}{4 r^{\mathrm{eff}}_{\mathrm{w},k}\rho_{\mathrm{d},k}}. \tag{14}$$

Because of their external mixing, the total AOD is equal to the sum over all bins/modes:

$$\tau_\lambda = \sum_{k=1,N_a} \tau_{\lambda,k}. \tag{15}$$

with $N_a = 25$ (see Table 2).

Chapter 3 – Sea-salt aerosol

Based on:

Spada, M., Jorba, O., Pérez García-Pando, C., Janjic, Z., and Baldasano, J. M.: Modeling and evaluation of the global sea-salt aerosol distribution: sensitivity to size-resolved and sea-surface temperature dependent emission schemes, Atmos. Chem. Phys., 13, 11735-11755, doi:10.5194/acp-13-11735-2013, 2013.

Spada, M., Jorba, O., Pérez García-Pando, C., Janjic, Z., and Baldasano, J. M.: On the evaluation of global sea-salt aerosol models at coastal/orographic sites, Atmos. Env., 101, 41–48, doi:10.1016/j.atmosenv.2014.11.019, 2015

A wave breaking over the bow of the R/V Knorr research vessel.
Photo credits: Robin Pascal (ciresblogs.colorado.edu)

3 Sea-salt aerosol

The modeling of sea-salt aerosol represented the first step of our module development. In Section 3.1 we present the parameterizations that we applied to describe the sea-salt life-cycle and an exhaustive model evaluation at global scale (1°x1.4°), including an evaluation of the coarse AOD fraction calculated from the contributions of sea-salt and dust aerosols (the only two aerosol species available at this stage of module development). High resolution (0.1°x0.1°) simulations for regions of interest, where effects due to the complex topography are found to affect the simulation of the sea-salt transport, are presented and discussed in Section 3.2.

3.1 Modeling and evaluation of the global sea-salt aerosol distribution: sensitivity to size-resolved and SST-dependent emission schemes

Sea salt is one of the most abundant aerosol species globally. It perturbs the radiative fluxes directly by interacting with shortwave and longwave radiation, and indirectly by acting as cloud condensation nuclei (CCN) and thus altering marine cloud brightness and lifetime. It also influences heterogeneous chemistry mainly over coastal areas (Lewis and Schwartz, 2004) and is co-emitted with organic aerosols (Tsigaridis et al., 2013). The major uncertainties in the sea-salt life cycle are emission (Textor et al., 2006; de Leeuw et al., 2011), water uptake (Textor et al., 2006), and deposition (Textor et al., 2007). Lewis and Schwartz (2004) estimate the total sea-salt emission to vary from $0.3\,\mathrm{Pg\,yr^{-1}}$ to $30\,\mathrm{Pg\,yr^{-1}}$ and estimates from models involved in the AEROCOM project range from $3\,\mathrm{Pg\,yr^{-1}}$ to $18\,\mathrm{Pg\,yr^{-1}}$ for year 2000 (Textor et al., 2006). These uncertainties may lead to differences of a factor of two or more in the simulated monthly averaged concentrations among different models, and between simulated and observed concentrations (Textor et al., 2006). The lack of comprehensive measurement data sets hampers evaluation efforts and the improvement of sea-salt models and related parameterizations. For a given region and a given time period, only a few coincident measurements of surface concentration, AOD, and particle-size distribution are available, and a few emission and deposition flux estimates at specific sites and temporal intervals can be found in literature. Additional difficulties arise from biases in satellite retrievals, particularly in the most important sea-salt production regions (e.g. Jaeglé et al., 2011).

Several approaches are typically used to parameterize the sea-salt emission process, from semi-empirical combinations of whitecap factorization and concentration measurements (Monahan et al., 1986; Smith et al., 1993; Smith and Harrison, 1998; Andreas, 1998; Hoppel et al., 2002; Gong, 2003; Petelski et al., 2005; Mårtensson et al., 2003; Clarke et al., 2006; Caffrey et al., 2006; Jaeglé et al., 2011; Fan and Toon, 2011), to empirical methods such as the use of concentration vertical profiles from aircraft observations (Reid et al., 2001). Parameterizations of sea-salt emission fluxes may account for different production mechanisms (e.g. bubble bursting, spume cutting), which may depend on different meteorological parameters. The most used parameter is wind speed at 10 m (U_{10}), but there have also been attempts to include dependencies on SST, wave height, increasing/decreasing wind, salinity and other parameters. Exhaustive reviews of these efforts and their performance can be found in Lewis and Schwartz (2004), O'Dowd and de Leeuw (2007), de Leeuw et al. (2011), and Grythe et al. (2013). The above-mentioned parameterizations are assumed for the open ocean. Production in the surf-zone represents an additional open issue (de Leeuw et al., 2000).

The high hygroscopicity of sea-salt requires water uptake schemes based on prescribed growth factors (Chin et al., 2002) or equations (Gerber, 1985; Ghan et al., 2001) or explicit

calculations of the condensed aerosol water (Vignati et al., 2004). However, their performance is hard to assess and it remains an open topic for aerosol modeling (Textor et al., 2006).

Togheter with the development of a sea-salt module, in this work we investigate the uncertainties associated with sea-salt, open-ocean emission schemes.

3.1.1 Size representation

We assume a dry radius lower cutoff of 0.1 μm in the size distribution. Upper size cutoff is fixed to 15 μm to comprehensively account for all the different formation processes involved by the implemented production schemes. Size-bins are listed in Table 2. Simulated sea-salt mass and AOD are strongly influenced by the number of size-bins adopted, due to the strong dependence of dry deposition upon particle size (Witek et al., 2011). Simulated values tend to converge above 15 size-bins, while mass loss takes place otherwise. We employ 8 size-bins which involves a mass loss of 5 % (Witek et al., 2011) – a negligible quantity compared to emission uncertainties – as a trade-off for doubled computational efficiency. A sub-bin log-normal approach is assumed to calculate different momenta of particle radius, such as dry effective radius $r_{\rm d}^{\rm eff} = < r_{\rm d}^3 > / < r_{\rm d}^2 >$ and volume mean radius $r_{\rm d}^{\rm vm} = (< r_{\rm d}^3 > / < r_{\rm d}^0 >)^{1/3}$. We assume the canonical log-normal distribution of Lewis and Schwartz (2004), characterized by a geometric radius at RH = 80 %, $r_{80}^{\rm g} = 0.3\,\mu$m and geometric standard deviation $\sigma^{\rm g} = 2.8$.

3.1.2 Open-ocean production

Strong uncertainties of up to one order of magnitude affect the estimates of sea-salt production fluxes. The most widely used technique to parameterize sea-salt emission is the so-called whitecap method, by which the flux is factorized as a product of sea-surface whitecap fraction and production per whitecap unit, both terms being affected by significant uncertainties. Parameterizations use wind-speed at 10 m (U_{10}), SST, atmospheric stability, sea-surface salinity, and ocean waves properties (height, age, relative direction respect to wind), for which Lewis and Schwartz (2004) and O'Dowd and de Leeuw (2007) provide useful reviews. In this study, we implement five widely used whitecap method schemes for open-ocean production (surf-zone production is neglected) with details provided in Table 3. Labels G03, M86, SM93, MA03, and J11 stand for schemes provided in Gong (2003), Monahan et al. (1986), Smith et al. (1993), Mårtensson et al. (2003), and Jaeglé et al. (2011), respectively. G03, M86, and SM93 are derived from observational data sets and only depend on U_{10}; MA03 is derived from laboratory experiments and includes SST effects that are size-dependent. J11 emissions are formulated by multiplying the G03 scheme by a SST-dependent function equal for all particle sizes. The function was fitted using the GEOS-CHEM model and observations. In our work, we keep the function as it was derived by Jaeglé et al. (2011). With the exception of SM93, all the implemented schemes apply the same wind speed power law ($U_{10}^{3.41}$) in the whitecap parameterization. Consequently, we do not focus on the model sensitivity to changes in this term. MA03 was derived for a temperature interval ranging from 271 K to 298 K, which does not strictly cover the annual variation of global SST. J11 is formulated for temperatures ranging from 273.15 K to 303.15 K. For our comparison, we choose schemes differing in particle size and production mechanism description. Figure 2 shows that the strongest uncertainties appear for the ultrafine particles ($r_{\rm d} < 0.1\,\mu$m), which do not play a relevant role in the simulation of mass concentration and AOD, and thus are beyond the scope of this work.

All considered schemes account for sea-salt formation from bubble bursting. Spume pro-

Table 3: Sea-salt number emission fluxes implemented in NMMB/BSC-CTM. $\mathrm{d}F_N/\mathrm{d}r$ fluxes in units $[\mathrm{m}^{-2}\,\mathrm{s}^{-1}\,\mu\mathrm{m}^{-1}]$, $\mathrm{d}F_N/\mathrm{d}\log(r)$ fluxes in units $[\mathrm{m}^{-2}\,\mathrm{s}^{-1}]$; r_{80} and r_d stand for wet radius at RH = 80 % and dry radius in units $[\mu\mathrm{m}]$, respectively. If r is used, dry or wet radius was not specified. U_{10} in $\mathrm{m\,s}^{-1}$. SST in K units. Formul. range stands for the size-range in the original formulation of each parameterization. The assumption $r_{80} = 2r_\mathrm{d}$ is used to merge wet and dry radius intervals. All schemes are applied in the range $r_\mathrm{d} \in [0.1\text{–}15]\,\mu\mathrm{m}$.

Production scheme	Reference	Mechanism	Formul. range
$\frac{\mathrm{d}F_N^{(\mathrm{emi})}}{\mathrm{d}r_{80}}\vert_{\mathrm{G03}} = 1.373 \cdot U_{10}^{3.41} \cdot r_{80}^{-A(r_{80})}(1 + 0.057 r_{80}^{3.45}) \cdot 10^{1.607\exp(-C(r_{80})^2)}$	G03	bubbles, spume?	$r_{80} \in [0.07\text{–}20]$
$A = 4.7(1+\theta r_{80})^{-0.017 r_{80}^{-1.44}}$, $\theta = 30$, $C = (0.433 - \log(r_{80}))/0.433$			
$\frac{\mathrm{d}F_N^{(\mathrm{emi})}}{\mathrm{d}r_{80}}\vert_{\mathrm{M86}} = 1.373 \cdot U_{10}^{3.41} \cdot r_{80}^{-3}(1 + 0.057 r_{80}^{1.05}) \cdot 10^{1.19\exp(-B(r_{80})^2)}$	M86	bubbles	$r_{80} \in [0.8\text{–}8]$
$B = (0.38 - \log(r_{80}))/0.65$			
$\frac{\mathrm{d}F_N^{(\mathrm{emi})}}{\mathrm{d}r_{80}}\vert_{\mathrm{SM93}} = \sum_{k=1,2} A_k(U_{10}) \exp\left[-f_k \ln\left(\frac{r_{80}}{r_k}\right)^2\right]$	SM93	spume	$r_{80} \in [5\text{–}30]$
$\log(A_1) = 0.0676 U_{10} + 2.43, \log(A_2) = 0.959 U_{10}^{1/2} - 1.476$ $r_1 = 2.1, r_2 = 9.2$			
$\frac{\mathrm{d}F_N^{(\mathrm{emi})}}{\mathrm{d}\log(2r_\mathrm{d})}\vert_{\mathrm{MA03}} = 3.84 \cdot 10^{-6} \cdot U_{10}^{3.41} \cdot (\alpha_j(r_\mathrm{d}) \cdot \mathrm{SST} + \beta_j(r_\mathrm{d}))$	MA03	bubbles (SST)	$r_\mathrm{d} \in [0.01\text{–}1.4]$ $\mathrm{SST} \in [271\text{–}298]$
$\alpha_j = \sum_{\xi=1,4} \alpha_{j,\xi}(2r_\mathrm{d})^\xi, \beta_j = \sum_{\xi=1,4} \beta_{j,\xi}(2r_\mathrm{d})^\xi$ $r_\mathrm{d} \in (0.01, 0.0725) \rightarrow j = 1$ $r_\mathrm{d} \in (0.0725, 0.2095) \rightarrow j = 2$ $r_\mathrm{d} \in (0.2095, 1.4) \rightarrow j = 3$			
$\frac{\mathrm{d}F_N^{(\mathrm{emi})}}{\mathrm{d}r}\vert_{\mathrm{M86SM93}} = \begin{cases} \max\left(\frac{\mathrm{d}F_N^{(\mathrm{emi})}}{dr}\vert_{\mathrm{SM93}}, \frac{\mathrm{d}F_N^{(\mathrm{emi})}}{\mathrm{d}r}\vert_{\mathrm{M86}}\right) & \text{if } U_{10} \geq 9 \\ \frac{\mathrm{d}F_N^{(\mathrm{emi})}}{\mathrm{d}r}\vert_{\mathrm{M86}} & \text{if } U_{10} < 9 \end{cases}$	M86/SM93	bubbles, spume	
$\frac{\mathrm{d}F_N^{(\mathrm{emi})}}{\mathrm{d}r}\vert_{\mathrm{MA03M86SM93}} = \begin{cases} \frac{\mathrm{d}F_N^{(\mathrm{emi})}}{\mathrm{d}r}\vert_{\mathrm{MA03}} & \text{if } r_\mathrm{d} \leq 1.4 \\ \frac{\mathrm{d}F_N^{(\mathrm{emi})}}{\mathrm{d}r}\vert_{\mathrm{M86SM93}} & \text{if } r_\mathrm{d} > 1.4 \end{cases}$	MA03/M86/SM93	bubbles (SST), spume	
$\frac{\mathrm{d}F_N^{(\mathrm{emi})}}{\mathrm{d}r_{80}}\vert_{\mathrm{J11}} = \frac{\mathrm{d}F_N^{(\mathrm{emi})}}{\mathrm{d}r_{80}}\vert_{\mathrm{G03}} \cdot \gamma(\mathrm{SST})$	J11	bubbles (SST), spume	$r_{80} \in [0.07\text{–}20]$ $\mathrm{SST} \in [273.15 - 303.15]$
$\gamma = 0.3 + 0.1(\mathrm{SST} - 273.15) - 0.0076(\mathrm{SST} - 273.15)^2 + 0.00021(\mathrm{SST} - 273.15)^3$			

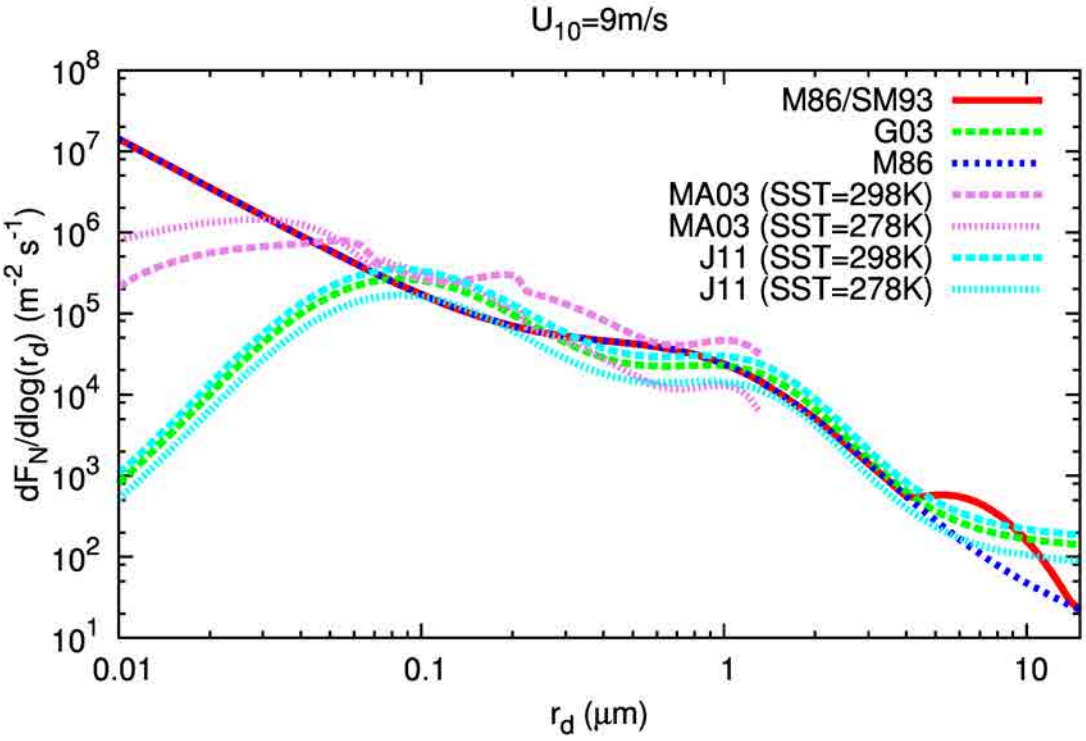

Figure 2: Sea-salt number emission flux at 10 m as a function of particle dry radius with the different emission schemes (color lines). U_{10} and r_{d} stand for wind speed at 10 m and dry radius, respectively.

duction is not described in M86 and MA03, while it is represented in SM93 (Fan and Toon, 2011), and its treatment in G03 is unclear (and, as a consequence, in J11). This leads to significant differences in emission fluxes of large particles (Fig. 2).

In addition, the above parameterizations were merged to obtain more comprehensive schemes, such as the combined M86/SM3 and MA03/M86/SM93 (Table 3). Hoppel et al. (2002) concluded that M86/SM93 may be considered as the best candidate to describe sea-salt emissions in the interval 0.15 mum to 15 μm in dry radius. M86/SM93 was then extended to ultrafine particles in other studies (Caffrey et al., 2006; Fan and Toon, 2011).

In this work, we also combined M86/SM93 and MA03 to account for the the SST effect upon sea-salt production. In MA03/M86/SM93, MA03 is applied within its range of validity and replaced by M86/SM93 beyond that range (i.e., for large particles with $r_\mathrm{d} > 1.4\,\mu$m). We find a similar attempt in the work of Tsyro et al. (2011), where MA03 is combined with M86 (but not with the spume production of SM93).

We choose an upper cutoff for the particle size around the maximum value allowed by the sea-salt production parameterizations implemented in our module. To perform a consistent comparison, we consider a range of [0.1–15] μm in dry radius for all the emission schemes, which implies an extension of M86, G03, and J11 schemes beyond their formulation intervals. Because some schemes work with wet radius r_{80} and others with dry radius r_d, we assume $r_{80} = 2r_\mathrm{d}$ to obtain emission of dry particles following the water-uptake treatment (detailed in Section 2.2.1). Mass emission fluxes $F^{(\mathrm{emi})}$ are calculated from number fluxes $F_N^{(\mathrm{emi})}$ as

$$F_k^{(\mathrm{emi})} = \int_{\mathrm{bin}-k} \frac{\mathrm{d}F_N^{(\mathrm{emi})}}{\mathrm{d}r_\mathrm{d}} \cdot \frac{4\pi}{3}\rho_\mathrm{d} r_\mathrm{d}^3 \mathrm{d}r_\mathrm{d}. \tag{16}$$

The emission mechanism is not explicitly coupled with the viscous sub-layer of the NMMB. However, the calculation of friction velocity and wind speed at 10 m depends on the viscous sub-layer scheme in the surface layer.

3.1.3 Experimental design

We performed global simulations between 2002 and 2006 and additional simulations covering the temporal windows of the cruises. The horizontal resolution used is 1°x1.4°. 24 vertical layers are employed and the dynamics time step is $\Delta t = 120$ s. Meteorological conditions are initialized every 24 h using the NCEP final analyses (FNL) at 1°x1° for year $\geq$ 2000 and the NCEP Global Data Assimilation System analysis (GDAS) at 2.5°x2.5° prior to year 2000. A spinup of 1 month for sea-salt is assumed at the beginning of each simulated period. The model output is taken every 6 h to calculate monthly averages and every 1 h when comparing with cruise observations.

The five implemented emission schemes are compared with comprehensive data sets of observations dispersed over the globe. For this comparison we use a coarse AOD calculated by applying a lower cutoff value of 0.6 μm (i.e. the AERONET submicron cutoff) of the wet particle radius. In our description, this value is equivalent to a lower cutoff of the dry particle radius $\bar{r}_\mathrm{d}$ given by

$$\bar{r}_\mathrm{d} = 0.6\,\mu m/\phi(\mathrm{RH}). \tag{17}$$

At maritime atmospheric conditions (RH = 80 %), the submicron bins significantly contribute to the coarse AOD. Sub-bin contributions to the coarse AOD are calculated assuming the log-normal distribution of Lewis and Schwartz (2004). In this contribution, the model coarse AOD

is calculated from the dust and sea-salt components allowing the use of AERONET stations affected by dust to be included in the evaluation.

Feedback processes between aerosols and radiation are not considered in any of the simulations.

At each evaluation site we also compare the simulated wind speed with a 30 yr climatology (1981–2010) derived from the NCEP/NCAR reanalysis data set (Kalnay et al., 1996) to evaluate the representativeness of our 5 yr wind speed climatology.

3.1.4 Observational data

Figure 3 displays the location of measurement sites and cruise measurement trajectories used in the model evaluation. Names and coordinates of the sites are listed in Table 4. Quantities evaluated are sea-salt surface concentrations and AOD. For the station data we use monthly climatologies to compare with our simulated 5 yr period (2002–2006).

We consider AERONET sun photometer measurements as the reference to evaluate the modeled sea-salt AOD. Even if algorithms tend to minimize biases due to cloud cover and other effects (e.g. Zhang and Reid, 2006), estimates from satellites remain highly uncertain and are not used in this contribution. Satellite overestimation can reach up to 0.07 in island stations compared to monthly AERONET-derived AOD (Jaeglé et al., 2011). At certain latitudes, the bias between satellite and ship AOD measurements may range from -0.2 to $+0.2$ (Smirnov et al., 2011). These biases exceed the typical sea-salt AOD value in the remote marine environment ($\sim$ 0.07, see Smirnov et al., 2011). AOD measurements from the AERONET Maritime Aerosol Network (MAN) are not used in this Section because of complexities in disentangling sea-salt and dust contributions from other aerosol species (such as carbonaceous and sulfate aerosols) that are not implemented in the module at this step of development.

NOAA/PMEL cruises. Sea-salt cruise measurements are considered, specifically ion concentrations from two cruises of the NOAA/PMEL: AEROINDOEX in 1999, spanning the Atlantic and the Indian Oceans, and ACE1 in 1995, crossing the Pacific Ocean. Concentrations of both Na^+ and Cl^- were measured by ion chromatography (Quinn et al., 1998) at 18 m above the sea surface. The experimental aerodynamic cutoff diameter was 10 μm for all cruises. Instruments were kept at constant RH values during measurements. Based on these values, Jaeglé et al. (2011) assumed a dry radius cutoff of 3 μm for AEROINDOEX and ACE1. Hence, we use the first 6 dry model bins for the comparison. The ACE1 and AEROINDOEX data sets also provide wind speed measurements at 33 m and 14 m above sea surface, respectively.

The spatial scale of the cruise measurements is around 600 km since they were averaged over temporal windows ranging from 2 to 24 h; mean ship speeds were around 24 km h^{-1}.

U-MIAMI surface concentrations. The U-MIAMI network supplied aerosol measurements from around 35 stations worldwide between the early 1980s and 1996 (Savoie and Prospero, 1977). Aerosols were collected with high-volume filter samplers and different measurement protocols were employed depending on the measurement site. We use climatologies from 15 stations (Fig. 3 and Table 4). These stations grant good data quality and are not affected by surf-zone production (J. Prospero, personal communication, 2012). The observed

Table 4: List of the observational sites used in this Section, classified by network.

Code	Database	Station	lat	lon
		AOD500 nm		
1	AERONET	Amsterdam Island	37.81° S	77.57° E
2	AERONET	Ascension Island	7.98° S	14.41° W
3	AERONET	Azores	38.53° N	28.63° W
4	AERONET	Bermuda	32.37° N	64.70° W
5	AERONET	Cape San Juan	18.38° N	65.62° W
6	AERONET	Ceilap-RG	51.60° S	69.32° W
7	AERONET	Coconut Island	21.43° N	157.79° W
8	AERONET	Crozet Island	46.43° S	51.85° E
9	AERONET	Dunedin	45.86° S	170.51° E
10	AERONET	Guam Island	13.43° N	144.80° E
11	AERONET	La Parguera	17.97° N	67.04° W
12	AERONET	Midway Island	28.21° N	177.38° W
13	AERONET	Nauru	0.52° S	166.92° E
14	AERONET	Reunion Island	20.88° S	55.48° E
15	AERONET	Rottnest Island	32.00° S	115.50° E
16	AERONET	Tahiti	17.58° S	149.61° W
		sulfateRFACE CONCENTRATIONS		
a	U-MIAMI	Baring Head	41.28° S	174.87° E
b	U-MIAMI	Bermuda	32.27° N	64.87° W
c	U-MIAMI	Cape Grim	40.68° S	144.68° E
d	U-MIAMI	Cape Point	34.35° S	18.48° E
e	U-MIAMI	Chatam Island	34.92° S	176.50° W
f	U-MIAMI	Fanning Island	3.92° N	159.33° W
g	U-MIAMI	Invercargill	46.43° S	168.35° E
h	U-MIAMI	King George Island	62.18° S	58.30° W
i	U-MIAMI	Marion Island	46.92° S	37.75° E
l	U-MIAMI	Miami	25.75° N	80.25° W
m	U-MIAMI	Midway Island	28.22° N	177.35° W
n	U-MIAMI	Oahu	21.33° N	157.70° W
o	U-MIAMI	Palmer	64.77° S	64.05° W
p	U-MIAMI	Reunion Island	21.17° S	55.83° E
q	U-MIAMI	American Samoa	14.25° S	170.58° W

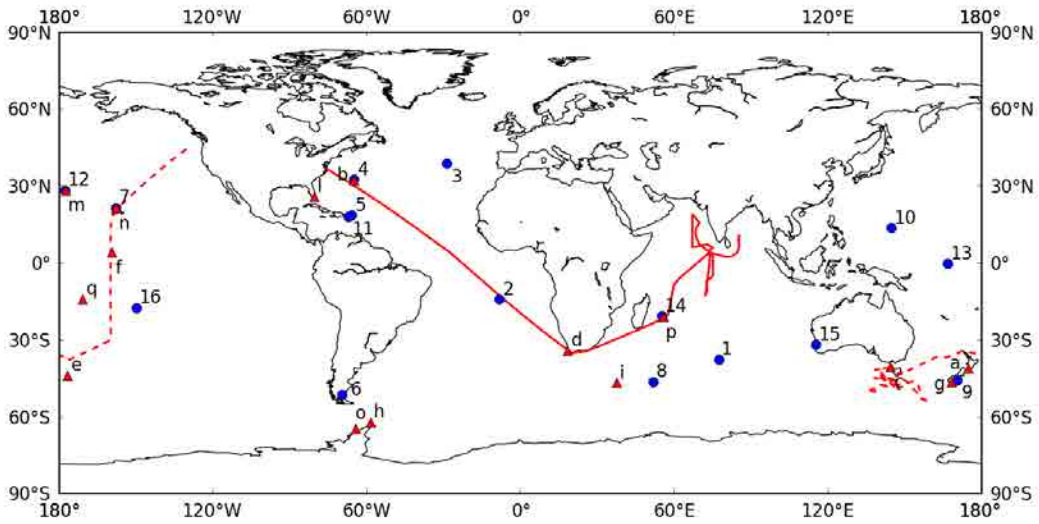

Figure 3: Observational data sets used for the model evaluation: blue circles refer to AOD measurements from AERONET, red triangles to surface concentration measurements from the U-MIAMI network; red lines refer to cruise measurement trajectories from AEROINDOEX (solid line), and ACE1 (dashed line).

sea-salt mass concentrations ($\mu g\,m^{-3}$) were computed as $sea-salt = Cl^- + 1.47Na^+$ following Quinn and Bates (2005) where both Cl^- and Na^+ measurements were available, and as $sea-salt = 3.252Na^+$, where only Na^+ concentrations were supplied (J. Prospero, personal communication, 2012). Since U-MIAMI measurements are not constrained by an upper cutoff radius, we perform the comparison with the complete set of model bins.

AERONET AOD. AERONET provides automatic ground-based observations from sun photometers in a large number of stations around the globe (Holben et al., 1998; Smirnov et al., 2000). The accuracy of AERONET sun photometers is 0.01 for AOD (Holben et al., 1998; Smirnov et al., 2000). We considered a set of 16 sea-salt-dominated stations as proposed by Jaeglé et al. (2011) (Fig. 3 and Table 4). The three requirements fulfilled by the stations are sea-salt contributions to the total AOD greater than 50 % as predicted by GEOS-CHEM model, availability of Level 2 quality-assured data for all the considered time ranges, and at least 3 yr of data supporting the monthly climatologies. The evaluation is performed against monthly climatologies of the AOD at 500 nm. In particular, we focus on the AOD coarse fraction, therefore limiting the influence of fine aerosol species.

3.1.5 Results and discussion

Global sea-salt distribution and total budgets. Fig. 4 displays the global distribution of simulated sea-salt production, surface concentration, and AOD at 500 nm in January and August with M86/SM93. We observe a pronounced asymmetry in the summer-to-winter variation between the two hemispheres and four large regions of maximum production. The two largest monthly peaks are found in regions with enhanced westerlies, i.e., beyond the

horse latitudes (lat > 30° N and lat < 30° S). Also two local maxima can be observed in correspondence with the trade winds, next to the intertropical convergence zone (around 10° N and 10° S). While sea-salt production at the southern belt only moderately changes with season, the northern belt is affected by strong variations during the year with increases in boreal winter well above +200 % with respect to boreal summer. It is well known that these seasonal fluctuations are related to the asymmetric variation of the global wind speed pattern, driven by the variation of the global atmospheric angular momentum (Sandwell and Agreen, 1984).

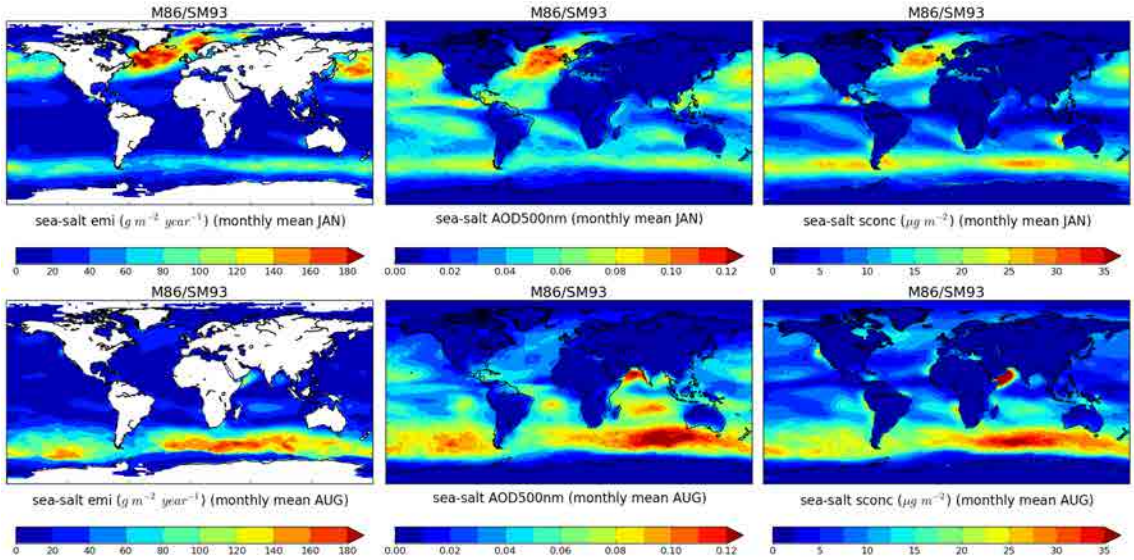

Figure 4: Seasonal regimes of sea-salt emission (left panels), AOD at 500 nm (middle panels), and surface concentration (right panels) with M86/SM93. January and August averages of a 5 yr period (2002–2006) are shown. The label emi refers to emission flux, and sconc refers to surface concentration.

Sea-salt production and surface concentration over the Pacific around 10° N is about half the values found at higher latitudes. Yet, the AOD reaches monthly mean values close to the global maximum. Because of the seasonal movement of the Intertropical Convergence Zone,

the region around 10° N in the Pacific is characterized – during winter – by infrequent precipitation and low wet scavenging rate increasing particle lifetime, in contrast to the strong production belts characterized by wet extratropical cyclone activity. The RH-dependent particle size and optical properties in the model also play a relevant role in determining the AOD peaks close to the intertropical convergence zone. Surface concentration and AOD maximum values in the Arabian Sea during the boreal summer are due to the strong southwestern winds of the monsoon circulation.

Figure 5 displays maps of annual mean sea-salt emission, surface concentration, and AOD with the five emission schemes. The two maximum production regions beyond the horse latitudes are the most sensitive to the choice of the emission scheme. G03 produces the highest concentrations with peaks above 35 μg m^{-3} in the southern belt and over 25 μg m^{-3} in the northern belt. Differences in spume production representation are clear when comparing the simple M86 with M86/SM93, for which the mean concentration is enhanced due to wind episodes exceeding the threshold $U_{10} > 9\,\mathrm{m\,s^{-1}}$. The relative importance of the production regions changes if SST effects are included in the emission scheme. The SST dependence

in MA03/M86/SM93 produces a latitudinal modulation of the emission fluxes and surface concentration with relative enhancement in the tropics and reduction elsewhere. This effect is amplified with J11, leading to a change in maximum values of surface concentration from the high-latitude belts to the tropics. In particular, an absolute maximum value above 35 μg m^{-3} is found over the Arabian Sea.

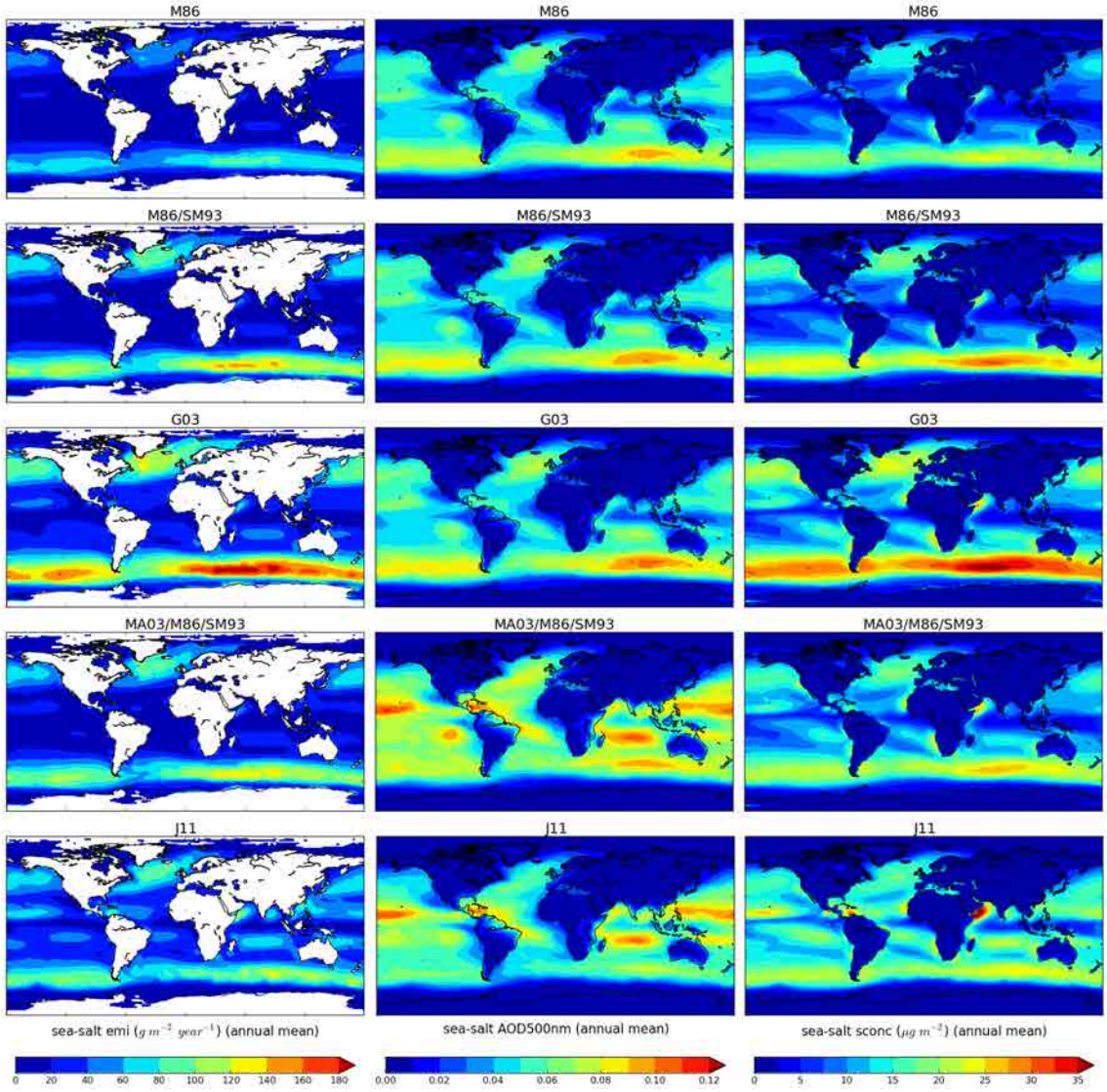

Figure 5: Annual mean values of sea-salt emission (left panels), AOD at 500 nm (middle panels), and surface concentration (right panels), depending on the emission scheme (from top to bottom: M86, M86/SM93, G03, MA03/M86/SM93, and J11). Averages of a 5 yr period (2002–2006) are shown. The label emi refers to emission flux and sconc refers to surface concentration.

Sea-salt AOD patterns with M86, M86/SM93, and G03 are very similar. The southern belt dominates with peaks around $\sim$ 0.1. Peak values around $\sim$ 0.06 are found at high latitudes and the tropical Pacific. Relevant differences are observed with MA03/M86/SM93 for which absolute maximum values of 0.1 appear next to the intertropical convergence zone.

Table 5: Model sea-salt global budgets and lifetimes compared with other recent studies. The label emi stands for total accumulated emission of sea-salt mass ($\mathrm{Tg\,yr^{-1}}$); wetfrac = wetdep/(drydep + wetdep) where drydep accounts for both accumulated dry deposition and sedimentation ($\mathrm{Tg\,yr^{-1}}$) and wetdep for accumulated wet deposition ($\mathrm{Tg\,yr^{-1}}$); <load> is the annual mean column mass load ($\mathrm{Tg\,yr^{-1}}$), and lifetime =< load >/(drydep + wetdep) (h). All quantities obtained in our work are averaged over the simulation period 2002–2006 and indicated by the label o.w. The labels ALL, F1, C1, F2, and C2 refer to different dry radius intervals (μm).

			ALL (0.1–15)			F1 (0.1–1)		C1 (1–4)		F2 (0.1–0.5)		C2 (0.5–4)	
	Study	emi	<load>	life	wetfrac	emi	life	emi	life	emi	life	emi	life
M86	o.w.	3888	5.0	11.3	0.486	499	27.7	2033	14.7	75	28.7	2457	16.7
M86/SM93	o.w.	5440	5.6	8.9	0.467	499	27.7	2172	14.8	75	28.7	2595	16.8
G03	o.w.	8114	6.7	7.3	0.400	372	24.7	2465	12.2	57	26.1	2781	13.9
MA03/M86/SM93	o.w.	5419	6.5	10.4	0.466	266	32.5	1997	17.2	48	33.6	2215	19.5
J11	o.w.	6514	7.2	9.6	0.368	298	34.9	1979	16.5	46	37.1	2233	19.0
M86[1]	Tsigaridis et al. (2013)					471	32.6	1916	26.6				
G03[1]	Tsigaridis et al. (2013)					357	32.6	2327	26.9				
J11[1]	Tsigaridis et al. (2013)					310	31.9	2019	26.6				
G03[2]	Jaeglé et al. (2011)	5200	4.7	7.9	0.356					67	26.2	2533	11.3
J11[2]	Jaeglé et al. (2011)	4600	4.4	8.4	0.402					59	24.7	2229	12.0
AEROCOM A median[3]	Textor et al. (2007)	3830	6.5	7.2	0.210								
AEROCOM A mean[3]	Textor et al. (2007)	8200	7.9	12.0	0.210								
AEROCOM A stddev[3]	Textor et al. (2007)	8200	5.4	7.1	0.122								
AEROCOM B median[3]	Textor et al. (2007)	7740	12.0	14.4	0.282								
AEROCOM B mean[3]	Textor et al. (2007)	7720	12.7	12.0	0.253								
AEROCOM B stddev[3]	Textor et al. (2007)	231	3.9	1.7	0.114								

[1] 2 modes: $r_\mathrm{d} \in [0.1\text{–}1]\,\mu$m and $r_\mathrm{d} \in [1\text{–}4]\,\mu$m
[2] 3 modes: $r_\mathrm{d} \in [0.01\text{–}0.5]\,\mu$m, $r_\mathrm{d} \in [0.5\text{–}4]\,\mu$m, and $r_\mathrm{d} \in [4\text{–}10]\,\mu$m
[3] models participating in AEROCOM experiments use different parameterizations and aerosol size

These peaks overestimate the maximum AOD from ship measurements gathered by Smirnov et al. (2011) both in the remote tropical Pacific (0.07 for total AOD at 500 nm) and the Indian Ocean (0.06, east of Madagascar). The use of the J11 scheme leads to an AOD pattern and peak values very similar to MA03/M86/SM93, with an enhancement of the SST latitudinal modulation.

Table 5 lists the annual model budgets from the different emission schemes and other recent studies. To achieve a consistent comparison, we specify values for five size intervals: all bins (ALL), fine bins up to 1 μm (F1), fine bins up to 0.5 μm (F2), coarse bins from 1 μm to 4 μm (C1), and coarse bins from 0.5 μm to 4 μm (C2).

Total emission, burden, and lifetime are sensitive to the parameterization of the emission flux. Lifetime ranges from 7.3 h with G03, which produces large spume particles independently from wind conditions, to 11.3 h with the simple M86, which neglects spume production.

Despite the decrease in total emissions, SST-dependent schemes lead to an enhancement of sea-salt lifetime, both in the case of MA03/M86/SM93 (with respect to M86/SM93) and J11 (with respect to G03). This effect was also observed in Jaeglé et al. (2011), where lifetime values are close to ours. However both fine (F1 and F2) and coarse (C1 and C2) lifetimes significantly increase with J11 compared to G03, in contrast to Jaeglé et al. (2011) and Tsigaridis et al. (2013). This may be related to different treatments of water uptake, deposition, and particle size distribution in the models.

With respect to AEROCOM experiments, the major difference is found in the wet deposition fraction, which is around 0.4 in our model and between 0.2 and 0.3 in AEROCOM A and B median models. In particular, J11 produces the most compatible value with the AEROCOM inter-model variability.

Our simulated annual mean column mass load (ranging from 5.0 Tg to 7.2 Tg) is only slightly larger than the value of Jaeglé et al. (2011) and it is close to the AEROCOM Experiment A median value and about half of Experiment B (12.0 Tg) (Textor et al., 2006).

Emission is very sensitive to the upper size cutoff value and ranges from 3888 $\mathrm{Tg\,yr^{-1}}$ to

$8114\,\mathrm{Tg\,yr^{-1}}$.

Modeled surface concentrations compared with cruise data. Cruise measurements allow a comparison with model at timescales of 2–24 h. Each measurement gathered by the vessels was averaged on space and time, thus simulated values may be affected by errors due to the adopted averaging technique. We remap the original lat/lon grid at resolution Δxx$Deltay$ (1°x1.4°) to a coarser resolution ($\Delta x' = n\Delta x$, $\Delta y' = n\Delta y$), matching the characteristic spatial length of the cruise under consideration. The number n is defined as the smallest integer satisfying the following conditions:

$$V_{\mathrm{cruise}} \cdot \max(T_{\mathrm{obs}}) < n\Delta x \tag{18}$$

$$V_{\mathrm{cruise}} \cdot \max(T_{\mathrm{obs}}) < n\Delta y, \tag{19}$$

where V_{cruise} is the vessel mean speed during the cruise and T_{obs} is the observation duration, which is not constant. In this way, the spatial extent of each measurement is represented by a single lower resolution grid cell. We use $n = 2$ for AEROINDOEX and $n = 4$ for ACE1. Model outputs every 1 h are then averaged over each measurement period. Cruise trajectories are displayed in Fig. 3. We recall that the values shown in this comparison refer to an upper cutoff of 3 μm in dry radius, thus we investigate the model's ability to simulate the concentration within the first 6 bins. In this case the M86/SM93 scheme is equivalent to M86, since the larger particles produced by spume cutting are not taken into account due to the observational cutoff.

Figures 6 and 7 show a good correlation for AEROINDOEX and a lower correlation for ACE1. Results are similar to those obtained in Jaeglé et al. (2011) and Witek et al. (2007) with GEOS-CHEM and NAAPS models, respectively. AEROINDOEX is simulated with a correlation close to 0.6 with M86, G03, and J11. The correlation decreases when employing the SST-dependent MA03/M86/SM93 (0.49). The mean normalized bias ranges from +0.4 % (MA03/M86/SM93) to −36.8 % (G03), showing an overall tendency of the model towards underestimation, mainly due to the misrepresentation of the peak around day 25. The mean normalized gross error is around 60 % for all cases.

For ACE1, the correlation is low (around 0.36) regardless of the emission scheme applied. The overall bias between model and observations ranges from −23.7 % (J11) to 26.3 % (M86), with J11 being the only scheme with a negative bias. The gross error is around 50 %. Because of the larger measurement timescales of ACE1, part of the errors may be due to the inefficiency of the averaging technique.

Figures 6 and 7 also display the simulated wind speed (at 14 m and 33 m), obtained by applying the power-law of Hsu et al. (1994) to U_{10}, observed wind speed, SST values, wet deposition and observed hourly precipitation. The measurements are 30 min-averages and the model output is taken every 1 h as an instantaneous value for both cruises. Wind speed is simulated with a high correlation for AEROINDOEX (0.73) and ACE1 (0.81) and biases (−8.5 %

and −3.7 %) and gross errors (24.2 % and 17.2 %) are rather low.

The plotted SST values highlight the corrections introduced by the SST-dependent emissions (MA03/M86/SM93 and J11) on their parent schemes (M86/SM93 and G03, respectively). For example, the higher SST values taking place during the first 30 days of ACE1 produce a marked increase in concentration.

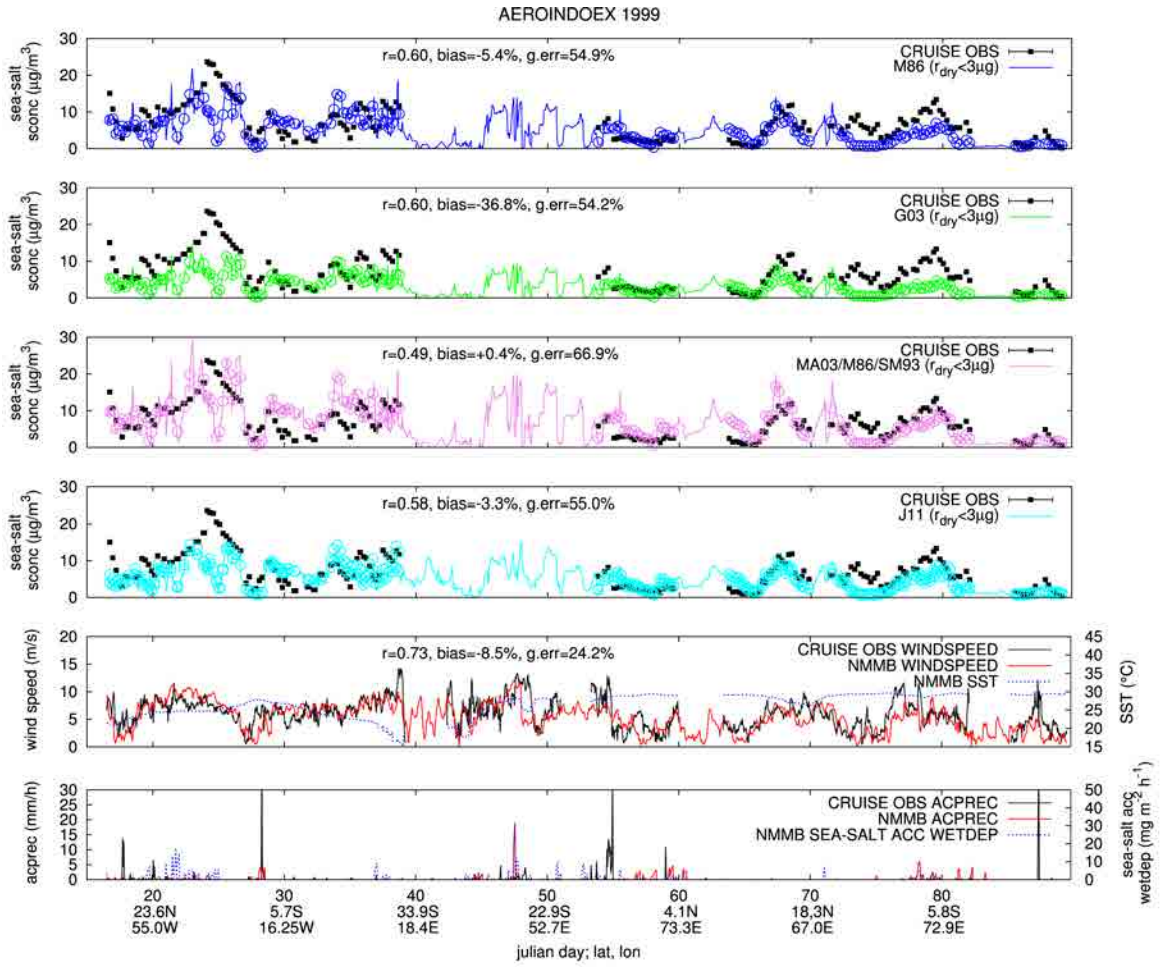

Figure 6: From top to bottom: simulated sea-salt surface concentration (sconc) with M86 (blue), G03 (green), MA03/M86/SM93 (violet), and J11 (cyan) compared to AEROINDOEX cruise measurements (black squares), simulated wind speed (red line) compared to AEROINDOEX measurements (black line) (simulated SST is also shown), and simulated precipitation (red line) compared to AEROINDOEX measurements (black line) (simulated accumulated wet deposition is also shown). M86/SM93 is not shown since it is equivalent to M86 for $r_d < 3\mu$m. The model 1 h-output surface concentrations are plotted with solid lines and averaged over the measurement times (circles). Skill scores shown are correlation (r), mean normalized bias (bias), and mean normalized gross error (g.err.).

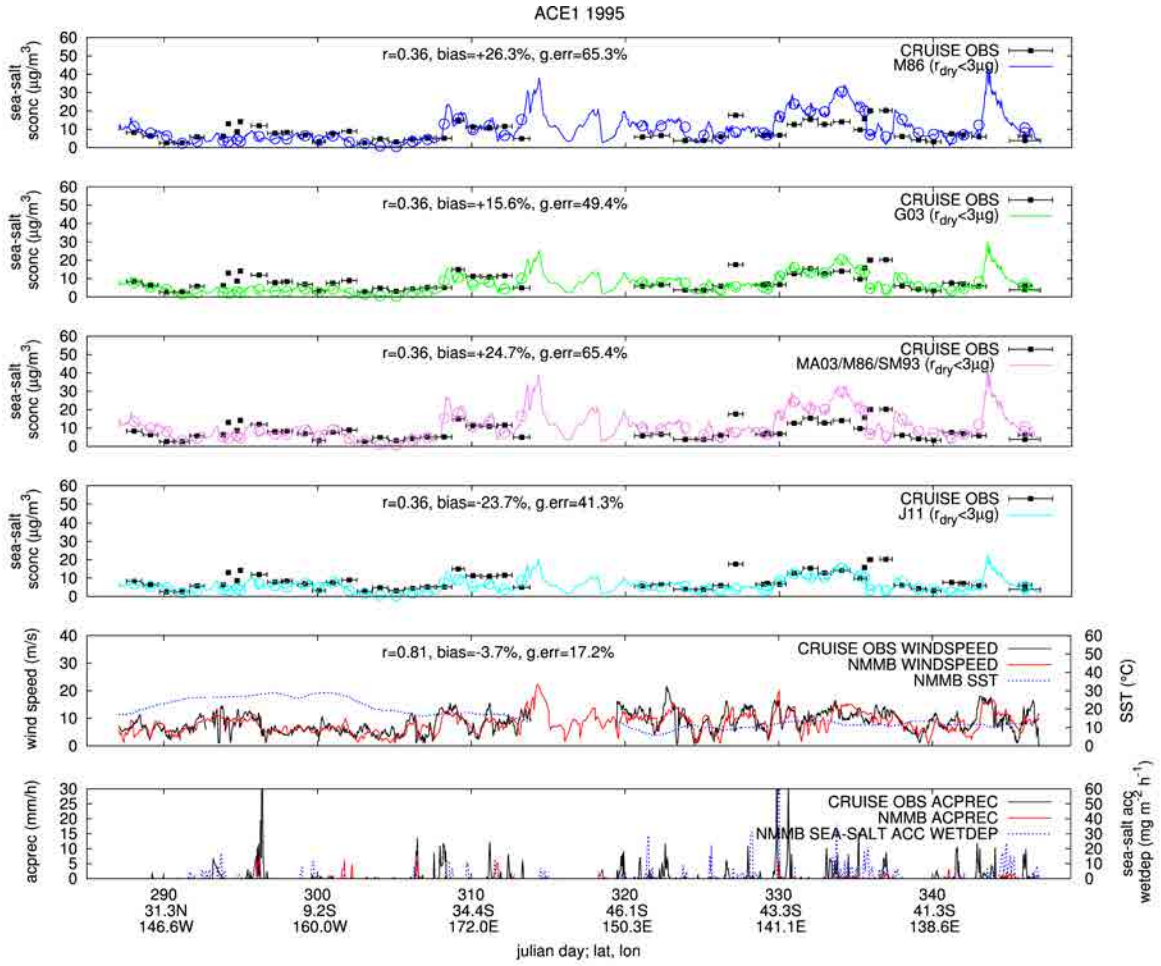

Figure 7: From top to bottom: simulated sea-salt surface concentration (sconc) with M86 (blue), G03 (green), MA03/M86/SM93 (violet), and J11 (cyan) compared to ACE1 cruise measurements (black squares), simulated wind speed (red line) compared to ACE1 measurements (black line) (simulated SST is also shown), and simulated precipitation (red line) compared to ACE1 measurements (black line) (simulated accumulated wet deposition is also shown). M86/SM93 is not shown since it is equivalent to M86 for $r_d < 3\mu$m. The model 1 h-output surface concentrations are plotted with solid lines and averaged over the measurement times (circles). Skill scores shown are correlation (r), mean normalized bias (bias), and mean normalized gross error (g.err.).

Simulated wet deposition peaks are generally in correspondence with peaks in observed precipitation, although the relative intensity may not always be well captured. Spurious precipitations and consequent wet deposition overestimation affect the concentration peak around day 25 of the AEROINDOEX campaign.

Model surface concentration at U-MIAMI measurement sites. Simulated surface concentration was compared with observed climatologies at 15 stations of the U-MIAMI network (Fig. 8). The discussion of the results is complemented by Fig. 9, where simulated wind speed is compared with a 30 yr wind speed climatology (1981–2010) derived from the NCEP/NCAR Reanalysis (Kalnay et al., 1996). We use this comparison in order to check the representativeness of our simulation temporal window (5 yr, 2002–2006) with respect to a more comprehensive model climatology.

Overall, simulated sea-salt concentrations are in good agreement with observations. Significant model overestimations of a factor of two or more are found in Invercargill (g), and Marion Island (i), where all schemes are above the observed mean plus one standard deviation. In these sites, overestimation cannot be attributed to an excess of wind speed compared with the NCEP/NCAR climatology (Fig. 9). A similar overestimation is found in Jaeglé et al. (2011) and Tsigaridis et al. (2013) in Marion Island (i) and in Invercargill (g) in Tsigaridis et al. (2013). Both studies use as well global models with an horizontal resolution greater than 1 degree. Since these sites are located in regions characterized by complex topography, we hypothesize that errors may be due in part to the low model resolution used.

In the Antarctic region, schemes show opposite performances in two stations close to each other. In Palmer (o), all schemes overestimate surface concentration with the exception of J11, which reproduces well the climatology. The overestimation of the wind speed with respect to the NCEP climatology does not entirely explain the behavior of M86, M86/SM93, G03, and MA03/M86/SM93. On the other hand, J11 leads to an underestimation of the observed climatology at King George Island (h) which cannot be attributed to wind speed. Contrasting results are found in this region when comparing our work with Jaeglé et al. (2011) and Tsigaridis et al. (2013).

Significant underestimation is found in Fanning Island (f) and American Samoa (q), both located in the tropical Pacific. In Fanning Island (f), the low concentration could be associated to an underestimation of the wind speed, in contrast to American Samoa (q), where the simulated wind speed matches the NCEP climatology. Observed concentration climatologies present large standard deviations during boreal winter in these sites, which is inconsistent with the low variability of the simulated or climatological wind speed, suggesting a poor representativeness of the observed mean concentration. Significant underestimation of the U-MIAMI climatological values in Fanning Island (f) and American Samoa (q) is also found in Jaeglé et al. (2011) and Tsigaridis et al. (2013).

There is a significant influence of the applied emission scheme upon modeled sea-salt surface concentrations. Even the introduction of SST-dependence in MA03/M86/SM93, which only affects the smaller bins (from 0.1 μm up to 1.4 μm in dry radius), makes a relevant contribution to the simulated concentration. Fig. 10 includes scatterplots of observed and simulated values (neglecting Invercargill (g) and Marion Island (i)) and a scatterplot of simulated wind speed and NCEP climatological values. Correlation, normalized bias, normalized gross error, and a linear regression fit are provided for each scatterplot. G03 generally overestimates the climatological monthly mean concentrations, while M86 underestimates. A significant

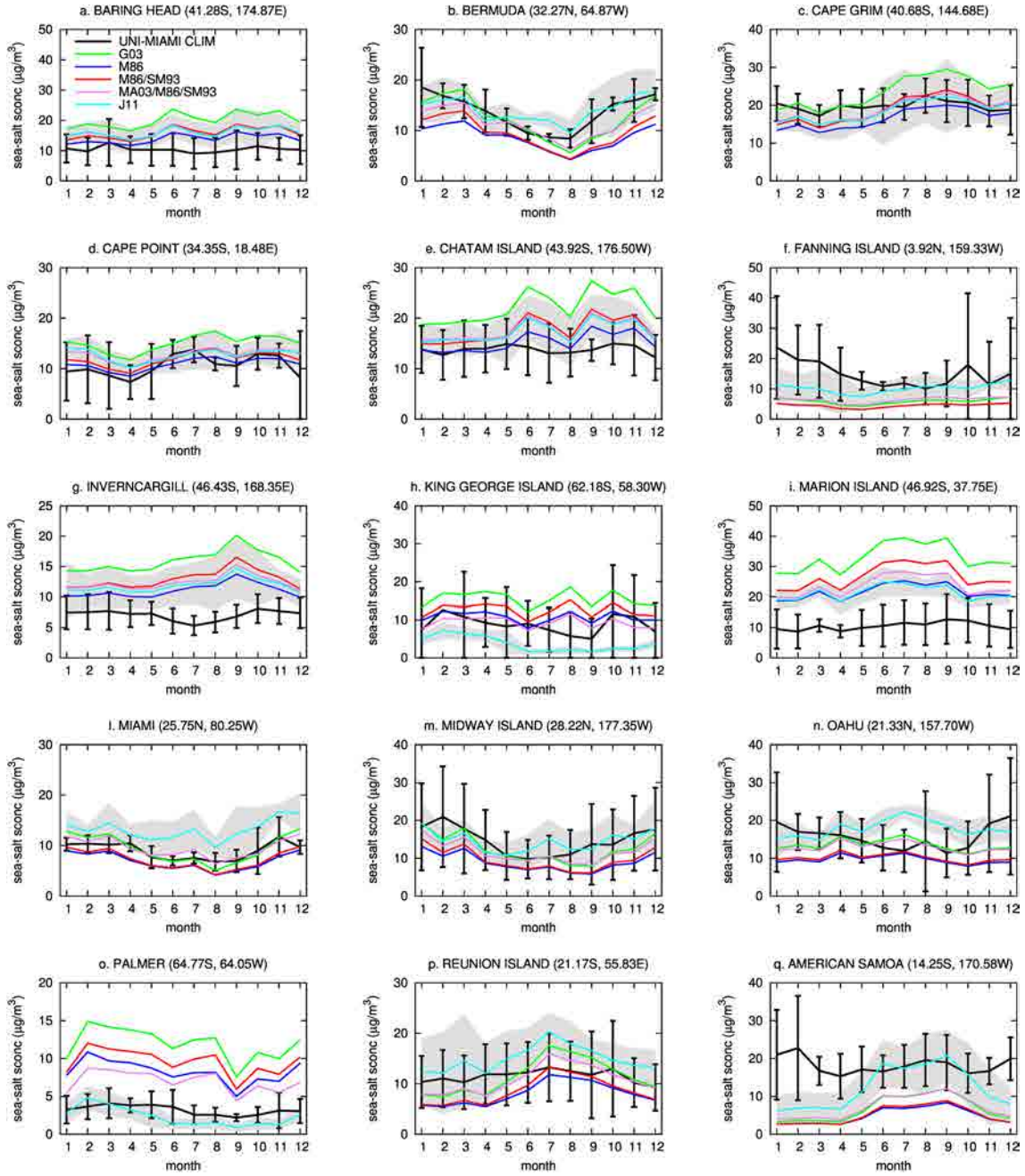

Figure 8: Monthly mean simulated (color lines) and observed (black lines) sea-salt surface concentration at U-MIAMI stations. Simulated values cover a 5 yr period (2002–2006). U-MIAMI climatologies include interannual standard deviation bars. J11 interannual standard deviation is also shown (shaded grey). The label CLIM stands for climatologies.

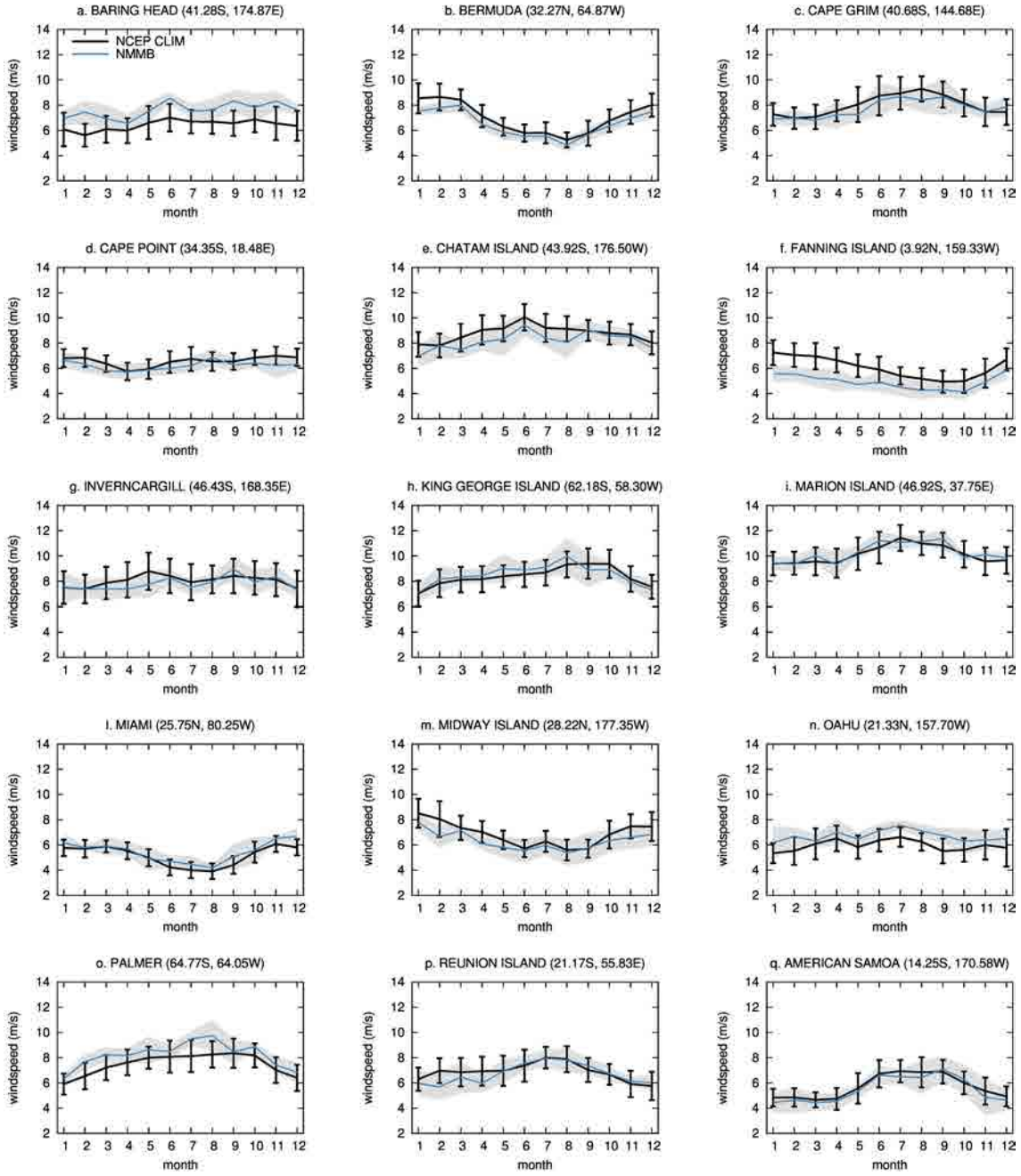

Figure 9: Monthly mean simulated surface wind speed (2002–2006) (blue) and surface wind climatologies (1981–2010) from NCEP/NCAR Reanalysis (black) at U-MIAMI stations. Interannual standard deviations are shown for the simulation (shaded grey) and the NCEP/NCAR climatology (black bars).

reduction in bias is obtained when using M86/SM93 instead of M86. The best agreement is obtained with the SST-dependent emission schemes MA03/M86/SM93 and J11. Overestimation with G03 may be explained by its unclear description of spume particles production, as already noted in Fan and Toon (2011). Indeed, the emission flux for particles larger than 10 μm in dry radius is nearly one order of magnitude larger than in the other implemented schemes (Fig. 2). On the other hand, the spume production is neglected in M86, which may partly explain the underestimated concentration. The introduction of spume particles in the combined M86/SM93 improves the model results. This improvement is more evident in stations and months characterized by frequent episodes of wind speed greater than 9 m s^{-1}, such as for example during January, February and March in Bermuda (b) (Fig. 8). In the tropics, where these episodes are infrequent, M86 and M86/SM93 provide similar results.

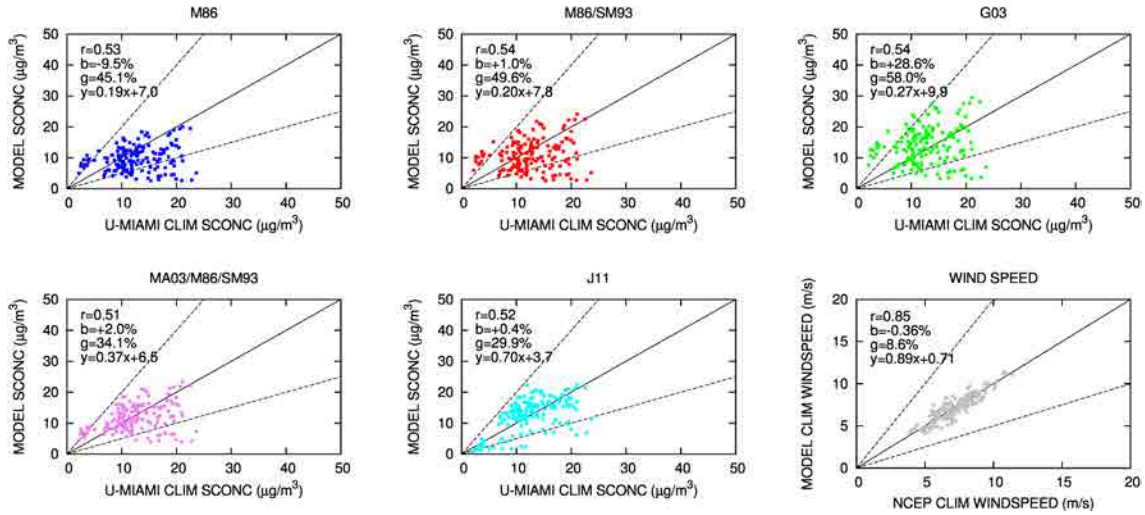

Figure 10: Scatterplots of simulated surface monthly mean concentrations and climatologies from the U-MIAMI network for each emission scheme. Invercargill (g) and Marion Island (i) stations have been excluded. A scatterplot of simulated surface wind speed and NCEP/NCAR climatology is provided in the bottom-right panel. The plots are accompanied by $y = 2^{\pm 1}x$ dashed lines. r, b, and g stand for overall mean correlation, normalized bias, and normalized gross error, respectively. A linear regression fit is also shown ($y = mx + q$).

The introduction of the SST-dependence in the emission scheme (both for MA03/M86/SM93 and J11) improves the overall statistics, with a reduction in bias and gross error (Fig. 10). The wind speed scatterplot suggests that biases could not be related to a weak representativeness of the simulated 5 yr period.

Aerosol optical depth. Simulated coarse AOD are compared with monthly climatologies at 16 AERONET sites (Fig. 11). The model AOD is all-sky in contrast to AOD measurements, which are clear-sky. The differences between all-sky and clear-sky results in models are currently uncertain and are thought to be moderate for sea-salt and very low for dust (Shindell et al., 2013).

To support the analysis, Fig. 12 displays the simulated wind speed and the NCEP wind speed climatology at each site. Overall, the simulated coarse AOD is in agreement with observations. Significant discrepancies are found in Ceilap-RG (6), Dunedin (9), Reunion Island (14), and Tahiti (16) with all schemes. Overestimation in Ceilap-RG (6) affects the

entire seasonal cycle mostly due to errors in dust emissions from South America. Neglecting the dust contribution, the nearly constant seasonal cycle and its mean value (~ 0.02) are well reproduced. Overestimation in Bermuda (4), Dunedin (9), Reunion Island (14), and Tahiti (16) takes place mainly during austral winter (JJA). At Bermuda (4), Dunedin (9), and Tahiti (16) model peaks may be partly related to an overestimated wind speed (Fig. 12).

Both at Reunion Island (14) and Dunedin (9) the significant dust contribution leads to uncertainties in the comparison. At Ascension Island (2), Bermuda (4), Cape San Juan (5), La Parguera (11), and Midway Island (12), the model's ability to reproduce the dust cycle is decisive for a proper simulation of the coarse AOD.

Results outline a close behavior among G03, M86 and M86/SM93, in contrast to SST-dependent schemes (MA03/M86/SM93 and J11). The latter tend to overestimate the AOD over warm sea surfaces in/near the tropics (e.g. Bermuda (4), Coconut Island (7), Guam Island (10), Midway Island (12), Reunion Island (14), and Tahiti (16)). These results are mainly related to differences in the emitted size-distribution and the hygroscopic growth of sub-micron aerosols affecting the coarse AOD. Figure 2 shows close to an order of magnitude difference in the number emission flux for particles with dry radius in the range 0.15–1.4 μm. Hygroscopic growth of particles above 0.6 μm adds up to explain the higher coarse AOD when using an SST-dependent scheme. Simulated wind speeds are stronger than NCEP climatological winds in Coconut Island (7), Guam Island (10), and Tahiti (16) (Fig. 12), which may also partly explain the overestimation in these sites. On the contrary, in Bermuda (4), Midway Island (12), and Reunion Island (14) the simulated wind speed is lower than the NCEP climatology.

In the subset of stations in/near the tropics, Jaeglé et al. (2011) found that their model generally underestimates the observed climatologies and the introduction of a SST-dependent term leads to an improvement of their model performance. In our work, we also find an increase in AOD at low latitudes when applying SST-dependent emission schemes, although it produces an overestimation of AERONET climatologies.

Figure 13 displays scatterplots of simulated and observed coarse AOD, excluding Ceilap-RG (6) due to the significant errors in the dust component. MA03/M86/SM93 and J11 produce the largest positive biases (+38.8 % and +27.5 %, respectively) and gross errors (above 40 %). The wind speed scatterplot indicates that such overestimation cannot be explained by a wind speed overestimation.

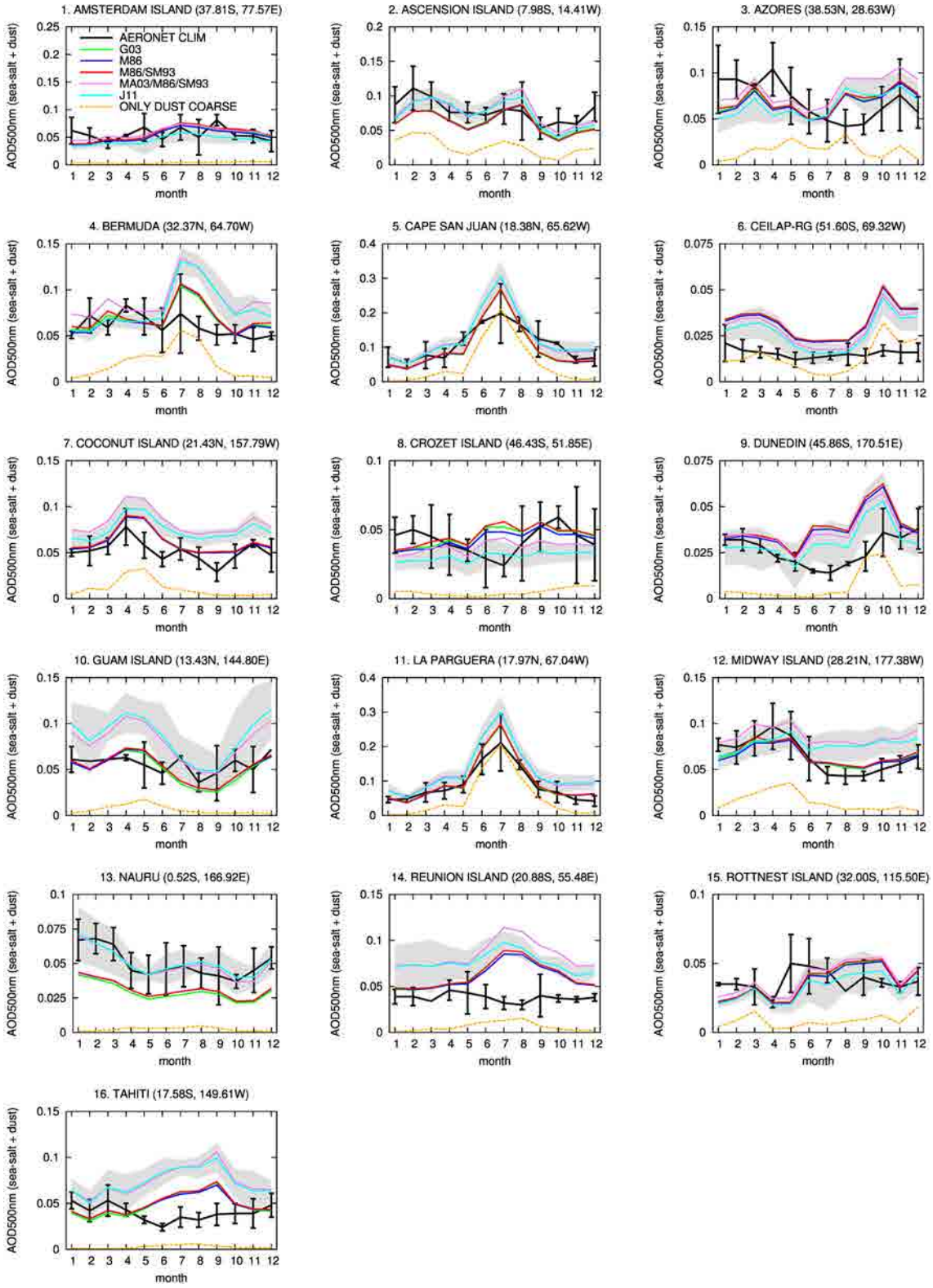

Figure 11: Monthly mean simulated sea salt + dust coarse AOD at 500 nm (color lines) and observed coarse AOD at 500 nm (black lines) at selected AERONET stations. Simulated values refer to averages over the simulated 5 yr period (2002–2006). AERONET climatologies include interannual standard deviation bars. J11 interannual standard deviation is also shown (shaded grey). The dust contribution is highlighted with the orange line. The label COARSE stands for coarse fraction of AOD; the label CLIM stands for climatologies.

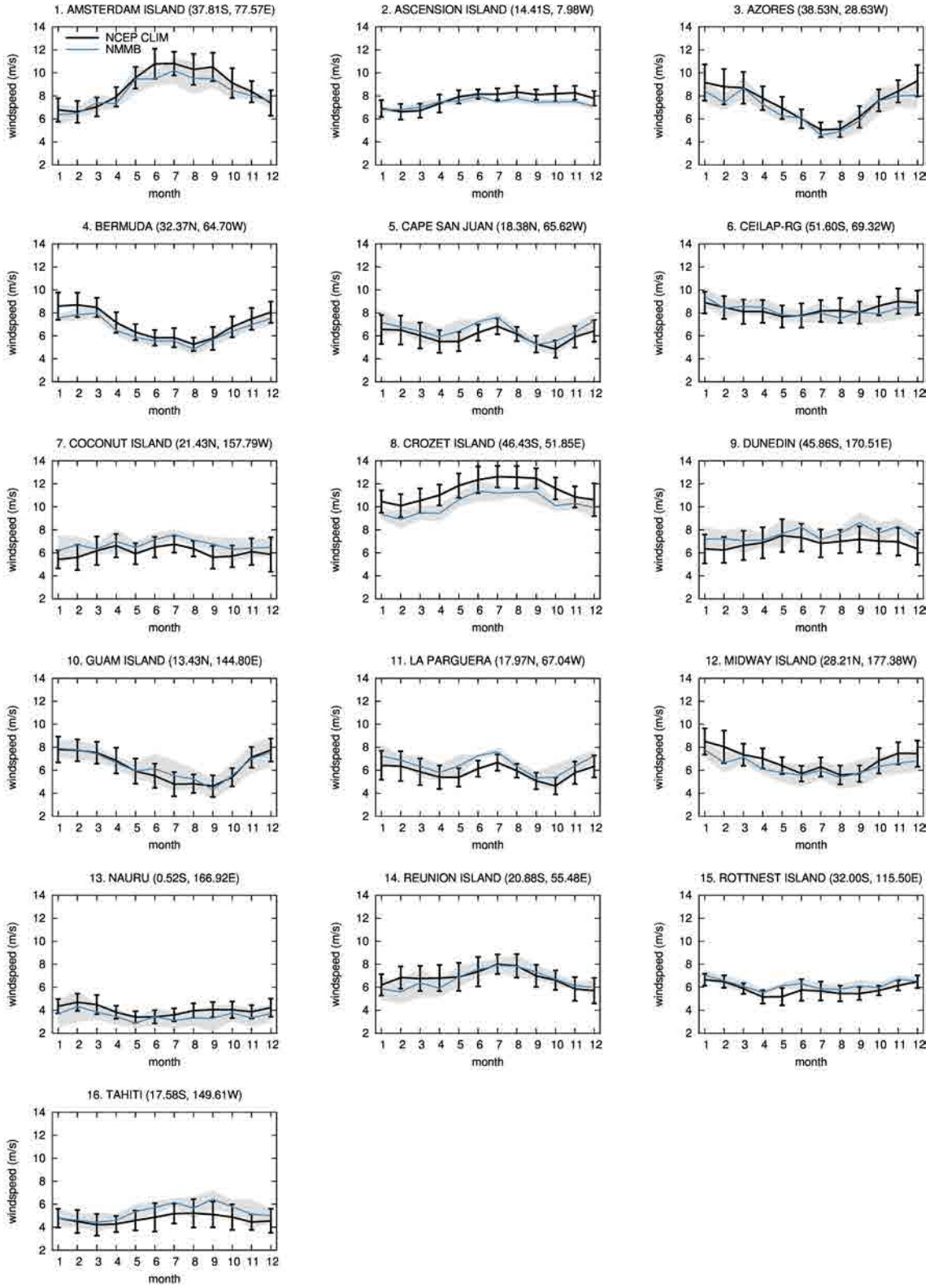

Figure 12: Monthly mean simulated surface wind speed (2002–2006) (blue) and surface wind climatologies (1981–2010) from NCEP/NCAR Reanalysis (black) at selected AERONET stations. Interannual standard deviations are shown for the simulation (shaded grey) and the NCEP/NCAR climatology (black bars).

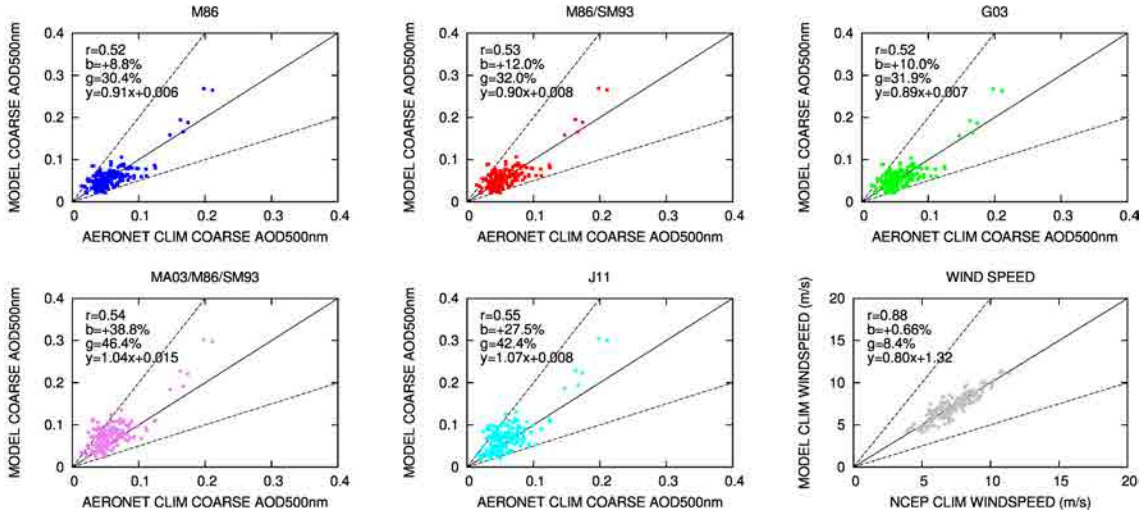

Figure 13: Scatterplots of simulated sea-salt+dust coarse AOD at 500 nm and climatologies from the AERONET network for each emission scheme. Ceilap-RG (6) has been excluded, since the dust errors affecting its region. A scatterplot of simulated surface wind speed and NCEP/NCAR climatology is provided in the bottom-right panel. The plots are accompanied by $y = 2^{\pm 1}x$ dashed lines. r, b, and g stand for overall mean correlation, normalized bias, and normalized gross error, respectively. A linear regression fit is also shown ($y = mx + q$).

3.2 On the evaluation of global sea-salt aerosol models at coastal/orographic sites

Modeling studies have attempted to constrain the sea-salt aerosol life-cycle, specially focusing on the sea-salt source function, which represents the largest source of uncertainty (Gong, 2003; Mårtensson et al., 2003; Lewis and Schwartz, 2004; Clarke et al., 2006; Caffrey et al., 2006; Jaeglé et al., 2011; Fan and Toon, 2011; Grythe et al., 2013; Partanen et al., 2014). Sea-salt source functions in global models are constrained and/or evaluated with AOD observations from satellites and Sun photometers, wind speed and surface concentration measurements from experimental campaigns (Quinn and Bates, 2005), and surface concentration climatologies at coastal stations from the University of Miami Network (UNI-MIAMI) (Savoie and Prospero, 1977). The UNI-MIAMI measurements represent the most comprehensive and used global climatological dataset of sea-salt surface concentration. Global model studies use a subset of the UNI-MIAMI coastal stations that are barely affected by local surf conditions (i.e. local production by breaking waves) and thus considered representative of open ocean conditions.

In a recent work, Jaeglé et al. (2011) showed that the discrepancy with observations of a model including a widely used source function based on a power law dependence on wind speed (Gong, 2003) was a strong function of SST. Using cruise observations to derive an empirical source function depending on both wind speed and SST, Jaeglé et al. (2011) obtained model bias reductions of nearly a factor of two for both cruise and station observations. Although the fitted parameters in the source function of Jaeglé et al. (2011) are model dependent, Tsigaridis et al. (2013) and Spada et al. (2013) (Section 3.1) recently tested the source function and found improved agreement with surface concentration observations in comparison to a number of other schemes. However, simulations remain affected with uncertainties

up to a factor of 2 or more. For example, Spada et al. (2013) found positive systematic biases of a 100% or more in Baring Head, Chatam Island, Invercargill and Marion Island, regardless of the source function applied in a global model at 1°x1.4° resolution. Simulations included a variety of combined source functions including the schemes of Gong (2003), Monahan et al. (1986), Smith et al. (1993), Mårtensson et al. (2003), and Jaeglé et al. (2011). Similarly, Tsigaridis et al. (2013) found strong overestimations in these stations, with most of the simulated monthly mean concentrations greater than the measured climatological values plus one standard deviation. In Jaeglé et al. (2011) a positive bias of about 100% was found in Marion Island, while negative biases in Baring Head and Invercargill were more pronounced when using the SST-dependent source function. Regardless of the source function or global model used, the annual trend in Invercargill is not well captured (e.g. Liu et al. (2005); Jaeglé et al. (2011); Tsigaridis et al. (2013); Spada et al. (2013)).
Sea-salt emissions in the open ocean are relatively independent of model resolution compared to mineral dust emitted from arid regions (Ridley et al., 2013). However, some UNI-MIAMI coastal stations are surrounded by pronounced orographic gradients and/or complex sea/land interfaces (complex coastal areas and small islands). Therefore, even if free from surf-zone production, these stations may not be representative of open-ocean conditions from a meteorological point of view, which may affect the interpretation of global model evaluations. In this sense, we investigated the role played by model resolution in capturing topography, mesoscale circulations, and precipitation at these coastal/orographic regions, and how these aspects affected the sea-salt annual trends at the measurement stations. We focused on two regions including four UNI-MIAMI stations: the New Zealand region – including Baring Head (41.28°S, 174.87°E), Chatam Island (34.92°S, 176.50°W) and Invercargill (46.43°S, 168.35°E) – and Marion Island (46.92°S, 37.75°E).

3.2.1 Experimental design

We compared global simulations at 1°x1.4° horizontal resolution and 24 vertical levels (GLOB) with high-resolution regional simulations at 0.1°x0.1° and 40 vertical levels. The global simulations and their evaluation were discussed in Spada et al. (2013). In this contribution, we considered two high-resolution regional domains (REG) centered in New Zealand (174.8°E, 41.2°S) and Marion Island (37.7°E, 46.1°S). For the global simulations we applied the source function of Gong (2003) (G03-GLOB) based on a power law dependence on wind speed and the source function of Jaeglé et al. (2011) (J11-GLOB) based on Gong (2003) with an added dependency on SST. For the regional simulations we used the source function of Jaeglé et al. (2011) (J11-REG). The dynamical core and all physical schemes were identical in both REG and GLOB simulations. The two REG domains were extended enough (i.e. more than $2000km$ from the center of the domains, which represents five times the mean transport path of sea-salt aerosols at maximum wind speed conditions in the region) to avoid any noticeable sea-salt contribution from the boundaries of the domain to the study region. We performed 5-year simulations (2002-2006) in order to compare the model results with climatological observations. Simulations were initialized every 24h and constrained at boundaries every 6h with NCEP Final Analysis (FNL).

3.2.2 Observational data

For the model evaluation we considered four stations from the UNI-MIAMI Network: (a) Baring Head, (b) Chatam Island, (c) Invercargill, and (d) Marion Island (see Table 6). Measurements are available from the early 1980s to the 1996 and these sites are free from

Table 6: Observation sites considered in this Section. Labels UNI-MIAMI, NIWA, and SWAS stand for University of Miami Network, National Institute of Water and Atmospheric Research, and South African Weather Service, respectively. $*$ stands for average on multiple observation sites at the corresponding model gridcell.

station	latitude	longitude	contributor	observation years
sea-salt surface mass concentration				
Baring Head	41.28°S	174.87°E	UNI-MIAMI	1987 – 1996
Chatam Island	43.92°S	176.50°W	UNI-MIAMI	1983 – 1996
Invercargill	46.43°S	168.35°E	UNI-MIAMI	1983 – 1996
Marion Island	46.92°S	37.75°E	UNI-MIAMI	1992 – 1996
precipitation and wind				
Baring Head	41.28°S*	174.87°E*	NIWA	1980 – 2010
Chatam Island	43.92°S*	176.50°W*	NIWA	1980 – 2010
Invercargill	46.43°S*	168.35°E*	NIWA	1980 – 2010
Marion Island	46.90°S	37.85°E	SWAS	1980 – 2010

surf-zone produced sea-salt aerosol (J. Prospero, personal communication, 2012). Observed sea-salt concentration was computed as $sea - salt = Cl^- + 1.47Na^+$ (Quinn and Bates, 2005). Measurements are not constrained by an upper cutoff in radius. We also evaluated the simulated wind speed and precipitation with 30-year observational climatologies (1980-2010) provided by NIWA (Wratt et al., 2006) and SWAS (Rouault et al., 2005) (Table 6). Additionally, NIWA provided climatological maps covering the New Zealand islands at 0.5°x0.5° resolution.

3.2.3 Results and discussion

The New Zealand region is characterized by open ocean westerlies and extratropical cyclones colliding with steep orographic gradients, which represent a classic example of the barrier problem (e.g. Roe (2005)). The influence of the Southern Alps orographic gradients upon wind and precipitation patterns represents a well studied topic both experimentally (Sinclair et al., 1997; McCauley and Sturman, 1999; Wratt et al., 2000) and through regional modeling (Katzfey, 1995a,b; Bormann and Marks, 1999; Revell et al., 2002). Westerlies have to circumvent the barrier and the flux is enhanced at the edges of the Island; rising humid air cools by adiabatic expansion releasing precipitation at the windward side of the mountain and becomes drier at the leeward side.
The Southern Alps are around $40km$ wide and over $1.5km$ high, with maximum heights of $3km$. Therefore, at REG scales (λ_{REG}) the model was able to capture the spatial length characterizing the orographic gradients $\lambda_c = 40km$ ($\lambda_c \sim 5\lambda_{REG}$) in contrast to GLOB ($\lambda_c/\lambda_{GLOB} < 1$). Figure 14 shows the simulated annual sea-salt emission fluxes and annual mean surface concentration over the domain, both at low and high-resolution. At high-resolution (REG), the annual mean surface concentration decreased over New Zealand from 20% to 80% compared to the GLOB simulation. Marked changes in concentration patterns

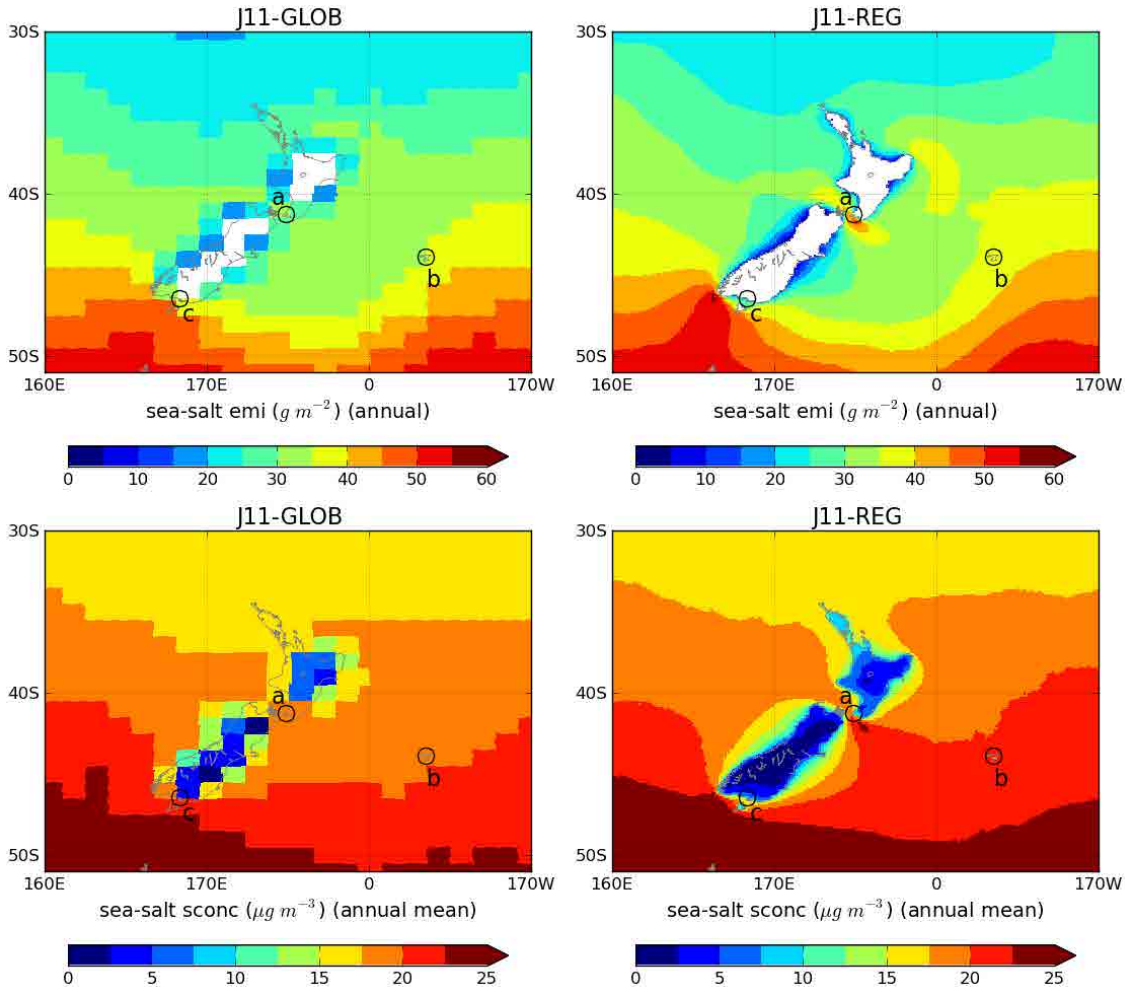

Figure 14: Simulated sea-salt annual emission (upper panels) and annual mean surface concentration (bottom panels) at low (GLOB, left column) and high (REG, right column) model resolutions over New Zealand using the Jaeglé et al. (2011) (J11) source function. Simulated averages refer to a 5-year period (2002-2006). The labels emi and sconc refer to emission flux and surface concentration, respectively. Plots are displayed over zoomed regions with respect to simulated domains (covering latitudes from 148.8°E to 159.2°W and longitudes from 15.2°S to 67.2°S). a, b, and c indicate UNI-MIAMI stations (Baring Head, Chatam Island, and Invercargill, respectively).

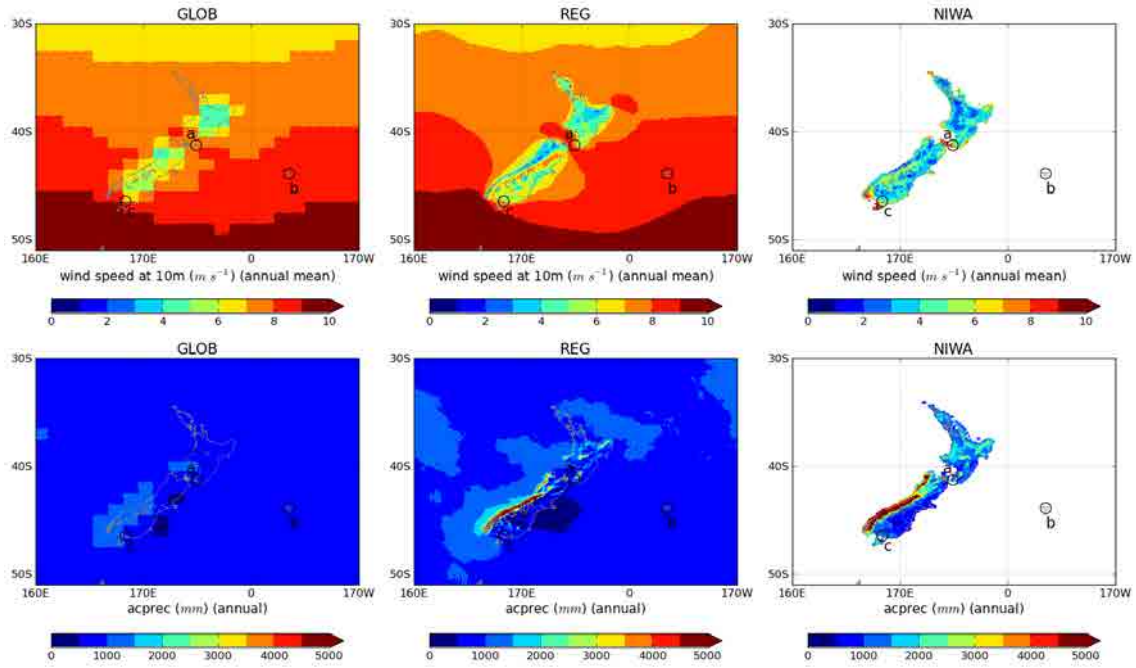

Figure 15: Simulated annual mean wind speed at 10m (upper panels) and annual accumulated precipitation (lower panels) at low (GLOB, left column) and high (REG, central column) model resolutions over New Zealand. 30-year observational climatologies from the National Institute of Water and Atmospheric Research (NIWA) are shown (right column). Simulated values cover a 5-year period (2002-2006). The label acprec refers to accumulated precipitation. Plots are displayed over zoomed regions with respect to simulated domains (covering latitudes from 148.8°E to 159.2°W and longitudes from 15.2°S to 67.2°S). a, b, and c indicate UNI-MIAMI stations (Baring Head, Chatam Island, and Invercargill, respectively).

also were found in the New Zealand straits that neighbor Baring Head (a) and Invercargill (c), respectively. Furthermore, Chatam Island (b) was treated as a land grid cell with no direct emission in the REG simulation, while it was represented as an ocean grid cell in the GLOB simulation, leading to a decrease of roughly 30%.

Figure 15 shows the simulated annual mean wind speed at 10m and annual precipitation over the New Zeland domain compared to the NIWA climatological maps. Simulated and observed wind roses at Invercargill are also displayed in Figure 16. Meteorological patterns changed significantly. At REG scales wind speed increased up to 20% compared to GLOB at the Cook Strait (between North and South Islands) and the edges of the Island. Over land, wind speed generally decreased, except for a narrow region leeward of the Southern Alps where winds increased up to $6 - 8m/s$, in better agreement with the observed NIWA climatology. Precipitation was enhanced to the west of the Island, including the open ocean and specially windward of the Southern Alps with a 800% increase. The maximum values and fine structure of precipitation were in strong agreement with the NIWA climatological map. Simulated precipitations upwind of the Southern Alps increased from $1200mm/yr$ with GLOB to $10300mm/yr$ with REG, removing most of the bias with respect to the NIWA maximum values (around $11200mm/yr$). The fine structure of the North Island and its local maxima were also well reproduced. The results outline the high-resolution model's ability to capture characteristic scales of the New Zealand circulation.

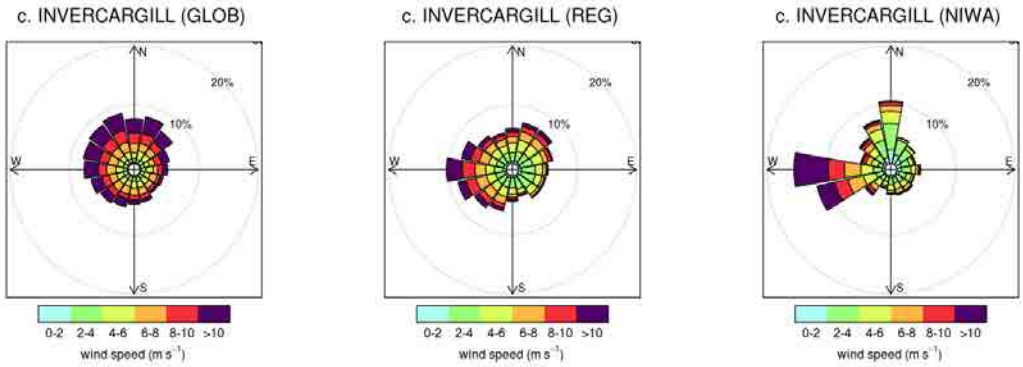

Figure 16: Simulated wind rose of Invercargill (c) at low (GLOB, left panel) and high (REG, central panel) model resolutions over New Zealand. 30-year observational climatologies from the National Institute of Water and Atmospheric Research (NIWA) are shown (right panel). Simulated values cover a 5-year period (2002-2006).

We also explored simulations over a large domain including Marion Island. Maps of sea-salt emission and surface concentration, wind speed at 10m, and precipitation are displayed in Figures 17 and 18. Marion Island (d) is a small volcanic island with steep orography (around $20km$ of diameter and up to $1200m$ altitude), subjected to strong northwesterly winds and high precipitation all year round. Regardless of the source function and global model, studies have shown systematic overestimations of the sea-salt surface concentration measured by the UNI-MIAMI station in this location. At the resolutions used by global models, the Island is considered as an open-ocean grid cell, and when REG scales were adopted, the sea/land interface was properly resolved by the model. In addition, precipitation was enhanced (up to 200% with respect to GLOB) windward of the orographic barrier. Consequently, an overall decrease of monthly mean concentrations from roughly $20\mu g/m^3$ (J11-GLOB) to $10\mu g/m^3$ (J11-REG) takes place over the Island.

Figures 19 and 20 show the evaluation at the UNI-MIAMI measurement sites. The scatter-plots indicate the significant improvement introduced when using high resolution. The strong positive bias affecting GLOB was reduced from +63% (J11-GLOB) to +3.3% (J11-REG) and the overall correlation increased from 0.52 to 0.84. The positive impact of model resolution was at least as large as the introduction of the SST-dependence in the G03 source function (bias reduced from +124% (GO3-GLOB) to +63% (J11-GLOB) and correlation increased from 0.36 to 0.52), which makes evident that these effects may be taken into consideration when evaluating source functions at these sites. The positive bias of wind speed at 10m was reduced from +24.6% to +15.8% and the correlation increased from 0.62 to 0.89. Remarkably, the high-resolution model was able to significantly reduce the overestimations of the wind speed monthly averages below $6m/s$. The simulation of precipitation improved with a reduction of the negative bias from -31.4% to -7.1%. In particular, the underestimated high monthly mean precipitations were corrected towards the observed values. The precipitation correlation increased from 0.65 to 0.86.

We identified three different effects introduced by the enhanced model resolution. (1) When the model was able to properly solve small islands and represented them as land grid cells instead of ocean cells, sea-salt aerosol was not directly produced in such cells and the sea-salt surface concentration strongly decreased: this was mostly the case of Chatam Island (b). (2)

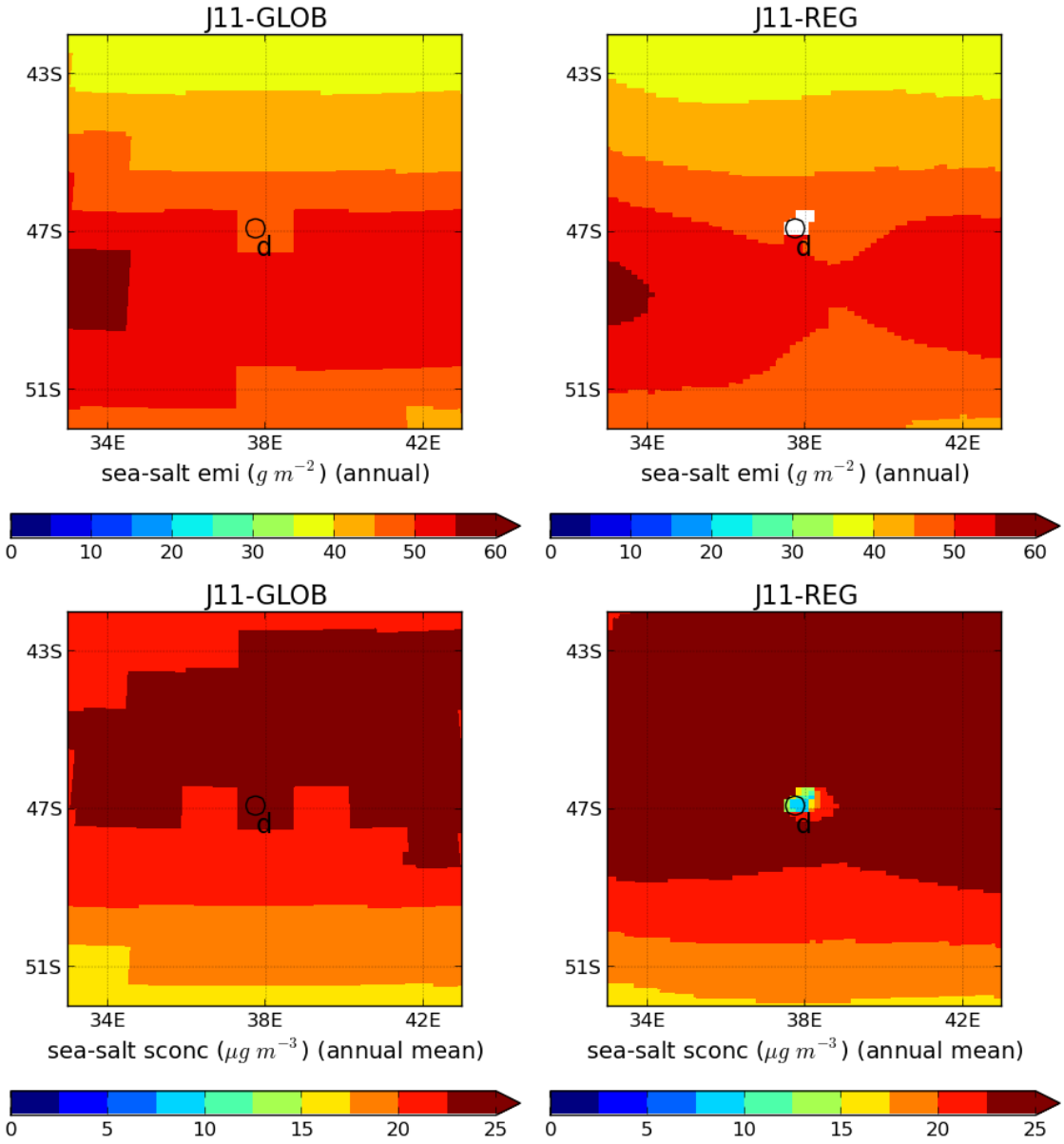

Figure 17: Simulated sea-salt annual emission (upper panels) and annual mean surface concentration (bottom panels) at low (GLOB, left column) and high (REG, right column) model resolutions over Marion Island using the Jaeglé et al. (2011) (J11) source function. Simulated averages refer to a 5-year period (2002-2006). The labels emi and sconc refer to emission flux and surface concentration, respectively. Plots are displayed over zoomed regions with respect to simulated domains (covering latitudes from 12.7°E to 62.7°E and longitudes from 21.9°S to 71.9°S). d indicates the UNI-MIAMI Marion Island station.

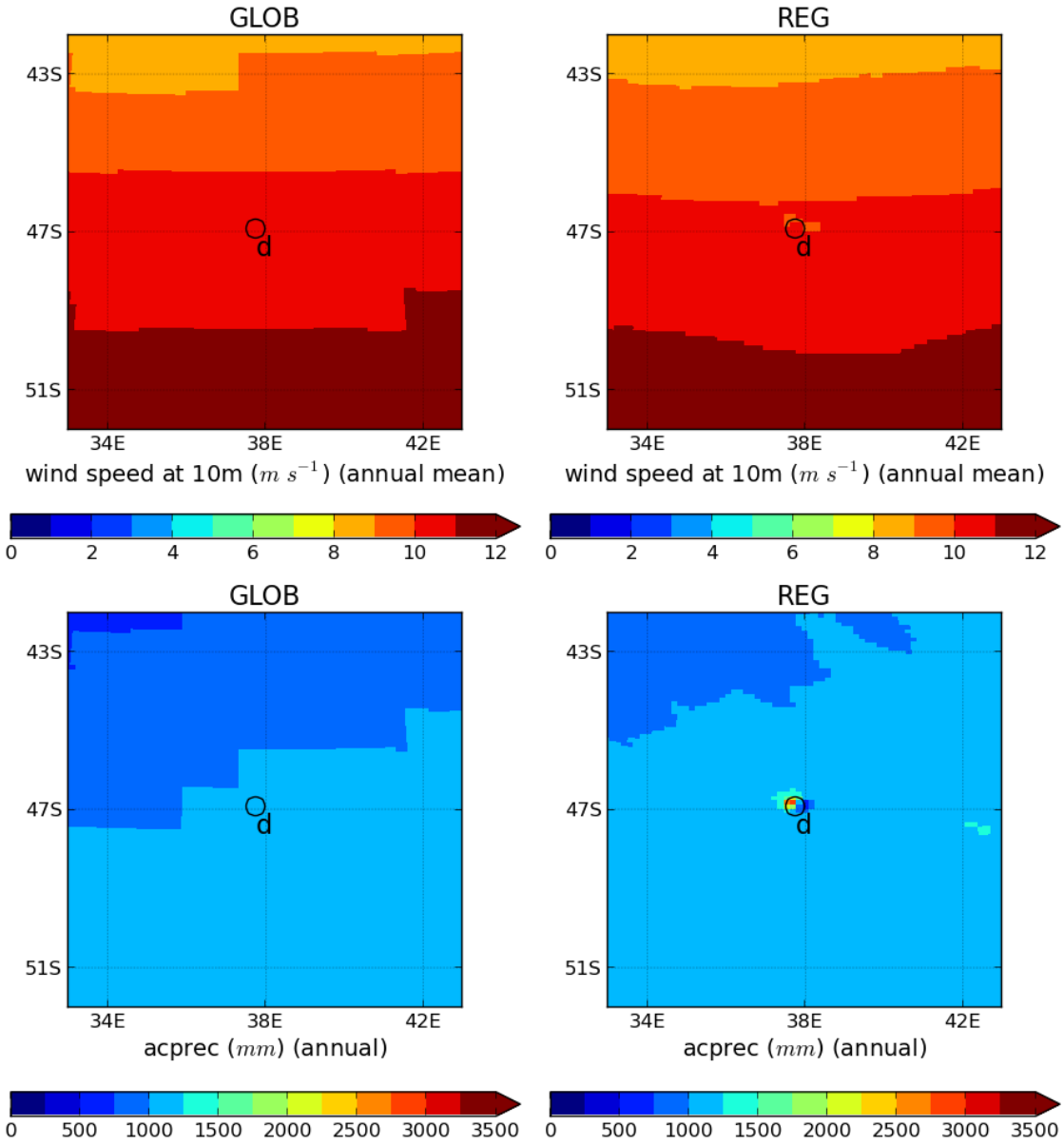

Figure 18: Simulated annual mean wind speed at 10m (upper panels) and annual accumulated precipitation (bottom panels) at low (GLOB, left column) and high (REG, right column) model resolutions over Marion Island. Simulated values cover a 5-year period (2002-2006). The label acprec refers to accumulated precipitation. Plots are displayed over zoomed regions with respect to simulated domains (covering latitudes from 12.7°E to 62.7°E and longitudes from 21.9°S to 71.9°S). d indicates the UNI-MIAMI Marion Island station.

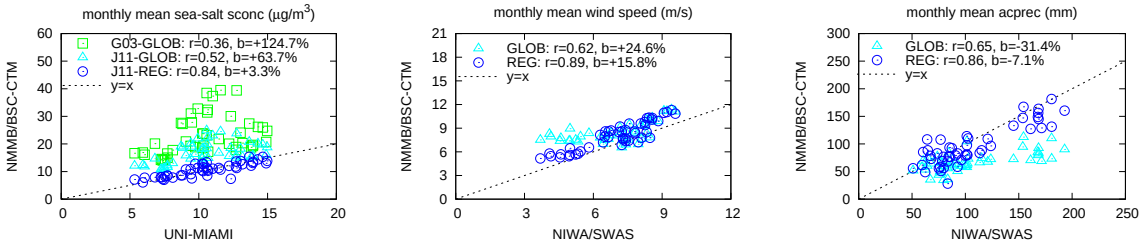

Figure 19: From left to right: scatterplots of simulated versus observed monthly mean sea-salt surface concentrations (sconc), wind speed at 10m, and precipitation (acprec); green squares, cyan triangles and blue circles refer to G03-GLOB (emission source of Gong (2003) at low resolution), J11-GLOB (emission source of Jaeglé et al. (2011) at low resolution), and J11-REG (emission source of Jaeglé et al. (2011) at high resolution) results, respectively. r and b stand for overall correlation and normalized bias. Simulated values cover a 5-year period (2002-2006).

At Invercargill (c), the simulated wind circulation was strongly affected by the representation of the Southern Alps barrier. The model scales were able to capture the mesoscale circulation, with wind speed reductions and changes in wind direction in better agreement with the measured climatologies. Figure 16 shows how the unrealistic wind rose at Inverncargill (c) with the GLOB simulations was clearly improved in the REG simulation, which better matched the observed dominant western winds and the lower wind speed values observed in other directions. Emissions and transport were consequently affected and the simulated surface concentrations decreased towards the observed monthly averages. We highlight the significant improvements introduced in the annual trend at Invercargill (c). The spurious maximum value in September obtained with GLOB simulations (also found in Liu et al. (2005) and Jaeglé et al. (2011)) was suppressed and replaced by a minimum value in August, in better agreement with the measured climatology. (3) At Baring Head (a) and Marion Island (d) we observed a significant increase in simulated precipitation when high-resolution was used, in agreement with measurements, with subsequent enhancement of sea-salt wet-deposition (not shown) and a decrease in concentration. Being Baring Head (a), Invercargill (c) and Marion Island (d) stations located close to the coastal line, model results in these sites were also affected by the sea/land interface effect discussed for Chatam Island (b). The quantification of the relative importance of each of these effects is complex and beyond the scope of this contribution.

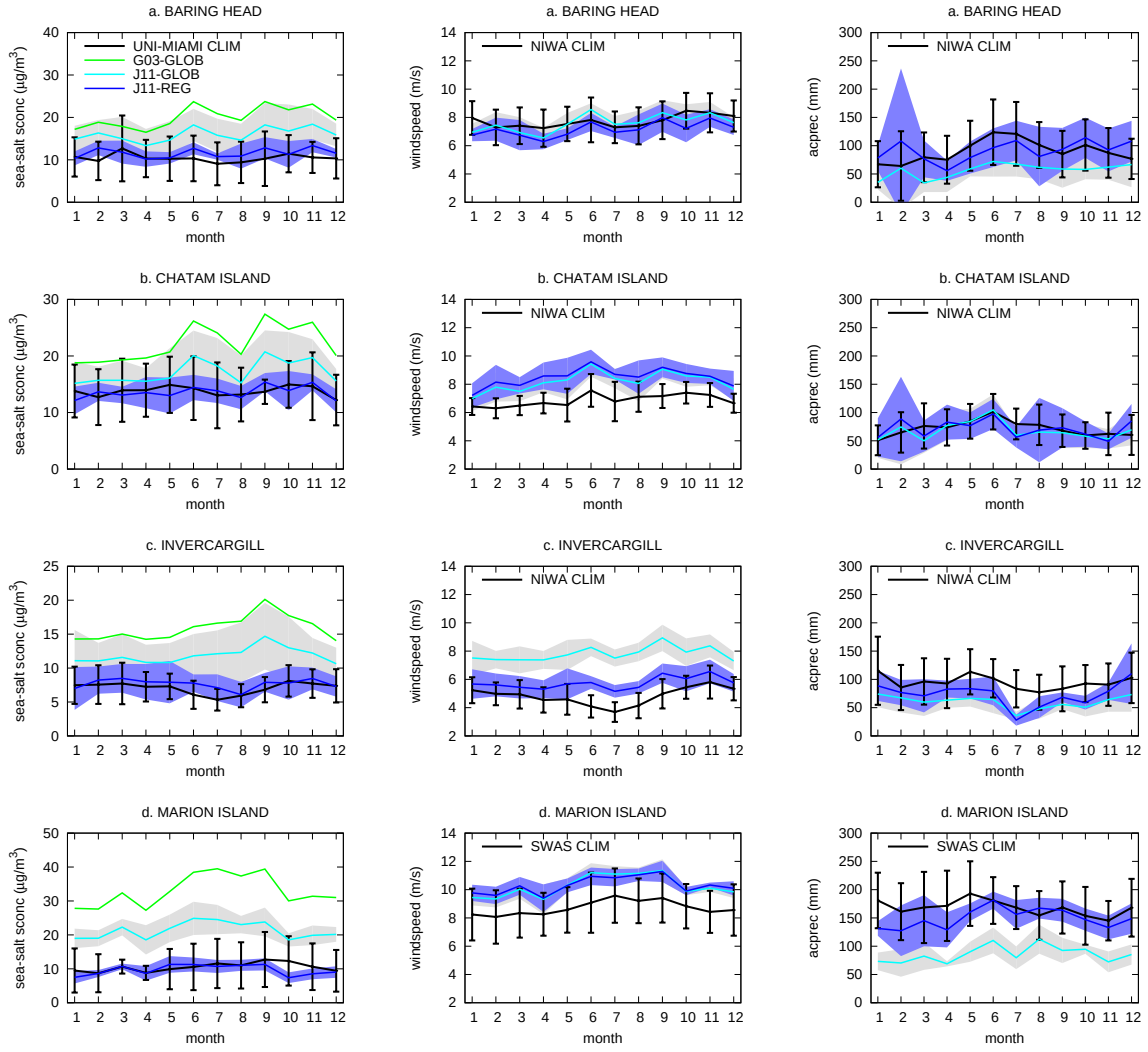

Figure 20: Simulated and observed monthly mean values of surface concentration (left column), wind speed at 10m (central column), and precipitation (right column) in each considered station; green, cyan, and blue lines refer to G03-GLOB, J11-GLOB, and J11-REG results, respectively. The label CLIM stands for climatologies. Observational climatologies (black lines, including standard error deviation bars) are from the University of Miami Network (UNI-MIAMI), the National Institute of Water and Atmospheric Research (NIWA), and the South African Weather Service (SWAS). Simulated values cover a 5-year period (2002-2006). J11-GLOB and J11-REG interannual standard deviation are also shown (shaded grey and blue, respectively).

Chapter 4 – Carbonaceous and sulfate aerosols

Based on:

Spada, M., Jorba, O., Pérez García-Pando, C., Tsigaridis, K., Soares, J., and Janjic, Z.: Global aerosols in the online multiscale NMMB/BSC Chemical Transport Model, in preparation for Geosci. Model Dev.

Aerosol particles over Mexico City. Photo credits: pnnl.gov

4 Carbonaceous and sulfate aerosols

The presence of organic aerosol, black carbon, and sulfate in the atmosphere can be strongly affected by the anthropogenic activity (including the burning of fossil fuels and biomass). In fact, organic aerosol and sulfate represent a very relevant (up to dominant) fraction of PM over anthropogenic regions (Jimenez et al., 2009). Carbonaceous and sulfate aerosols impact climate in at least three ways. sulfate scatters incoming solar radiation, thereby cooling the Earth's surface; carbonaceous aerosols (organic aerosol and black carbon) can scatter or absorb radiation and thus have the potential of warming or cooling the atmosphere. Both aerosol types may act as CCN, thus perturbing cloud cover and cloud properties (indirect effect). Also both may influence tropospheric chemistry, as they act as sites for heterogeneous chemical reactions. Thus these anthropogenic aerosols may influence climate directly by scattering and absorbing radiation and indirectly by acting as CCN and affecting atmospheric chemistry (Koch, 2001).

In a recent AEROCOM experiment, Tsigaridis et al. (2014) observed that the simulation of organic aerosol varies greatly between global models in terms of magnitude of primary emissions, SOA formation, number of organic aerosol species used (from 2 up to 60 or more), complexity of organic aerosol parameterizations (gas-particle partitioning, chemical aging, multiphase chemistry, aerosol microphysics), and organic aerosol physical, chemical and optical properties. The diversity of the global organic aerosol simulation results has increased during the last years, mainly due to the increasing complexity of the SOA parameterization in models, and the implementation of new and highly uncertain organic aerosol sources. Tsigaridis et al. (2014) concluded that there is no clear change in global models' skill with increasing model complexity with regard to organic carbon or organic aerosol mass concentration, even if complexity is needed in models in order to distinguish between anthropogenic and natural organic aerosol.

The ACCMIP intercomparison study of Lee et al. (2013) found that, despite the use the same black carbon emissions, the global black carbon burden differs by approximately a factor of 3 among models due to differences in aerosol removal parameterizations and simulated meteorology.

The simulation of sulfate aerosols is also still uncertain (Goto et al., 2011). The large differences shown by models can be associated with the simplifications of the sulfur processes. In particular, the diversity of sulfate sources is mainly caused by the disagreement on depositional loss of precursor gases and on chemical production (Textor et al., 2006).

In this Chapter we describe the implementation of organic aerosol, black carbon, and sulfate into the module. This represented the second fundamental step of our developments. An evaluation of the simulated aerosol global distribution is also presented. Note that the inclusion of carbonaceous and sulfate aerosols into the module, in addition to dust and sea-salt, also allowed the simulation and the evaluation of the total AOD, as presented in Section 4.2.

As already reported in Section 1.2, the modeling of ammonium/nitrate aerosols and nitrogen chemistry is beyond the scope of this thesis.

4.1 Model description

While dust and sea-salt aerosols were described using a sectional approach, since they span a large range of sizes (including coarse aerosols) and they are emitted by applying size-dependent

physical parameterizations, organic aerosol, black carbon, and sulfate aerosols were treated as bulk tracers, since they are difficult to be distributed in size at emission (Dentener et al., 2006). The characteristics of the aerosol species implemented in the module have been already reported in Table 2. A description of water-uptake, removal, and mixing processes has been presented in Chapter 2. In the following, we detail the specific assumptions done for the parameterization of carbonaceous and sulfate particles and the simulation of their life-cycle.

4.1.1 Organic Aerosol

We implemented two hydrophobic/hydrophilic bins to describe primary organic aerosols, and four hydrophilic bins to describe secondary organic aerosols. The six organic aerosol bins are represented with lognormal modes characterized by a geometric radius $r_g = 0.0212\mu m$ and a geometric standard deviation $\sigma = 2.24$, according to the Global Aerosol Data Set (GADS) of Köepke et al. (1997). The lognormal distributions provided by GADS are defined in the range from $0.005\mu m$ to $20\mu m$. A phobic-to-philic conversion mechanism was added to the organic aerosol transport equations to parameterize the particles' ageing in the atmosphere:

$$q_{\text{phob}}(t, \vec{x}) = -\frac{1}{\tau_{\text{ef}}} q_{\text{phil}}(t, \vec{x}) \tag{20}$$

$$q_{\text{phil}}(t, \vec{x}) = +\frac{1}{\tau_{\text{ef}}} q_{\text{phob}}(t, \vec{x}) \tag{21}$$

where q stands for the organic aerosol aerosol mass mixing-ratio at a given time (t) and grid-cell ($\vec{x}$). We set the e-folding time to $\tau_{\text{ef}} = 1.2$ days as in Chin et al. (2002).
The biogenic SOA aerosol production was implemented by using the 2-product scheme of Tsigaridis and Kanakidou (2007), detailed in Table 7. The formation of SOA from anthropogenic precursors is neglected in this work. In our implementation, the monoterpenes' (TERP) and isoprene (ISOP) concentrations are oxidated by OH and O_3 (R1–R4 of Table 7) to form four product gases. Then, a gas-particle partitioning is applied to produce the four SOA aerosols (R5–R8). Even if the reaction rates involved in the SOA scheme may also depend on the NO_x low/high concentration in the atmosphere, we assumed low NO_x conditions in this study. The SOA formation from anthropogenic precursor gases was neglected in this work. For the conversion of organic species (organic aerosol, POA, and SOA: units $\mu g/m^3$) to the correspondent organic carbon measurements (organic carbon, POC, and SOC: units $\mu g(C)/m^3$) we apply a factor OA/OC=1.8, which is an intermediate hypothesis between urban and non-urban values suggested by observations (Turpin and Lim, 2001; Aiken et al., 2008).

Table 7: SOA production mechanism. T stands for air temperature, C^* for saturation concentration, and $-\Delta H/R$ for enthalpy of vaporization.

gas-phase (mass-based stoichiometry)				
#	reaction	rate		reference
R1	TERP + OH → 0.192 TERP-P1 + other products	2.51E-11·EXP(444/T)		Tsigaridis and Kanakidou (2007)
R2	TERP + O_3 → 0.215 TERP-P2 + other products	1.4E-14·EXP(-732/T)		Tsigaridis and Kanakidou (2007)
R3	ISOP + OH → 0.0288 ISOP-P1 + other products	2.55E-11·EXP(410/T)		Tsigaridis and Kanakidou (2007)
R4	ISOP + O_3 → 0.232 ISOP-P2 + other products	1.23E-14·EXP(-2013/T)		Tsigaridis and Kanakidou (2007)
gas-aerosol partitioning				
#	reaction	C^* ($\mu g/m^3$)	$-\Delta H/R$ (K)	reference
R5	TERP-P1 ⇌ SOA1(a)	15.7	8.77E+3	Presto et al. (2005)
R6	TERP-P2 ⇌ SOA2(a)	385.0	8.77E+3	Presto et al. (2005)
R7	ISOP-P1 ⇌ SOA3(a)	1/1.62	5.05E+3	Henze and Seinfeld (2006)
R8	ISOP-P2 ⇌ SOA4(a)	1/0.00862	5.05E+3	Henze and Seinfeld (2006)

4.1.2 Black Carbon

Two modes were implemented for the black carbon aerosols (phobic/philic), which are assumed to be lognormally distributed with $r_g = 0.0118\mu m$ and $\sigma_g = 2.00$ (following GADS). The same phobic-to-philic conversion mechanism illustrated in the previous Section is applied to black carbon, with the same $\tau_{\text{ef}} = 1.2$days, as in Chin et al. (2002).

4.1.3 Sulfate

One hydrophilic mode was used to describe the sulfate aerosol, lognormally distributed according to GADS, with $r_g = 0.0695\mu m$, $\sigma_g = 2.03$ (see Table 2). A simplified approach to the sulfur chemistry was analyzed in this thesis, although the coupling with the full chemical mechanism of NMMB/BSC-CTM is already possible. As already stated, the implementation of ammonium/nitrate aerosols and their interactions with sulfate is beyond the scope of this thesis. As a consequence, the coupling of the nitrogen chemistry with the sulfur chemical mechanism is neglected in this work. The sulfate formation is parameterized within three production channels: the oxidation of SO_2 and DMS in their gas-phase, and the aqueous chemistry of SO_2. The chemical scheme presented in Table 8 includes gas-phase reactions (R_S1–R_S5), gas/aqueous equilibria (R_S6–R_S8), acid-base equibria (R_S9–R_S10), aqueous-phase reactions (R_S11–R_S13), and one photolysis reaction (R_S14). The reaction rates were taken from those indicated in the atmospheric chemistry box model CAABA/MECCA-3.0 (Sander et al., 2011), with the exception of the DMS chemistry that uses reactions and rates reported in Emmons et al. (2010). At the end of each chemistry timestep, we assumed that the sulfuric acid instantanously condenses into sulfate aerosol particles. The contribution from the aqueous chemistry is also added:

$$SU(a) = H_2SO_4(g) + SO_4^{2-}(aq) \tag{22}$$

where (a), (g), and (aq) stand for aerosol, gaseous, and aqueous phase, respectively. To solve the chemical reactions set S1–S13, we used the CAABA/MECCA-3.0 numerical methods by modifying the reaction rates according to our assumptions detailed in Table 8. Gaseous and aqueous reactions are treated as a coupled and closed system, avoiding errors due to quasi first-order approximations (Goto et al., 2011).
The aqueous chemistry uses the liquid water content (LWC) variable of the NMMB microphysics. At the end of the chemistry timestep, the aqueous concentrations of SO_2 and H_2O_2 are assumed to be fully evaporated and restored in their gas-phase concentrations.

4.1.4 Transport of gaseous species

Nine gaseous species are additionally transported by the model (see Table 9). The Henry's Law constants and enthalpies required by the gaseous wet deposition scheme are also listed. In our sulfur chemistry mechanism, SO_2, DMS, and H_2O_2 were simulated as prognostic species. We included for H_2O_2 as a prognostic tracer, since recent studies found that it could be a critical point for a proper simulation of the sulfur chemistry (Goto et al., 2011). The gases included in the SOA mechanism (i.e. TERP and ISOP and their 4 product gases) are also transported. The main uncertainty derives from the poor chemical characterization of the transport of product-gases (TERP-P1, TERP-P2, ISOP-P1, ISOP-P2). As reported in Table 9, we assumed formic acid-like values – the most simple carboxylic acid – for their Henry's Law constant and entalphy values and also for their dry deposition parameters.

Table 8: Sulfur chemistry mechanism. k_H, K_0, and $\tilde{K}_0$ stand for dissolution, dissociation, and aqueous reaction constants, respectively; $-\Delta$ H/R stands for enthalpy of vaporization. T(K) and C_{air}(mol/cm^3) refer to air temperature and concentration, respectively. Photolysis j-values are calculated with a specific module.

gas-phase				
#	reaction	rate		reference
R_S1	$HO_2+HO_2 \rightarrow H_2O_2+O_2$	k_{HO_2}(T, C_{air}, C_{H_2O})		Christensen et al. (2002)
R_S2	$H_2O_2+OH \rightarrow H_2O + HO_2$	1.8E-12		Kircher and Sander (1984)
R_S3	$SO_2+OH \rightarrow H_2SO_4+HO_2$ (*)	k_{3rd}(T, C_{air}, 3.3E-31, 4.3, 1.6E-12, 0., 0.6)		Sander et al. (2006)
R_S4	$DMS+OH \rightarrow SO_2$	k_{DMS1}(T)		Emmons et al. (2010)
R_S5	$DMS+OH \rightarrow 0.5SO_2 + 0.5HO_2$	k_{DMS2}(T, C_{air})		Emmons et al. (2010)
k_{HO_2}(T, C_{air}, C_{H_2O})=(1.5E-12·EXP(19/T)+1.7E-33·EXP(1000/T)· C_{air})·(1+1.4E-21·EXP(2200/T)· C_{H_2O})				
k_{3rd}(T, a, k_0, n, k_0^{inf}, m, f_c)=ak_0(300/T)^n /(1+ak_0(300/T)$^{n-m}$/k_0^{inf})/$f_c^{(1+(\log_{10}(ak_0(300/T)^{n-m}/k_0^{inf}))^2)}$				
k_{DMS1}(T)=9.6E-12·EXP(-234/T)				
k_{DMS2}(T, C_{air})=1.7E-42· EXP(7810/T)· 0.21 C_{air} /(1+5.5E-31· EXP(7460/T) · 0.21 C_{air})				
gas-phase/aqueous-phase equilibria				
#	reaction	k_H (M/atm)	$-\Delta$ H/R (K)	reference
R_S6	$O_3 \rightleftharpoons O_3$(aq)	1.2E-2	2.56E+3	Chameides (1984)
R_S7	$H_2O_2 \rightleftharpoons H_2O_2$(aq)	see Table 9	see Table 9	
R_S8	$SO_2 \rightleftharpoons SO_2$(aq)	see Table 9	see Table 9	
acid-base and other equilibria				
#	reaction	K_0 (M^{m-n})	$-\Delta$H/R (K)	reference
R_S9	SO_2(aq) $\rightleftharpoons H^+$(aq) + HSO_3^-(aq)	1.7E-2	2.09E+3	Chameides (1984)
R_S10	HSO_3^-(aq) $\rightleftharpoons H^+$(aq) + SO_3^{2-}(aq)	1.7E-2	1.12E+3	Chameides (1984)
aqueous-phase				
#	reaction	$\tilde{K}_0$ ($M^{1-n}s^{-1}$)	$-\Delta$H/R (K)	reference
R_S11	SO_3^{2-}(aq) + O_3(aq) $\rightarrow SO_4^{2-}$(aq) (*)	1.5E+9	-5.3E+3	Hoffmann (1986)
R_S12	HSO_3^-(aq) + O_3(aq) $\rightarrow SO_4^{2-}$(aq) + H^+(aq) (*)	3.7E+5	-5.5E+3	Hoffmann (1986)
R_S13	HSO_3^-(aq) + H_2O_2(aq) $\rightarrow SO_4^{2-}$(aq) + H^+(aq) (*)	5.2E+6	-3.65E+3	Martin and Damschen (1981)
photolysis				
#	reaction	rate		reference
R_S14	H_2O_2 + h$\nu \rightarrow$ 2 OH	jx(H_2O_2)		Sander et al. (2011)

(*) assumed to be converted in sulfate aerosol at the end of the chemical timestep: sulfate(a) = H_2SO_4(g) + SO_4^{2-}(aq) (where a, g, and aq stand for aerosol, gaseous, and aqueous phase, respectively)

Gaseous species are transported following the NMMB/BSC-CTM gas-phase module (Jorba et al., 2012). The Wesely (1989) scheme was used for the dry deposition. The cloud chemistry scheme of Byun and Ching (1999) and Foley et al. (2010) were applied in order to resolve the cloud processes affecting the concentration of air pollutants. The processes included are grid-scale scavenging and wet deposition, subgrid-scale vertical mixing, scavenging and wet-deposition for precipitating and non-precipitating clouds. Only incloud scavenging is considered for gases.

4.2 Evaluation of the NMMB/BSC-CTM aerosol module at global scale

We describe the global-scale evaluation conducted in this work. The emissions chosen for our experiment are reported in Section 4.2.1. The experimental design and the observational datasets used for the evaluation are detailed in Sections 4.2.2 and 4.2.3, respectively. Finally, model results and their comparison with observations are discussed in Section 4.2.4.

4.2.1 Anthropogenic and natural emissions

The emission inventories and schemes used in this work are detailed in Table 10. Anthropogenic emissions of POA, black carbon, and SO_2 are from the AEROCOM-ACCMIP inventory, downloaded from the AEROCOM web (`http://aerocom.met.no/download/emissions/AEROCOM-II-ACCMIP/`) and based on the work of Lamarque et al. (2010). For our experiments, we assumed these emissions to be constant during the year (as in their original formulation which is characterized by an annual temporal resolution). Their original horizontal resolution is 0.5°x0.5°; aircraft emissions are described within 25 vertical levels. Emission fluxes were

Table 9: Gas tracers and their chemical properties in the model. Off-line means climatological values from an off-line simulation using the full gas-phase chemical mechanism (Badia, 2014). k_H and $-\Delta$ H/R stand for Henry's Law constant and Entalphy (activation energy), respectively.

gas	transported/off-line	k_H (M/atm)	$-\Delta$ H/R (K)	reference
SO_2	transported	1.2	3.12E+3	Chameides (1984)
DMS	transported	5.4E-1	3.5E+3	Staudinger and Roberts (2001)
H_2O_2	transported	1.E+5	6.338E+3	Lind and Kok (1994)
TERP	transported	4.9E-2 (†)	0 (†)	Sander (1999) (†)
ISOP	transported	2.8E-2	0	Sander (1999)
TERP-P1	transported	8.9E+3 (*)	6.1E+3 (*)	Johnson et al. (1996) (*)
TERP-P2	transported	8.9E+3 (*)	6.1E+3 (*)	Johnson et al. (1996) (*)
ISOP-P1	transported	8.9E+3 (*)	6.1E+3 (*)	Johnson et al. (1996) (*)
ISOP-P2	transported	8.9E+3 (*)	6.1E+3 (*)	Johnson et al. (1996) (*)
OH	off-line ($\diamond$)	–	–	–
HO_2	off-line ($\diamond$)	–	–	–
O_3	off-line ($\diamond$)	–	–	–

(†) pinene values assumed
(*) formic acid values assumed
($\diamond$) assumed off-line in this work, but it can be transported by NMMB/BSC-CTM

conservatively interpolated onto the model grid (1°x1.4°, 24 vertical levels. AEROCOM-ACCMIP also provides monthly biomass-burning emissions of POA, black carbon, and SO_2. We introduced these emissions into the model by keeping their monthly resolution. SO2 emissions from volcanos were described by using the daily fluxes provided by the AEROCOM-HC inventory (`http://aerocom.met.no/download/emissions/AEROCOM_HC/`), based on the Global Volcanism Program's database provided by the Smithsonian Institution (where subglacial and submarine volcanoes are excluded). For our experiments, only non-eruptive emissions were selected. DMS production fluxes from oceans were introduced by using the emissions provided by MOZART-4 (`http://cdp.ucar.edu`), which refer to DMS simulations for the year 2000 achieved by the HAMOCC5 model (Kloster et al., 2006).

The MEGAN model (Guenther et al., 2006) was coupled with the model to produce online emission fluxes of monoterpenes (we assumed the 21 monoterpenes simulated by MEGAN as contributors of TERP emissions) and isoprene. Primary carbonaceuos emissons were distributed into phobic/philic bins by assuming a partitioning of 65%/35% for organic aerosol, following Mayol-Bracero et al. (2002), and 80%/20% for black carbon, according to Chin et al. (2002).

In Table 10 we also reported the vertical injection height we assumed for emissions. Emissions were distributed homogenously in the model vertical layers, proportionally to the fraction of the emission height covered by each layer depth. Volcanos emissions are homogenously injected in the top third of the plume. To inject emissions from forest and grassland fires, we used the satellite-derived climatological profiles calculated by the IS4FIRES (Sofiev et al., 2012) (available in the web at `http://is4fires.fmi.it/data/vertcal_profiles.htm`). The fraction of total emission flux is given for 20 vertical layers and on a monthly climatological scale, based on averages of satellite data over the years 2001–2008 (at a resolution of 1°x1°). The data were remapped onto the model grid. Since the estimated fluxes in the AEROCOM-ACCMIP inventory comes from top-down or bottom-up techniques, while the

IS4FIRES injection height fractions from satellite retrievals, it may happen that for a given model gridcell we have positive non-zero emission flux but null vertical fractions to inject the flux: in this case we set to zero the emissions. With this assumption we are probably missing fires at high latitudes, where satellite data are unavailable.

Table 10: Emissions used in this work. The assumed vertical injection height of emissions is also indicated. Temp. res. stands for temporal resolution.

source	species	temp. res.	temp. range	reference	vert. height (m)
			off-line		
traffic	POA, BC, SO_2	yearly	2002–2006	AEROCOM-ACCMIP	0–10
agric. waste	POA, BC, SO_2	yearly	2002–2006	AEROCOM-ACCMIP	0–100
domestic	POA, BC, SO_2	yearly	2002–2006	AEROCOM-ACCMIP	0–10
energy prod. plants	POA, BC, SO_2	yearly	2002–2006	AEROCOM-ACCMIP	100–300
industrial plants	POA, BC, SO_2	yearly	2002–2006	AEROCOM-ACCMIP	100–300
waste	POA, BC, SO_2	yearly	2002–2006	AEROCOM-ACCMIP	100–300
ships	POA, BC, SO_2	yearly	2002–2006	AEROCOM-ACCMIP	0–30
aircrafts	BC	yearly	2002–2006	AEROCOM-ACCMIP	25 levels interp. to model grid
grassland bb	POA, BC, SO_2	monthly	2002–2006	AEROCOM-ACCMIP	IS4FIRES clim.
forest bb	POA, BC, SO_2	monthly	2002–2006	AEROCOM-ACCMIP	IS4FIRES clim.
oceanic DMS	DMS	monthly	2000	MOZART	0–10
volcanos (non-erup.)	SO_2	daily	2002–2006	AEROCOM-HC	upper 1/3 of volc. plume
			on-line		
biogenic	TERP, ISOP	online	–	MEGAN	0–10
desert dust	dust	online	–	Pérez et al. (2011)	surface layer
sea-salt	sea-salt	online	–	Monahan et al. (1986)	0–10

4.2.2 Experimental design

We performed global simulations including the 25 aerosol tracers described in Table 2 and the 9 gas-phase tracers described in Table 9. A horizontal resolution of 1°x1.4° and 24 vertical layers were used. The dynamics timestep was $dt = 90s$. Physical parameterizations and chemical mechanisms were both solved every $4dt = 360s$. Since the small value of the physical timestep, governing the solution of cloud processes, the errors due to neglection of the transport of aqueous species were minimized. We simulated the period 2002–2006. Meteorological conditions were initialized every 24h using the NCEP final analyses (FNL) at 1°x1°. A spinup of 1 year was considered at the beginning of the simulated period. The model output was taken every 3h to calculate monthly mean values. For this benchmark study of the aerosol module, the chemical mechanism (both of sulfur species, see Table 8, and of SOA-related species, see Table 7) was assumed uncoupled with the chemistry of the involved oxidants (namely OH, O_3, and HO_2). Off-line oxidant fields were provided every 3h by monthly mean values obtained with the full gas-phase chemical mechanism for the year 2004 (Badia, 2014).

It has been found in Section 3.1 that the use of the SST-dependent scheme of Jaeglé et al. (2011) implies an improvement of model results, but also a marked overestimation of the tropical AOD coarse fraction during the summer. Then, for this experiment, the basic production scheme of Monahan et al. (1986) is used in order to minimize the uncertainties in the simulation of the total AOD.

The same calibration factor used in the global simulations of Pérez et al. (2011) is applied to calculate the dust emission flux.

The direct effect of aerosol on the radiative scheme was turned off in order to avoid additional sources of uncertainty.

4.2.3 Observational data

The simulated concentrations were compared with observations from ground-based networks: respectively, EMEP in Europe (Tørseth et al., 2012), IMPROVE in US (DeBell et al., 2006), and EANET in Asia. The data were downloaded from the EBAS webpage (`http://ebas.nilu.no`) managed by the Norwegian Institut for Air Research (NILU). For this comparison we selected exclusively observations which fall in the simulated 5-year period (2002–2006), obtaining monthly mean values for each specific year under study. A minimum of 2 weeks of measurements was required for the monthly mean calculations and a minimum of 3 years was required to perform interannual calculations. The data not satisfying this constraint were discarded. Only rural/remote sites of the EMEP and IMPROVE networks were considered. The considered mass concentrations measurements are from filterpacks and they are characterized by different particle size cutoffs at "dry" conditions (RH<50%). To be consistent with measurements, we calculated fractions of PM2.5 and PM10 mass concentrations of organic carbon, elemental carbon, and sulfate by applying the assumption of lognormal distribution $n(r, r_g, \sigma_g)$:

$$\mathrm{PM}_\eta/\mathrm{PM}_{\mathrm{tot}} = \Big(\int_{5E-3}^{0.5\eta} r^3 n(r, r_g, \sigma_g) dr\Big) \Big/ \Big(\int_{5E-3}^{2E+1} r^3 n(r, r_g, \sigma_g) dr\Big) \tag{23}$$

where η is the dry diameter cutoff (i.e. 10μm for PM10, 2.5μm for PM2.5) and r the particle dry radius. EMEP provides data for both PM2.5 and PM10 measurements, while IMPROVE only PM2.5 measurements of organic carbon, black carbon, and sulfate. Only PM10 sulfate observations are provided by EANET. Note that in this case we refer to elemental carbon (not black carbon) measurements, since they are filterpack measurements.
As a second evaluation, we compared the simulated monthly concentrations with worldwide observations from specific networks that are often used for model intercomparison studies; in this way we can get additional information about the model performance with respect to the other state-of-the-art models. We assumed that the following datasets refer to "dry" (RH<50%) measurements. Networks and measurement years are listed in Tables 11 and 12 and displayed in Figure 21 (top panel). For the evaluation of the organic carbon, we used stations from the observational dataset considered in Tsigaridis et al. (2014) (TS14). They are a merging of observations from different networks and different years; for example the US stations of Ohio (a), Colorado (b), Arizona (c), and Georgia (d) are from the IMPROVE network (averages over 2002–2006). The considered stations were categorized as remote or marine sites. Note that in 8 out of 9 sites the measured parameter is the organic carbon mass concentration, while in Welgegund (f) we have displayed measurements of organic aerosol, since we are referring to AMS optical measurement. We recall that we modeled the OA/OC ratio by applying a factor of 1.8. For black carbon, the observational dataset described by Lee et al. (2013) (LE13) is used. It includes remote sites and sites perturbed by the transport of anthropogenic aerosols. The LE13 dataset was obtained from measurements provided by the National Oceanic and Atmospheric Administration Earth System Research Laboratory Global Monitoring division (NOAA-ESRL-GMD), the Atmospheric Radiation Measurement Program of the U.S. Department of Energy (ARM/DOE), and EMEP. The data collected in Alert, Pallas (see Hyvärinen et al. (2011)), and Jungfraujoch were provided by S. Sharma (Environment Canada), H. Lihavainen (Finnish Meteorological Institute), and M. Collaud Coen (MeteoSwiss), respectively. Note that the notation black carbon is applied in this case because observations come from optical measurements performed with Aethalometers

and Particle Soot Absorption Photometers. The mass concentration measurements of the University of Miami Network (Savoie and Prospero, 1977) at 11 marine sites in the Northern Hemisphere and 12 marine sites in the Southern Hemisphere are considered to evaluate the model performance in the simulation of sulfate. Note that no upper cutoff has to be imposed to these high-volume filter sampler measurements.
Additionally, we performed an evaluation of the simulated AOD, where dust and sea-salt are also contributing in addition to organic carbon, black carbon, and sulfate. A first model AOD evaluation was performed by comparing with AERONET observations at 152 worlwide sites. The monthly averages were calculated from the monthly averages provided by the AERONET level 2.0 climatological tables `http://aeronet.gsfc.nasa.gov/cgi-bin/climo_menu_v2_new` (which are calculated from daily averages) if a minimum of 3 years of data was available in the years 2002–2006. The considered AERONET stations are plotted in Fig. 21 (bottom panel). Four regions of specific interest are introduced to characterize the stations: the North American (NA), the European (EU), the Eastern Asia (EA), and the African domains. A second comparison with satellite data was provided. For MODIS, we considered the monthly mean AOD at 550nm provided by the Aqua Black Target - Deep Blue Collection 6 merged product (Sayer et al., 2014), which is available from July 2002 to December 2006 and which partially covers the simulated period. The MISR Level 3 monthly mean AOD (green band) (Kahn et al., 2005) is also considered for the comparison, covering the whole 2002–2006 period. MODIS and MISR data are obtained from the Giovanni Online Visualization and Analysis System website `http://disc.sci.gsfc.nasa.gov/giovanni`. MODIS data were downloaded at a horizontal resolution of 1°x1°, while MISR at 0.5°x0.5°; then, they were interpolated onto the model grid.

Note that the observational data were obtained from pre-calculated monthly AERONET and satellite products, while the model monthly mean values were calculated by averaging over a 3-hourly output. Hence, inconsistencies may affect the comparison, due to the fact that the model output was not temporally and spatially collocated with observations.

To compare with both AERONET and satellite measurements, we calculated a diagnostic clear-sky value. This issue still remains very open and uncertain within the the aerosol community (Shindell et al., 2013), so even a naive estimate as the flip-coin algorithm we describe in the following can be useful to the discussion. For each model vertical layer in each gridcell at a given timestep, we considered the cloud cover (CC) calculation done by the NMMB, which accounts for both convective and grid-scale clouds. By roughly assuming that the horizontal distribution of clouds in a vertical layer k is independent from that calculated for other layers and we estimated the probability of a sun beam to pass through the entire column to be:

$$P_{\text{cs}} = \prod_{k=1}^{K} [1 - CC(k)] \tag{24}$$

where $K = 24$ is the number of vertical levels in our simulations. At this point we rolled a random from 0 to 1 (ξ): if the result was lesser than P_{cs}, then we assumed that we have clear-sky conditions in the model gridcell; if not, the clear-sky AOD was considered as a missing value:

$$\text{clear-sky AOD} = \begin{cases} \text{AOD}, & \text{if } \xi < P_{\text{cs}} \\ \text{missing}, & \text{otherwise} \end{cases} \tag{25}$$

Obviously, this algorithm was designed to provide a probabilistic calculation of monthly and annual mean values, not reliable instantaneuos estimates.

To compare our results with other models, the following works have been taken as main references: the AEROCOM organic aerosol evaluation study of Tsigaridis et al. (2014) (TS14), the AEROCOM Phase-II experiment (AC-II) (specifically the CTRL simulations of the year 2006 as reported in the AEROCOM web: `http://aerocom.met.no/cgi-bin/AEROCOM/aerocom/surfobs_annualrs.pl`, last check: 18/05/2015), the AEROCOM Experiment-B (ACB) simulating the year 2000 as described in Textor et al. (2006), the ACCMIP black carbon intercomparison study of Lee et al. (2013) (LE13), and the ACCMIP radiative forcing experiment (SH13) of Shindell et al. (2013) (we refer to the year 2000).

Table 11: List of observational sites used for the comparison with model results (part 1 of 2). lon, lat, and alt stand for longitude, latitude, and altitude of observations, respectively. Parameter specifies the measured variables; the label years indicates the interval of time in which measurements are available and/or considered.

surface concentration							
num. stations	*network/campaign*		*region*		*parameter*	*years*	*category*
143	IMPROVE (PM2.5)		US		OC, EC, SU	2002–2006	rural/remote
7	EMEP (PM2.5)		EU		OC, EC	2002–2006	rural/remote
10	EMEP (PM2.5)		EU		SU	2002–2006	rural/remote
18	EMEP (PM10)		EU		OC, EC	2002–2006	rural/remote
20	EMEP (PM10)		EU		SU	2002–2006	rural/remote
29	EANET (PM10)		EA		SU	2002–2006	rural/remote/urban
specific site	*network/campaign*	*lon*	*lat*	*alt(m)*	*parameter*	*years*	*category*
a) Ohio	TS14	81.34W	39.94N	366	OC	2002–2006	remote
b) Colorado	TS14	107.80W	37.66N	2750	OC	2002–2006	remote
c) Arizona	TS14	114.07W	36.02W	902	OC	2002–2006	remote
d) Georgia	TS14	82.13W	30.74N	48	OC	2002–2006	remote
e) Finokalia	TS14	25.67E	35.33N	250	OC	2004–2007	remote
f) Welgegund	TS14	26.94E	26.57S	1480	OA	2010–2011	remote
g) Alaska	TS14	148.97W	63.72N	658	OC	2002–2006	remote
h) Manaus	TS14	60.21W	2.59S	45	OC	2008–2010	remote
i) Amsterdam I.	TS14	77.52E	37.78S	70	OC	2003–2007	marine
A) Alert	LE13	62.5W	82.4N	200	BC	1989–2006	arctic
B) Ny Alesund	LE13	11.9E	78.9N	474	BC	2005–2010	arctic
C) Barrow	LE13	156.6W	71.3N	11	BC	1998–2011	arctic
D) Pallas	LE13	23.7E	68.0N	340	BC	2005–2010	sub-arctic
E) Hyytiala	LE13	24.3E	61.8N	181	BC	2004–2011	remote
F) Preila	LE13	21.1E	55.3N	5	BC	2008–2010	marine
G) Mace Head	LE13	9.5W	53.2N	15	BC	2003–2007	remote
H) Ispra	LE13	8.6E	45.8N	209	BC	2007–2010	perturbed continental
I) Sable I.	LE13	60.0W	43.9N	5	BC	1996–2000	perturbed marine
L) Trinidad H.	LE13	124.2W	41.0N	107	BC	2002–2011	marine
M) S. G. Plains	LE13	97.5W	36.6N	314	BC	1996–2011	perturbed continental
N) Bondville	LE13	88.4W	40.0N	230	BC	1996–2011	perturbed continental
O) Mauna Loa	LE13	155.6W	19.5N	3397	BC	2001–2011	marine
P) Jungfraujoch	LE13	8.0E	46.5N	3578	BC	1995–2011	remote

4.2.4 Results and discussion

Detailed evaluations of the dust and sea-salt modules were already discussed Pérez et al. (2011) and Spada et al. (2013) (see Section 3.1). In this Section we focus on the evaluation of organic aerosol, black carbon, and sulfate concentrations. Additionally, we also present an evaluation of the simulated monthly mean total AOD. We remind that, where not differently specified, model values and observations are averaged over the period 2002–2006: consequently, with the terms annual and monthly means we intend interannual (2002–2006) averages of the annual and monthly mean values, respectively.

Organic aerosol. Fig. 22 (top-left panel) displays the global distribution of simulated organic aerosol annual mean surface concentration and, additionally, the contribution of SOA (top-right panel). The simulated organic aerosol annual mean concentrations range from few nanograms per cubic meter up to maximum values of $10\mu g/m^3$ or more found in the East and South-East Asia. Other relative maxima around $5\mu g/m^3$ or more are found in the Central

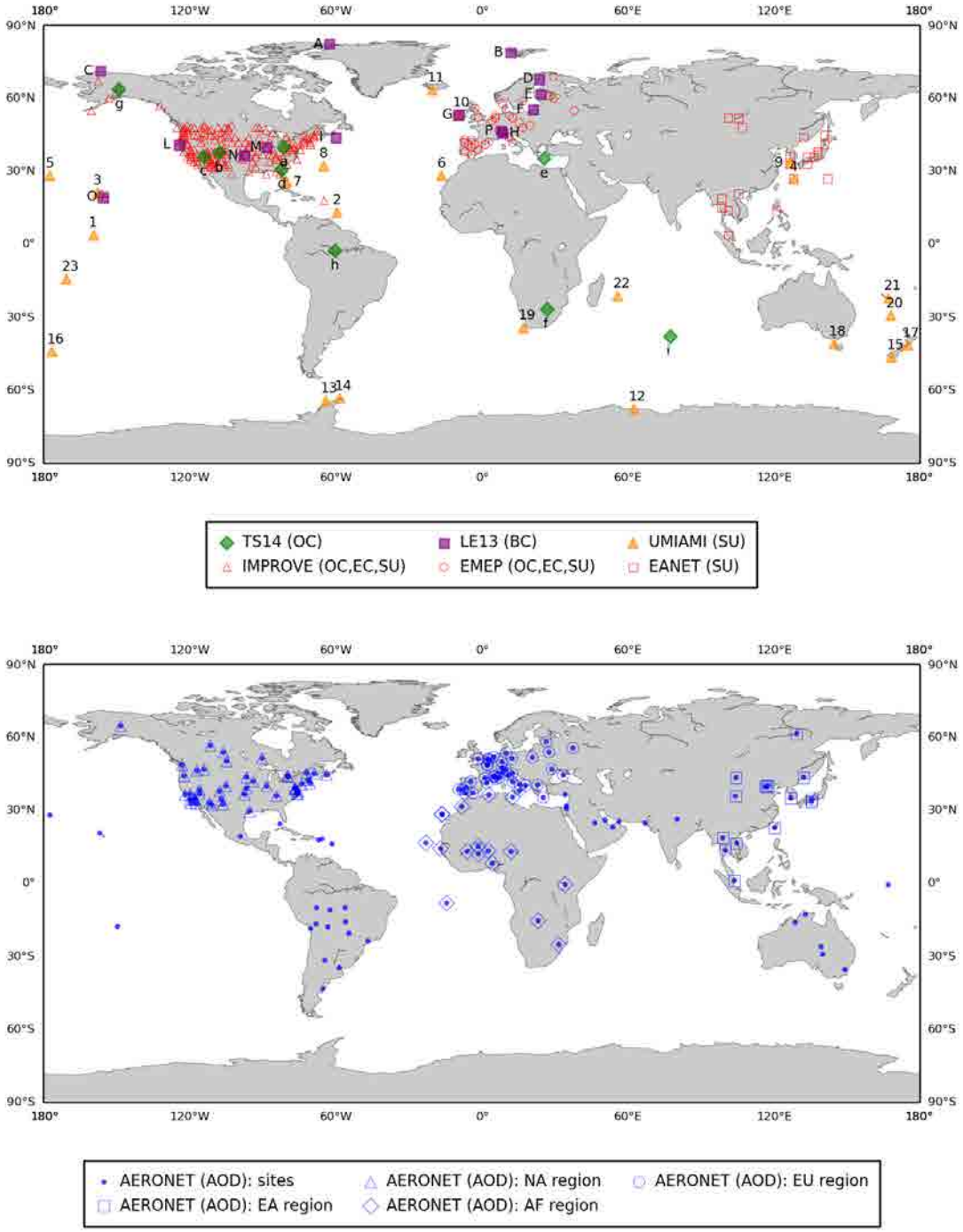

Figure 21: Top panel: observational networks used for the comparison with simulated surface concentrations (sites are also listed in Tables 11 and 12). Green filled diamonds and purple filled squares indicate specific observational sites used by TS14 and LE13, respectively. Orange filled triangles indicate measurements from the UMIAMI network. Red triangles, circles, and squares indicate IMPROVE, EMEP, and EANET observational sites (in the period 2002-2006). Bottom panel: observational network used for the comparison with simulated AOD at 500nm (sites are also listed in Table 12). Blue filled circles indicate AOD measurement sites from the AERONET sunphotometer network. Triangles, circles, squares, and diamonds indicate specific sub-domains, i.e. North America, Europe, East Asia, and African region, respectively.

Table 12: List of observational sites used for the comparison with model results (part 2 of 2). lon, lat, and alt stand for longitude, latitude, and altitude of observations, respectively. Parameter specifies the measured variables; the label years indicates the interval of time in which measurements are available and/or considered.

surface concentration							
specific site	*network/campaign*	*lon*	*lat*	*alt(m)*	*parameter*	*years*	*category*
1) Fanning I.	UMIAMI	159.33W	3.92N	-	SU	1981-1986	marine
2) Barbados	UMIAMI	59.43W	13.17N	-	SU	1984-1998	marine
3) Oahu	UMIAMI	157.70W	21.33N	-	SU	1981-1995	marine
4) Hedo Okinawa	UMIAMI	128.25E	26.92N	-	SU	1991-1994	marine
5) Midway I.	UMIAMI	177.35W	28.22N	-	SU	1981-1997	marine
6) Izana	UMIAMI	16.50W	28.30N	2360	SU	1987-1998	marine
7) Miami	UMIAMI	80.25W	25.75N	-	SU	1989-1998	marine
8) Bermuda	UMIAMI	64.87W	32.27N	-	SU	1989-1998	marine
9) Cheju Korea	UMIAMI	126.48E	33.52N	-	SU	1991-1995	marine
10) Mace Head	UMIAMI	9.85W	53.32N	-	SU	1988-1994	marine
11) Heimaey	UMIAMI	61.50E	67.70S	-	SU	1991-1998	marine
12) Mawson	UMIAMI	126.48E	33.52S	-	SU	1987-1996	marine
13) Palmer	UMIAMI	64.05W	64.77S	-	SU	1990-1996	marine
14) Marsh K. G. I.	UMIAMI	58.30W	62.18S	-	SU	1990-1996	marine
15) Invercargill	UMIAMI	168.35E	46.43S	-	SU	1983-1996	marine
16) Chatam I.	UMIAMI	176.50W	43.92S	-	SU	1983-1996	marine
17) Wellington	UMIAMI	174.87E	41.28S	-	SU	1987-1996	marine
18) Cape Grim	UMIAMI	144.68E	40.68S	-	SU	1983-1996	marine
19) Cape Point	UMIAMI	18.48E	34.35S	-	SU	1992-1996	marine
20) Norfolk I.	UMIAMI	167.98E	29.08S	-	SU	1987-1997	marine
21) Yate	UMIAMI	167.00E	22.15S	-	SU	1983-1985	marine
22) Reunion I.	UMIAMI	55.83E	21.17S	-	SU	1990-1996	marine
23) A. Samoa	UMIAMI	170.58W	14.25S	-	SU	1983-1996	marine
AOD at 500nm							
num. stations	*network/campaign*		*region*		*parameter*	*years*	*category*
152	AERONET		worldwide		AOD at 500nm	2002–2006*	rural/remote/ urban/marine

∗ sites with at least 3 years of available measurements of monthly mean values

Africa and in the Central and South America. Eastern Europe is also characterized by relative maximum values over $2\mu g/m^3$. The simulated global distribution of organic aerosol is mainly governed by fire-emitted particles. The most relevant simulated long-range transport of biomass-burning organic aerosol is the west-ward plume extending from Africa over the Atlantic Ocean, which is characterized by annual mean surface concentrations over $1\mu g/m^3$. The maximum values simulated in anthropogenic regions (where biomass-burning aerosols may also play a relevant role), such as US or Europe, are lesser than $2\mu g/m^3$. The simulated biogenic SOA surface concentrations are maximum in Central Africa, in the East and South-East Asia, in South America (maximum in the Andes), and in the Northern Australia, reaching values around $1\mu g/m^3$ or more. In Australia the contribution of SOA to the total concentration of organic aerosol is more than 50%. Relevant contributions over 30% are found in the Southern US, in Alaska, in the Amazon Forest, in the Andes, in the Antarctic region, and in the Iberian Peninsula in Europe.

Table 13 shows the model total budgets and lifetime of organic aerosols. The simulated annual emissions (108.6Tg/y), annual mean load (1.5Tg), wet deposition fraction (74.7%), and lifetime (5.1 days) of organic aerosol are very close to the median values found in TS14. The same result is found when focusing on POA (4.1days of lifetime, TS14 median value: 4.8 days). For the SOA we obtain a lifetime around 9 days, which is higher than the TS14 median value (6.1 days): this is mainly due to our implementation of a two-product biogenic SOA mechanism in the model, which leads to a longer life in the atmosphere of such particles with respect to models using mechanisms with constant-yield conversion of terpenes to SOA. Together with black carbon, SOA are the longest-lived aerosols in our simulations. The global contribution of SOA to the total organic aerosol load (1.5Tg) is around 0.5Tg.

The scatterplots in Fig. 23 compare the simulated concentrations of organic carbon over US and Europe, where geographically distributed and continuous measurements are provided

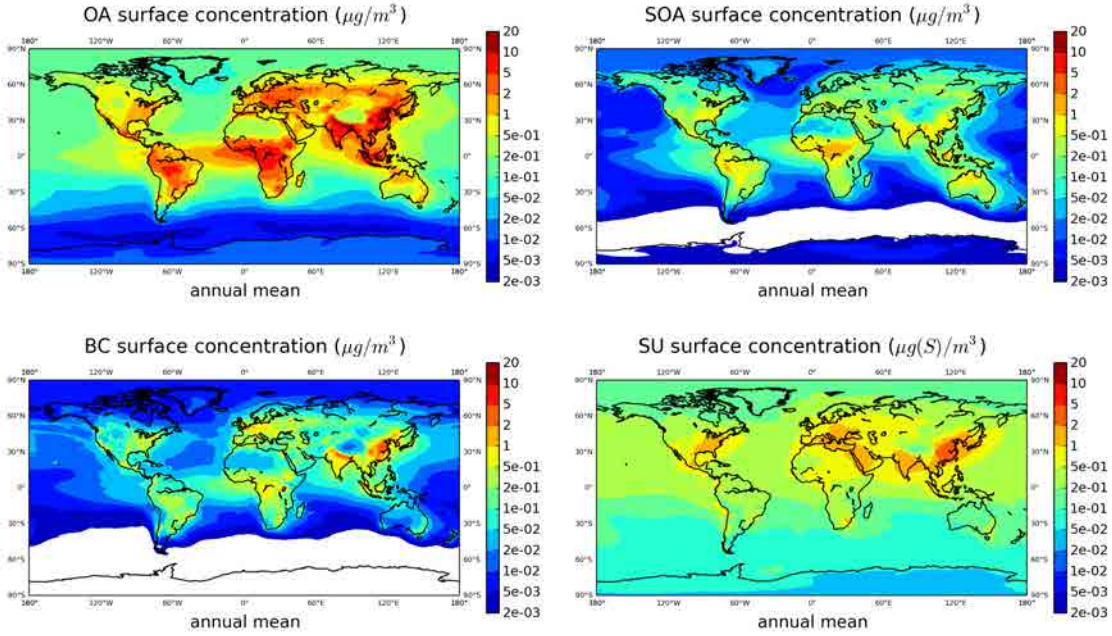

Figure 22: Simulated organic aerosol, SOA, black carbon, and sulfate annual mean surface concentrations (interannual average over 2002−2006).

by rural/remote stations of the IMPROVE and EMEP networks. In the US, we observe a strong agreement between model and IMPROVE PM2.5 measurements: the overall correlation of monthly mean values is around 0.76 i.e. well over the maximum correlation achieved by the AC-II models (0.56) (see Table 14). The overall RMSE ($0.39 \mu g/m^3$) is also markedly lower than the AC-II minimum value ($0.73 \mu g/m^3$). Since the organic aerosol annual cycle in the US rural/remote stations is mainly driven by the SOA summer peak (see also the stations shown in Fig. 24), we relate this agreement between model and observations with the good performance of the two-product SOA production scheme. On the contrary, when comparing with EMEP in Europe, we find very low correlation values (0.05) and marked model underestimates (around -60%), both for PM2.5 and PM10 organic carbon. The same problem is found by the AC-II models, presenting low correlations ranging from 0.02 up to 0.3 (median: 0.12). The main explaination of this problem is that a relevant number of the EMEP sites could be not representative of the global air, since they are affected by local/regional pollution sources (as, for example, the Ispra station). Another explaination can be found in the lack of an appropriate standardized method of organic carbon and elemental carbon determination affecting the EMEP measurements performed in the simulated temporal window (Cavalli et al., 2010), i.e. before the improvement of the EMEP protocol done in 2008 (Tørseth et al., 2012). Additional uncertainties are introduced by the neglection of seasonality in the anthropogenic emissions used in this work and/or by the missing of relevant primary sources in the emission inventory (such as the wood-burning sector, as suggested by Karl et al. (2009)). The missing of anthropogenic SOA in our module could be also play a role in the underestimates, although this hyphotesis has been considered less probable in Karl et al. (2009).

Fig. 24 shows the simulated and observed organic carbon annual cycle at nine specific

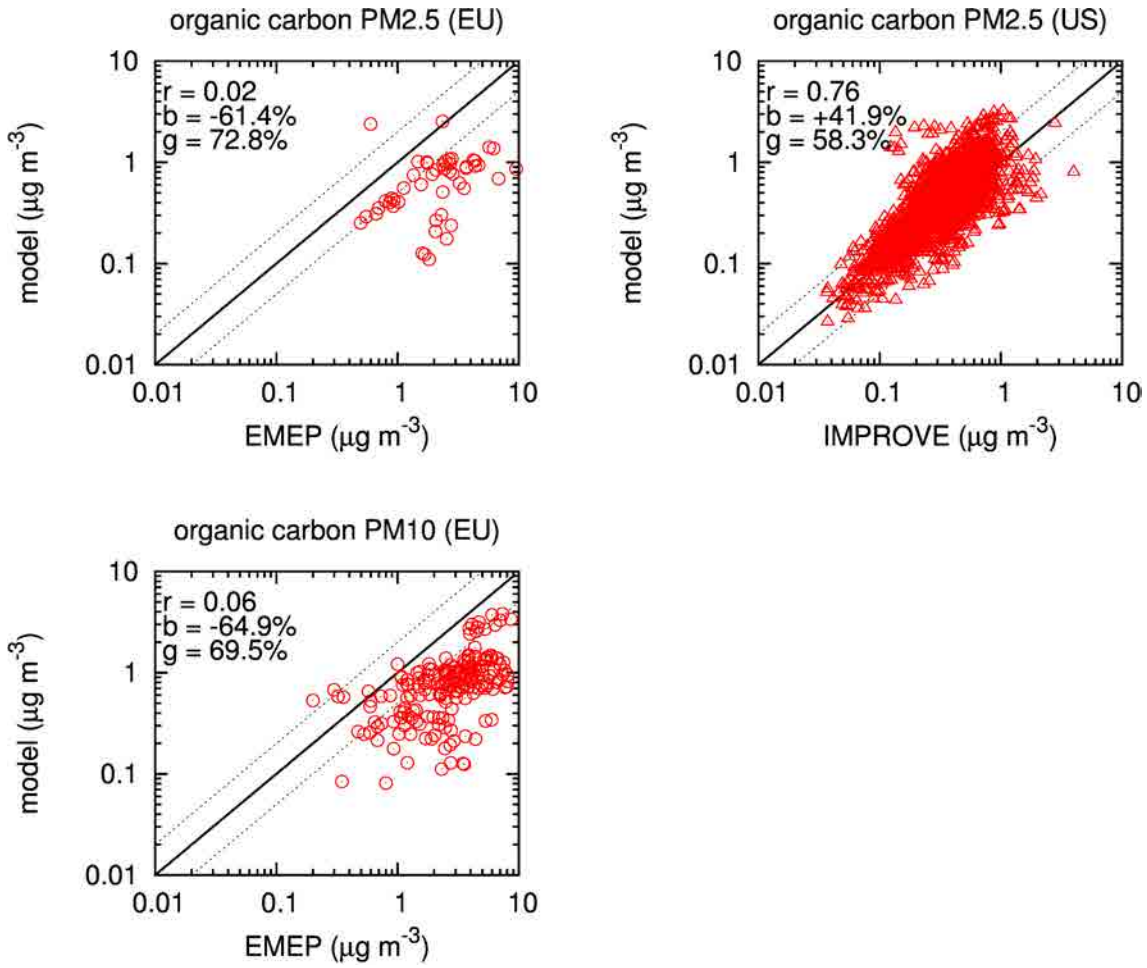

Figure 23: Organic carbon: scatterplots of simulated vs observed PM2.5 and PM10 monthly mean concentrations in Europe (EU) and United States (US). EU and US observations are from EMEP and IMPROVE networks, respectively. r, b, and g stand for mean correlation, normalized bias, and normalized gross error. 1:1 (black solid), 1:2 (black dotted), and 2:1 (black dotted) lines are also shown. Model and observed values are interannual averages over the same period (2002–2006).

remote sites in the world (sites investigated in TS14). Due to the lack of globally distributed observations of organic aerosol surface concentrations, this small number of stations represents the more comprehensive worldwive dataset to evaluate the model currently. We observe that the annual cycle of the US stations – Ohio (a), Colorado (b), Arizona (c), Georgia (d), and Alaska (g) – is decisively influenced by SOA, which are minimum in the boreal winter and maximum in the boreal summer. In these sites, the model is able to reproduce the observations with a good correlation (around 0.8), with two exceptions. The August maximum at Alaska (g) due to fire episodes is not well simulated by the model and it affects the calculated low correlation (0.30). The winter enhancement of concentrations at the Georgia (d) station is not captured by the model, probably because the lack of seasonality in the anthropogenic emission. The Manaus (h) station is also influenced by the SOA cycle, but the dominant contribution simulated by the model is due to the fire-emitted POA; the combination of SOA and biomass-burning POA leads of a very good correlation with observations (around 0.81). The Finokalia (e) measurements are markedly underestimated (MNB: -71%) and weakly correlated (0.31) with the SOA-driven annual cycle simulated by the model. Similar underestimates and low correlation values are found in TS14. As reported in TS14 (after a comparison with AMS measurements), the Finokalia (e) measurements are characterized by relevant seasonal variations of the OA/OC ratio, that are not taken into account by most of the models and that can explain our low model performance there. The organic aerosol annual cycle measured by the AMS station at Welgegund (f) in South Africa is overall reproduced by the model, although the model is missing or underestimating the marked observed peaks in March, July, September and October. In the TS14 work a better agreement of the Welgelgund (f) observations with models is found when VBS approaches are used instead of two-product SOA schemes. We stress again the AMS measurements are referred to organic aerosol and, consequently, the use of the same conversion OA/OC ratio (1.8) for all our organic aerosol tracers, independently from the aerosol source/type, can affect the model performance in the Welgegund (f) region. Negative correlation (-0.46) and strong underestimates (-87%) of model with observations are found at Amsterdam Island (i). As shown by TS14, most of the models (and that is our case) are missing the dominant contribution to the total organic aerosol of this site, that may be attributed to the marine POA production.

Black carbon. The simulated annual mean surface concentration of black carbon is shown in Fig. 22 (bottom-left panel): absolute maximum values around $2\mu g/m^3$ or more are found in East Asia (Northern India and China) and relative maximum values ($0.5\mu g/m^3$) are found in Central/Eastern Europe, Central Africa, South-East Asia, and specific hotspots that are affected by anthropogenic or biomass-burning emissions.

As presented in Table 13, our simulation of the black carbon life-cycle is considerably different with respect to the median results obtained by the models involved in the AC-II, ACB, and SH13 experiments. We simulate a global load (0.19Tg) greater than the median value provided by other experiments (0.12Tg in AC-II and 0.13Tg in SH13) and similar to the ACB value (0.21Tg). The enhanced ACB load is consequent to higher black carbon emissions (11.3Tg/y) than those prescribed by ACCMIP and used in this work (7.7Tg/y). This model behavior can be explained by the fact that the wet deposition fraction of the total removal (53.3%) is not dominating the total deposition as in other models. In particular, we find that the contribution of convective scavenging to the wet deposition is low (28.0%). With an overall lifetime of 9.1days, black carbon is the longest-lived aerosol species in our simulations.

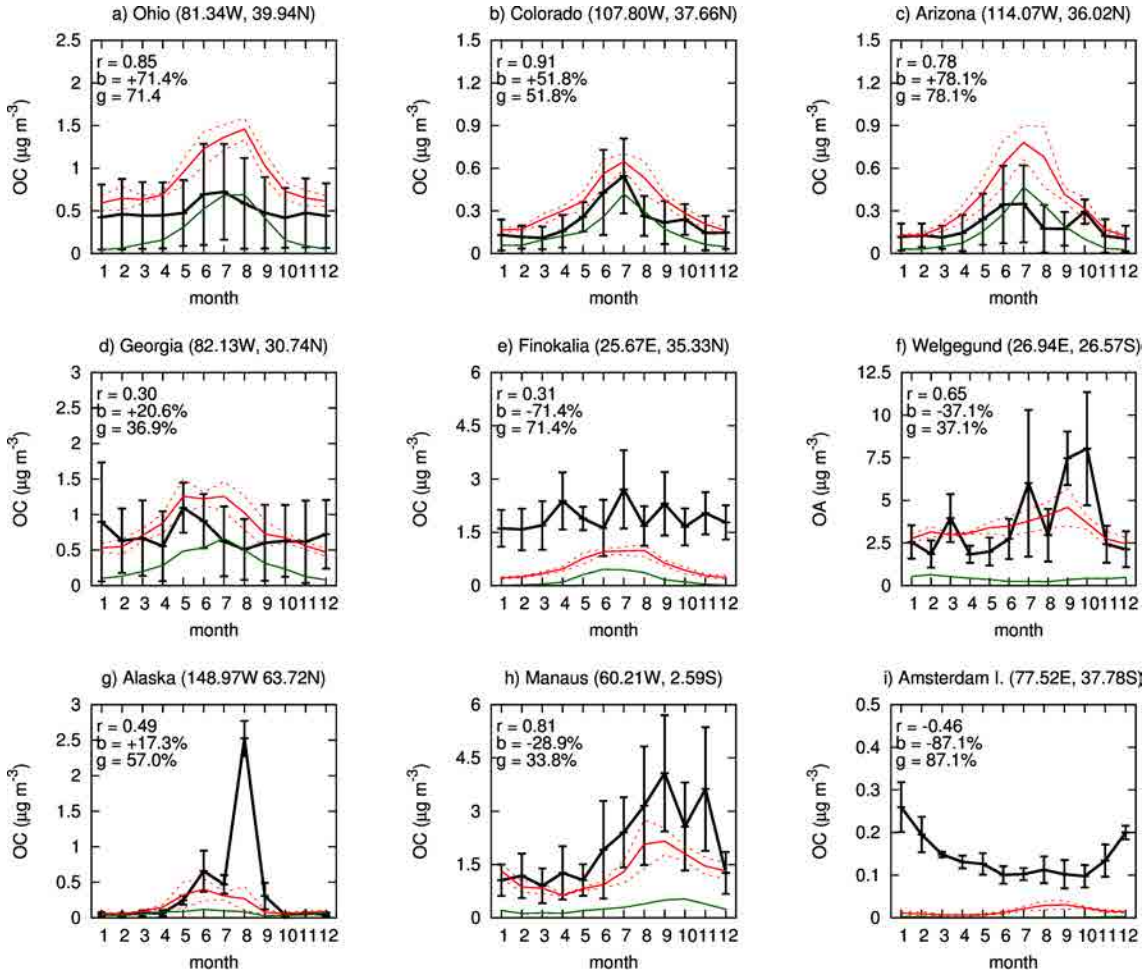

Figure 24: Organic carbon: comparison of simulated (solid red lines) with observed (solid black lines) monthly mean surface concentration at nine sites worldwide (specific sites considered by TS14, Tsigaridis et al. (2014)). Simulated (dotted red lines) and observed (black bars) interannual standard deviation are also shown. Green lines show the contribution of SOA to the total organic carbon concentration. r, b, and g stand for mean correlation, normalized bias, and normalized gross error. Model and observed values are interannual averages over different periods (simulated: 2002–2006, measurements: see Table 11).

The scatterplots in Fig. 25 show that the model monthly mean values are weakly correlated both with the IMPROVE and the EMEP measurements (correlations around 0.3–0.5) and the errors (gross and RMS) are very high (gross error over 100% in the US). A strong positive bias is observed when comparing with IMPROVE (+92%). As discussed for the case of the organic carbon, the comparison with EMEP data may be affected by the presence of sites which are subjected to local/regional pollution sources (e.g. Ispra). Similar uncertainties are encountered by the other state-of-the-art models, such as those involved in AC-II, which show negative correlation values in Europe (see Table 14).

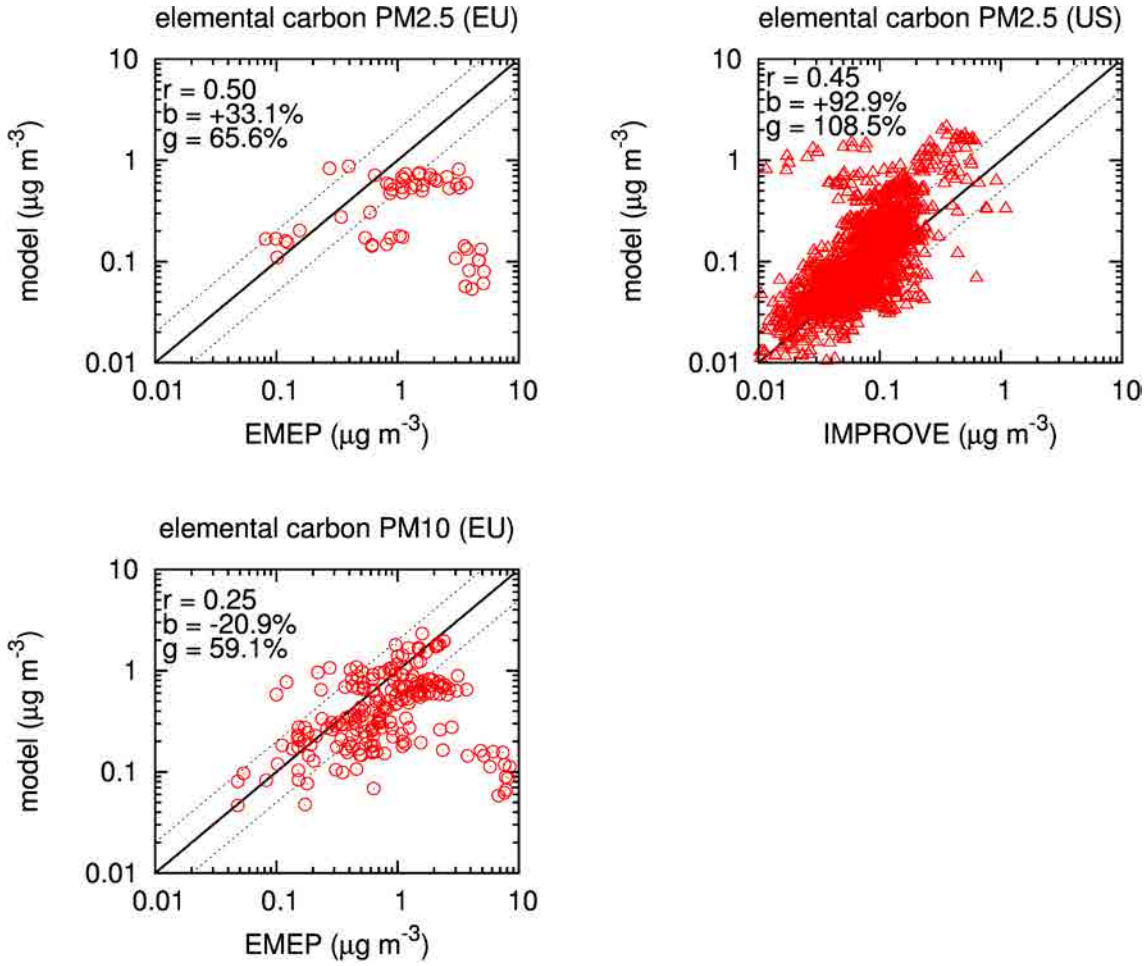

Figure 25: Elemental carbon: scatterplots of simulated vs observed PM2.5 and PM10 monthly mean concentrations in Europe (EU) and United States (US). EU and US observations are from EMEP and IMPROVE networks, respectively. r, b, and g stand for mean correlation, normalized bias, and normalized gross error. 1:1 (black solid), 1:2 (black dotted), and 2:1 (black dotted) lines are also shown. Model and observed values are interannual averages over the same period (2002–2006).

Fig. 26 shows the simulated and observed black carbon annual cycle at fourteen sites in the Northern Hemisphere, which have been considered in the LE13 model intercomparison work. Observations are AMS measurements, then the evaluation could be affected by inconsistencies between model and measurement description of black carbon optical properties (the assumptions done in the elaboration of observations are reported in LE13). When

comparing model monthly means with LE13 stations, we find a good agreement in most of them; Ny Alesund (B), Barrow (C), Pallas (D), Hyytiala (E), Preila (F), Mauna Loa (O), and Jungfraujoch (P) are characterized by correlation ranging from 0.51 up to 0.97. In particular, the annual cycle observed in Barrow (C) with the spring maximum and the summer minimum is reasonably well captured by the model, while most (all, with the exception of HadGEM2) of the LE13 models are simulating a spurious maximum peak and minimum concentrations in winter-spring. This good performance of model in Barrow (C) could be mainly related with the use of the IS4FIRES fire injection heights, since the use of prescribed heights according to Dentener et al. (2006) leads our model to simulate a markedly different annual cycle, similar to the LE13 models and weakly correlated with observations (not shown). In the remaining stations we observe low correlations: 0.28 at Alert (A), 0.12 at Mace Head (G), 0.41 at Sable Island (I), 0.28 at Trinidad Head (L), and 0.14 at Southern Great Plains (M). Ispra (H) and Bondville (N) show very low or negative correlations (0.06 and -0.22, respectively) and that can be related with their perturbed continental site category, which is not well reproduced by the model: this result suggest that the coarse resolution and the neglection of seasonality in the anthropogenic emissions are affecting the simulated annual cycles. Same problem is probably affecting the other two perturbed stations in study i.e. Sable Island (I) and S. G. Plains (M). With the exception of Alert (A), where the simulated maximum is postponed to may with respect to the observed one in march, the model is well capturing transport cycle from the continents to Arctic or sub-Arctic stations (Ny Alesund (B), Barrow (C), and Pallas (D)) in the boreal winter-spring. However, the simulated concentrations present a negative bias ranging up to -78%, bias which is very marked in the Arctic stations. Since the same underestimates are found in LE13, we argue that relevant uncertainties still affect the state-of-the-art modeling of black carbon emissions and transport.

Sulfate. The global distribution of the sulfate annual mean surface concentration (bottom-right panel of Fig. 22) is characterized by maximum values reached in the Chinese region, over $2\mu g(S)/m^3$. Relative maxima are found in the Eastern US, in the Mediterranean Sea and in the Eastern Europe, in the Arabian Peninsula, and in India ($1\mu g(S)/m^3$ or more). Other specific regions affected by biomass-burning and volcanic emissions can also reach annual mean concentration above $1\mu g/m^3$. The sulfate production from DMS dominates the surface concentrations over the oceans in the Southern Hemisphere (around $0.05\mu g(S)/m^3$), which are nearly one order of magnitude lesser than those dominated by the transport from continents over the oceans in the Northern Hemisphere (around $0.2\mu g(S)/m^3$ or more).

The overall load in the years 2002–2006 is around 1Tg (see Table 13), which is close to the the median value provided by AC-II for the year 2006 (1.3Tg) and lesser than the SH13 and ACB values for the year 2000 (median values: 2.2Tg and 2.0Tg, respectively) mainly due to a lesser sulfate production (110.2Tg/y instead of the 186.0Tg/y ACB median). The simulated sulfate lifetime is 3.5 days, longer than the median value of AC-II (1.3 days) but similar to SH13 and ACB median values (4.1 days in both cases). Globally, the wet deposition dominates the total removal of sulfate (86.4%) and the main mechanism of removal can be addressed to the grid-scale wet scavenging (being the relative contribution of convective scavenging around 26%), in agreement with the multi-model results obtained in ACB.

Fig. 27 (top-central panel) show a high correlation (r=0.84) between the simulated monthly mean concentrations and the PM2.5 measurements provided by the IMPROVE network over the US, very similar to the AC-II median value (0.86). A marked positive bias

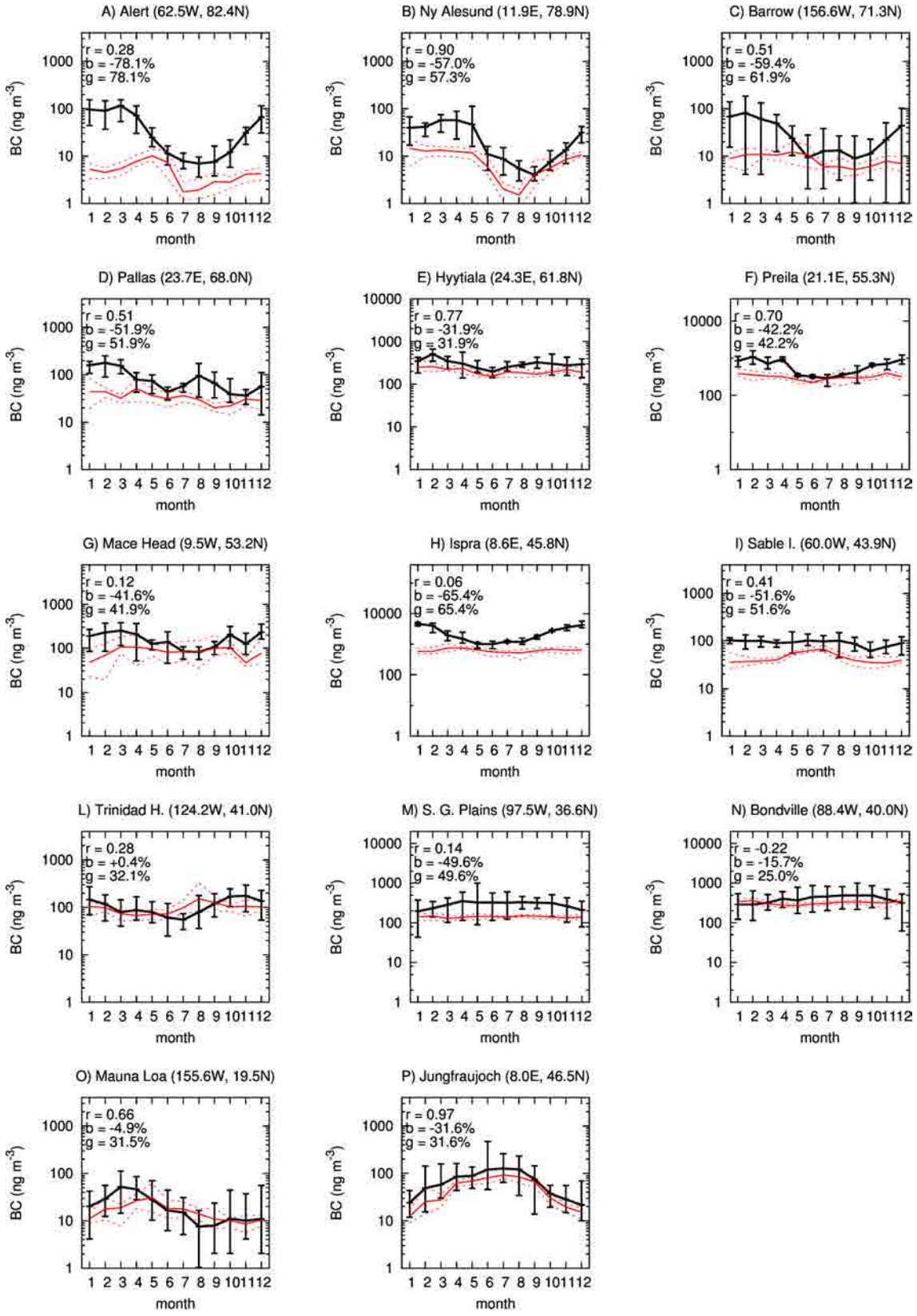

Figure 26: Black carbon: comparison of simulated (solid red lines) with observed (solid black lines) monthly mean surface concentration at fourteen sites in the Northern Hemisphere (specific sites considered by LE13, Lee et al. (2013)). Simulated (dotted red lines) and observed (black bars) interannual standard deviation are also shown. r, b, and g stand for mean correlation, normalized bias, and normalized gross error. Model and observed values are interannual averages over different periods (simulated: 2002–2006, measurements: see Table 11).

(+61%) is found, due to the model tendency to overestimate the low concentrations values which characterize stations located in the mountainous western US. As shown in Fig 27 (top-right panel), we find a decrease of bias to an overall value of +0.3% when avoiding from the comparison the stations characterized by altitudes higher than 1000m. The model overestimates of low concentrations at mountainous sites can be mainly addressed to the model resolution, both vertical and horizontal, which may markedly affect the transport of aerosol particles in regions affected by strong orographic gradients (Spada et al., 2015). Additional uncertainties are introduced by the off-line coupling of sulfur chemistry with climatological OH and O_3 fields, since they are affected by model overestimates in the tropics (Badia, 2014). The lack of both a size-resolved description of sulfate aerosol and coagulation with other particles can also play a role. In Europe, when comparing with EMEP PM2.5 (top-left panel) and PM10 (bottom-left panel) measurements, we obtain correlations around 0.5 which are in the higher range of the AC-II results (median value around 0.37). In the Eastern-Asia, the overall correlation with the EANET measurements is also around 0.5.

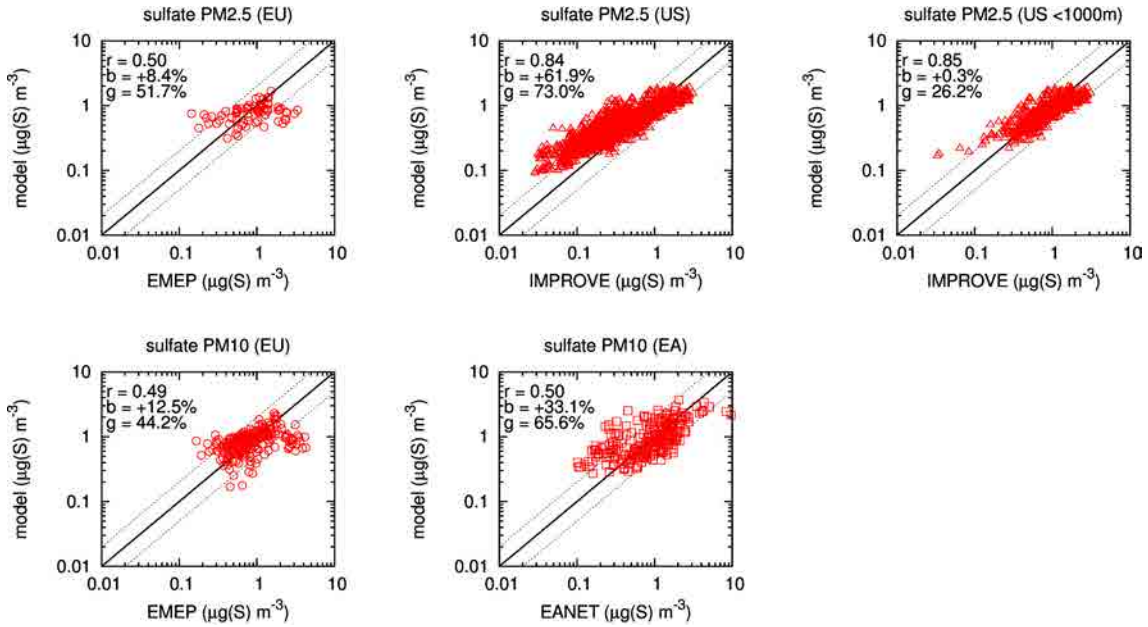

Figure 27: Sulfate: scatterplots of simulated vs observed PM2.5 and PM10 monthly mean concentrations in Europe (EU), United States (US), and East Asia (AS). EU, US, and EA observations are from EMEP, IMPROVE, and EANET networks, respectively. r, b, and g stand for mean correlation, normalized bias, and normalized gross error. 1:1 (black solid), 1:2 (black dotted), and 2:1 (black dotted) lines are also shown. Model and observed values are interannual averages over the same period (2002–2006).

The simulated annual cycles of sulfate concentrations are evaluated at specific measurement sites of the UMIAMI network, both in the Northern (Fig. 28) and in the Southern (Fig. 29) Hemisphere, as performed by Liu et al. (2005). The transport of anthropogenic and biomass-burning sulfate dominates at the UMIAMI stations in the Northern Hemisphere (Fig. 28). Despite the use of constant anthropogenic emissions during the year, the model seems to be able to reproduce well the annual cycles of most of the these stations, with a correlation above 0.5 at Barbados (2), Oahu (3), Midway Island (5), Izana (6), Miami (7), Bermuda (8), Mace Head (10), and Heimaey (11). However, we find strong overestimates

at Oahu (3) during the whole year and Midway Island (5) in the boreal summer. The case of Oahu (3) can be addressed to overestimates in the simulation of volcanic aerosol, while the spurious summer-peak at Midway Island (5) can be mainly related with the sulfate production due to the DMS (since both the DMS emission flux and the offline OH field are maximum show pronounced maximum values over the Northern Pacific in the summer). The shift of the maximum values of Mace Head (10) and Heimaey (11) observed in may to the simulated ones in June/July can be also referred to the uncertainties in the the description of DMS emission and chemistry. The several tests performed on the DMS chemistry (varying the reactions set from different literatures) during the module development have not lead to important differences in the simulation of sulfate aerosol in these regions (not shown). Since the spurious model maximum sulfate concentration during the boreal summer found in the tropical stations corresponds to the summer maximum of DMS emissions and OH concentration, we relate the model errors mainly with overestimates of theoff-line emission fluxes and/or climatological OH. The negative correlation (-0.11) found at Fanning Island (1) is not critical, because the flat shape of the annual cycle. The low correlations (around 0.25) found at Hedo Okinawa (4) and Cheju Korea (9) suggest that the the use of constant anthropogenic emissions during the year could be critical in these regions.

The sulfate production in the Southern Hemisphere is mainly driven by emission of DMS (but biomass-burning emissions can be also important in specific regions): this reflects in the typical U-shape annual cycle which is found at these stations, with maximum values in the austral summer and minimum values in the austral winter (Fig. 29). With the exceptions of Cape Point (19) (flat annual cycle) and Yate (21) (the minimum value observed in May is simulated in July by the model), all the other stations show correlations above 0.5 and most of them are above 0.7. But, despite of correlation, the maximum values assumed in the austral summer are generally overestimated. This evidences again the model uncertainties in the estimate of DMS production and/or chemistry to form sulfate aerosol. The systematic overestimate at American Samoa (23) can be also related with overestimates of the volcanic contribution to the total sulfate.

At marine sites, spurious maximum values in the boreal summer in the Northern Hemisphere and overestimates during the boreal winter in the Southern Hemisphere were also found in the work of Liu et al. (2005). Note that in Liu et al. (2005) a global DMS emission flux estimate of 26.1Tg(S)/y (based on) was applied, that is very close to the value provided by HAMOCC5 for the year 2000 (27.6Tg(S)/y) and used in this work. Even if the value prodvided by HAMOCC5 is within the range of $[15-33]$Tg(S)/y suggested by Kettle and Andreae (2000), it is higher than the range of fluxes used by other model studies $[10.7-23.7]$Tg(S)/y (Rotstayn and Lohmann, 2002). Rotstayn and Lohmann (2002) found a strong sensitivity of the DMS emission estimates depending on the parameterization used to couple the surface wind speed with the DMS concentrations in the ocean. In particular, they found a clear improvement of model results when the global emission flux is reduced from 22.1Tg(S)/y to 14.3Tg(S)/y.

Aerosol Optical Depth. The simulated annual mean all-sky AOD at 550nm is presented in Fig. 30 (top-left panel) and discussed in the following. The model diagnostic clear-sky AOD is also shown (top-right panel) with the purpose to compare with satellite (MODIS and MISR: bottom left and right panels, respectively) and AERONET observations. As an additional support of our discussion, Fig. 31 shows the relative contribution of each simulated

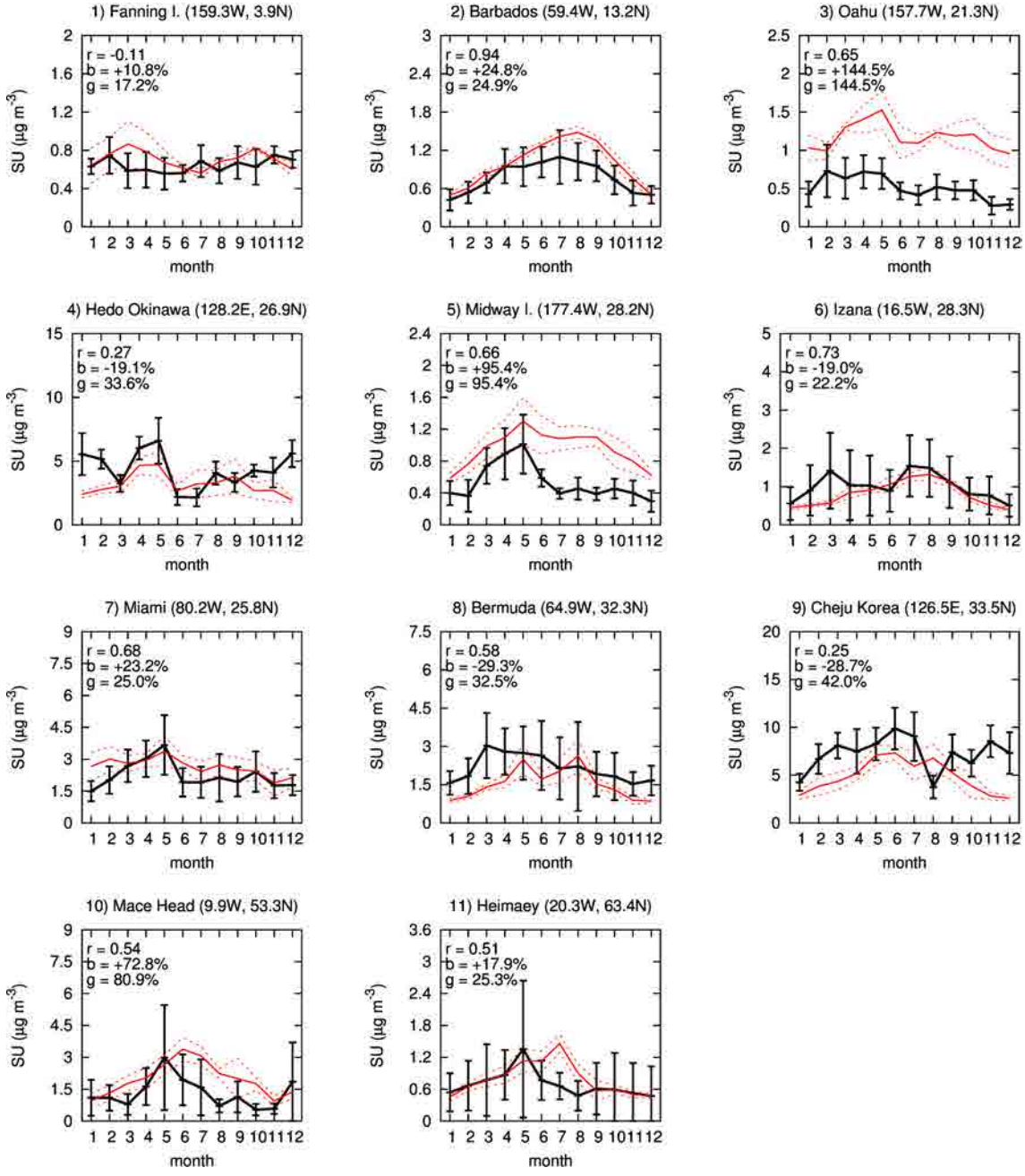

Figure 28: Sulfate: comparison of simulated (solid red lines) with observed (solid black lines) monthly mean surface concentration at eleven sites in the Nothern Hemisphere (specific sites from the University of Miami Network, see also Liu et al. (2005)). Simulated (dotted red lines) and observed (black bars) interannual standard deviation are also shown. r, b, and g stand for mean correlation, normalized bias, and normalized gross error. Model and observed values are interannual averages over different periods (simulated: 2002–2006, measurements: see Table 12).

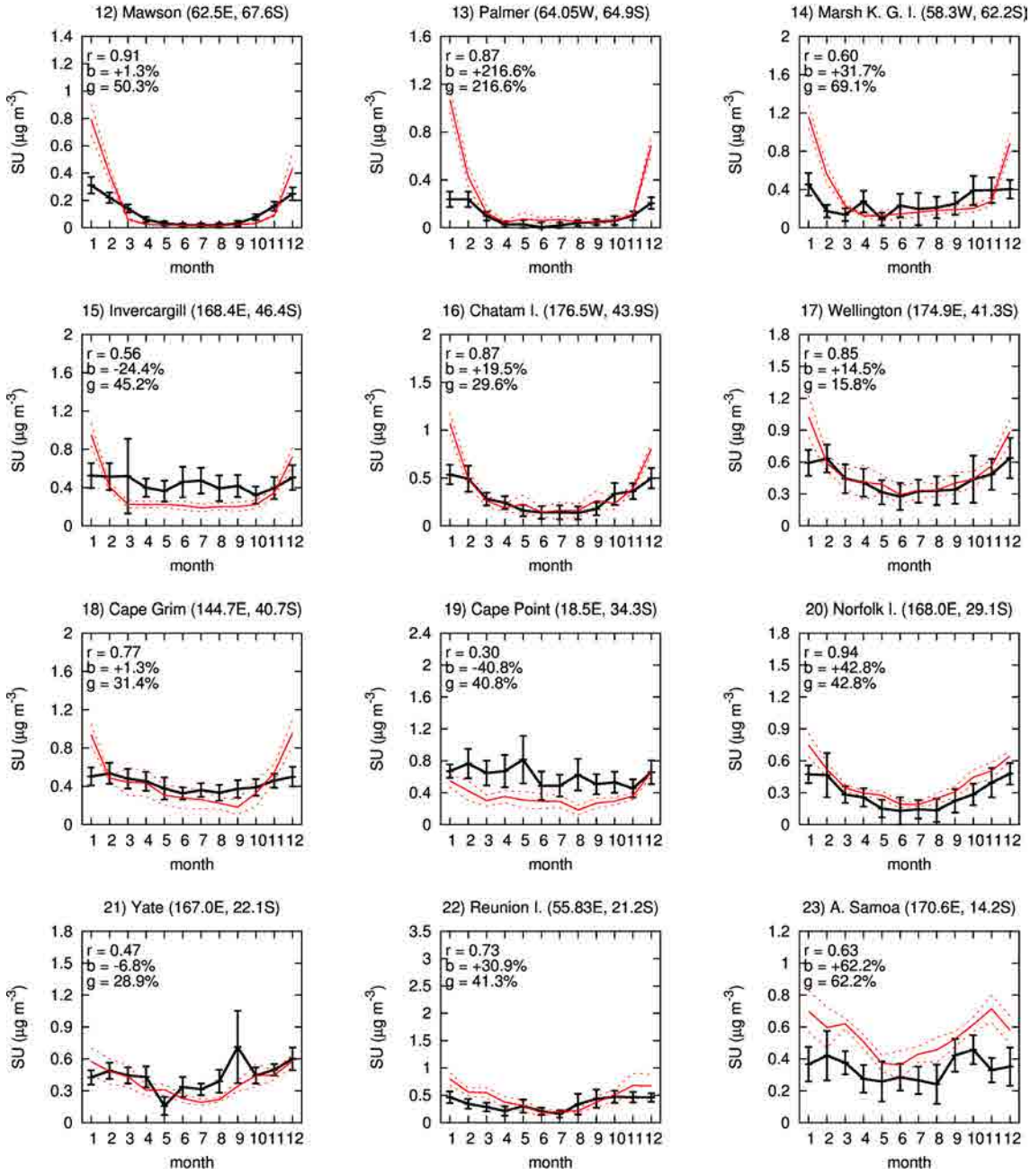

Figure 29: Sulfate: comparison of simulated (solid red lines) with observed (solid black lines) monthly mean surface concentration at twelve sites in the Southern Hemisphere (specific sites from the University of Miami Network, see also Liu et al. (2005)). Simulated (dotted red lines) and observed (black bars) interannual standard deviation are also shown. r, b, and g stand for mean correlation, normalized bias, and normalized gross error. Model and observed values are interannual averages over different periods (simulated: 2002–2006, measurements: see Table 12).

Table 13: Simulated totals of aerosol emissions (emi), load, wet deposition fraction of the total deposition (wdep/dep), convective fraction of the wet deposition (convwdep/wdep), and lifetime (life) (averages over 2002−2006) and comparison with other studies. Square brackets indicate minimum, median, and maximum values provided by AC-II. Round brackets indicate values found in TS14. Curly brackets indicate values provided by SH13. Slashes indicate values from ACB.

aero	emi (Tg/y)	load (Tg)	wdep/dep (%)	convwdep/wdep (%)	life (days)
OA	108.6	1.5	74.7%	57.7%	5.1
	$(-, 97, -)$	$(0.6, 1.4, 3.8)$	$(-, 85\%, -)$	–	$(3.8, 5.4, 9.6)$
POA	87.0	1.0	73.0%	57.5%	4.1
	$(34, 56, 144)$	–	–	–	$(2.7, 4.8, 7.6)$
	$/-, 96, -/$	$/-, 1.8, -/$	$/-, 78.9\%, -/$	$/-, 54.5\%, -/$	$/-, 6.2, -/$
SOA	21.6	0.5	81.4%	58.5%	9.0
	$(13, 19, 121)$	–	–	–	$(2.4, 6.1, 14.8)$
BC	7.7	0.19	53.3%	28.0%	9.1
	$[5.2, 7.7, 10.3]$	$[0.07, 0.12, 1.07]$	–	–	$[3.6, 6.1, 48.7]$
	$/-, 11.3, -/$	$/-, 0.21, -/$	$/-, 79.5\%, -/$	$/-, 44.6\%, -/$	$/-, 6.5, -/$
	$\{7.7, 7.8, 8.8\}$	$\{0.06, 0.13, 0.32\}$	–	–	$\{3.9, 6.0, 15.2\}$
SU	110.2	1.0	86.4%	26.0%	3.5
	–	$[0.4, 1.3, 4.5]$	–	–	$[1.1, 1.3, 9.3]$
	$/-, 186.0, -/$	$/-, 2.0, -/$	$/-, 88.5\%, -/$	$/-, 35.2\%, -/$	$/-, 4.1, -/$
	–	$\{1.5, 2.2, 2.8\}$	–	–	$\{3.0, 4.1, 7.9\}$

aerosol species to the total all-sky AOD at 550nm.

The global distribution of the simulated all-sky AOD is characterized by three maximum value regions exceeding the annual mean value of 0.5: the Western and Central Africa, where the AOD is governed by desert dust and biomass-burning aerosols – respectively – , the South-Eastern Arabian peninsula, mainly due to desert dust aerosol, and the Chinese region, where half of the AOD can be addressed to sulfate aerosol (both from anthropogenic and biomass-burning sources). The strong biomass-burning activity in the Indonesian archipelago leads to other two specific maximum values around 0.5 (or more) in the, mainly characterized by the organic aerosol contribution. The Gobi desert is simulated with an annual mean AOD at 550nm between 0.30 and 0.35. The biomass-burning organic aerosol contribution also dominates the relative maximum (AOD at 550nm up to 0.25) in the Amazonian and Mato Grosso regions in South America. The Eastern Europe and the Northern Russia also show relative maximum values between 0.25 and 0.30, due to the activity of fires in these regions. The remote Southern Oceans are characterized by annual mean AOD values lesser than 0.15. The Northern Pacific is affected by the eastward transport plume from East Asia, reaching values above 0.25, while the eastward transport of the US originated aerosols lead to values between 0.15 and 0.20 in the Northern Atlantic. The westward plume extending from Africa towards South America is simulated with an AOD gradient decreasing from around 0.50 (close to the African sources) to around 0.20 (close to South America).

As already stated, for the comparison with satellite data (bottom panels of Fig. 30) we refer to the diagnostic clear-sky AOD shown in Fig. 30 (top-right panel). The use of the model diagnostic clear-sky AOD instead of the all-sky AOD implies an overall decrease in the annual mean values: in particular, the AOD calculation is markedly reduced in the US, in Europe, and in the East Asia. The comparison with satellite data shows an overall agreement of the simulated AOD with both MODIS and MISR (correlation and biases inside

the range of the SH13 models, see Table 14), but we found that the model clear-sky AOD at 550nm is overestimated in the Western Africa and underestimated in the Central Africa with respect to MODIS. This suggests that our simulations may be affected by important overestimates in the parameterization of dust emissions (online-coupled physical scheme) and by important underestimates in the biomass-burning emissions (from the ACCMIP dataset). Overestimates in the size distribution applied in the parameterization of the dust emission flux were already observed and discussed for the global model in Pérez et al. (2011). Concerning the biomass-burning emissions, it is a well known problem that the state-of-the-art top-down and bottom-up inventories (such as GFED version 2, included in the AEROCOM-ACCMIP emissions used in this work) tend to miss fires and underestimate emission fluxes up to a factor of 4 with respect to satellite observations (Kaiser et al., 2012; Soares et al., 2015). Despite the overestimates of the AOD close to the Western African desert sources, the westward African plume is reproduced in a good agreement with MODIS and MISR (Fig. 30, bottom left and right panels, respectively). The pattern of the simulated Asian plume over the Pacific is in a good agreement with both satellite averages, but we found a strong underestimate of the Eastern Asia AOD which is even more evident when referring to the clear-sky calculations (with respect to the all-sky values). This could be explained inter alia by the absence of the nitrate contribution to the total AOD in our simulations. Hauglustaine et al. (2014) found that the nitrate AOD at 550nm reaches its global maximum value (annual mean value around 0.1) in the Eastern Asia region. The simulated clear-sky AOD pattern of the Atlantic transport is very close to the observations of MISR and in good agreement with MODIS. As for case of African fires, the simulated AOD underestimates the annual mean value provided by MODIS in the Mato Grosso region, while the model tendency to overestimate AOD near to dust sources is overturned in the Gobi desert, which is simulated with an AOD markedly lower than that observed by satellites. In Australia, MODIS and MISR are giving very different AOD values and the model seems to reproduce better the MISR observations than the MODIS ones, which are overbiased by the model. This could be explained by considering that the merged MODIS product is affected by negative biases with respect to AERONET measurements in Oceania (Sayer et al., 2014).

Figure 31 displays the relative contribution of each simulated aerosol species to the total all-sky AOD (annual mean). It is evident that the contribution of black carbon to the total AOD can be considered very low ($\leq 5\%$). Also the contribution of SOA is very low, since the regions where organic aerosol dominates (central South America, central Africa, and Indonesia) are characterized mainly by biomass-burning aerosol. With an overall contribution above 50% over land, the sulfate aerosol clearly dominates the Northern Hemisphere.

For the comparison with AERONET, we calculate the monthly mean correlation (Fig. 33, top panel) and the normalized annual mean bias (Fig. 33, bottom panel) of the model clear-sky AOD in the worldwide measurement sites described in section 4.2.3 (see also Table 12). The dominant aerosol contribution to the total AOD is also highlighted. The overall correlation with AERONET observations is good (around 0.7) and falls in the higher part of the AC-II range $[0.30 - 0.78]$ (matching the maximum value provided by the SH13 models $[0.44 - 0.69]$, see Table 14). Fig. 33 (top panel) evidences that very high correlations are achieved in regions dominated by sulfate and organic carbon. Even in the western US, where a positive bias is found (see Fig. 33, bottom panel) due to sulfate overestimates, the correlation is good. The stations characterized by the Atlantic long-range transport of dust present a higher correlation than the stations close to the dust African sources. The lower correlations (around 0.5) are found in marine stations, where it is difficult to address the uncertainties due

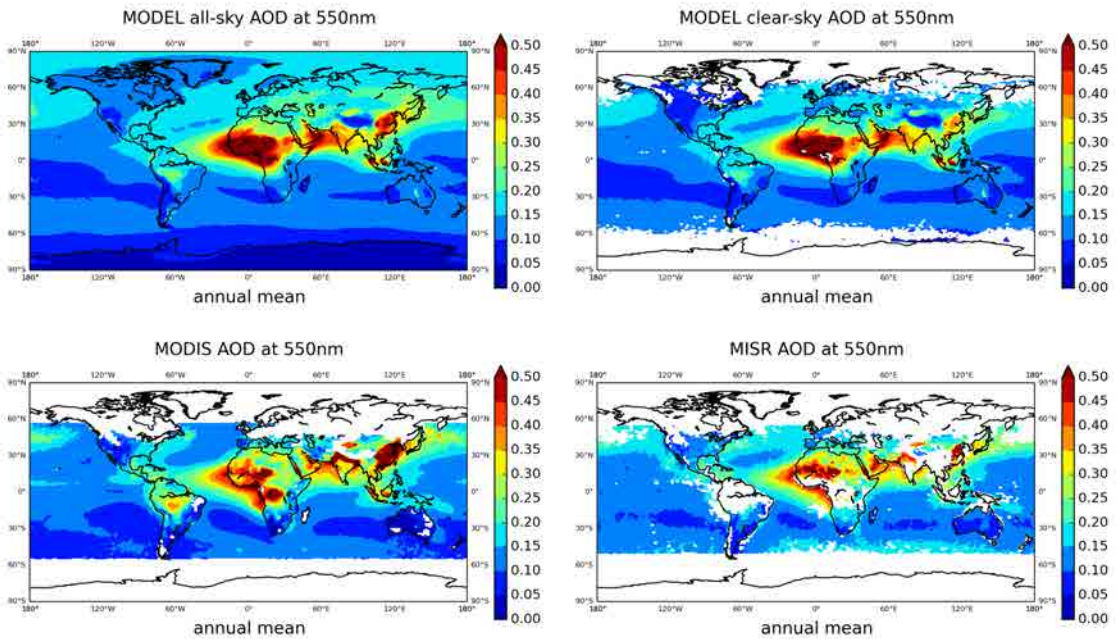

Figure 30: Upper panels: simulated all-sky and clear-sky annual mean AOD at 550nm (interannual average over 2002−2006). Bottom panels: MODIS and MISR AOD at 550nm (interannual average over 2002−2006). Annual mean (model and satellite) values are shown only in gridcells where the complete annual cycle is available. Interannual averages of (model and satellite) monthly mean values have been calculated only in gridcells with at least 3 years of available data.

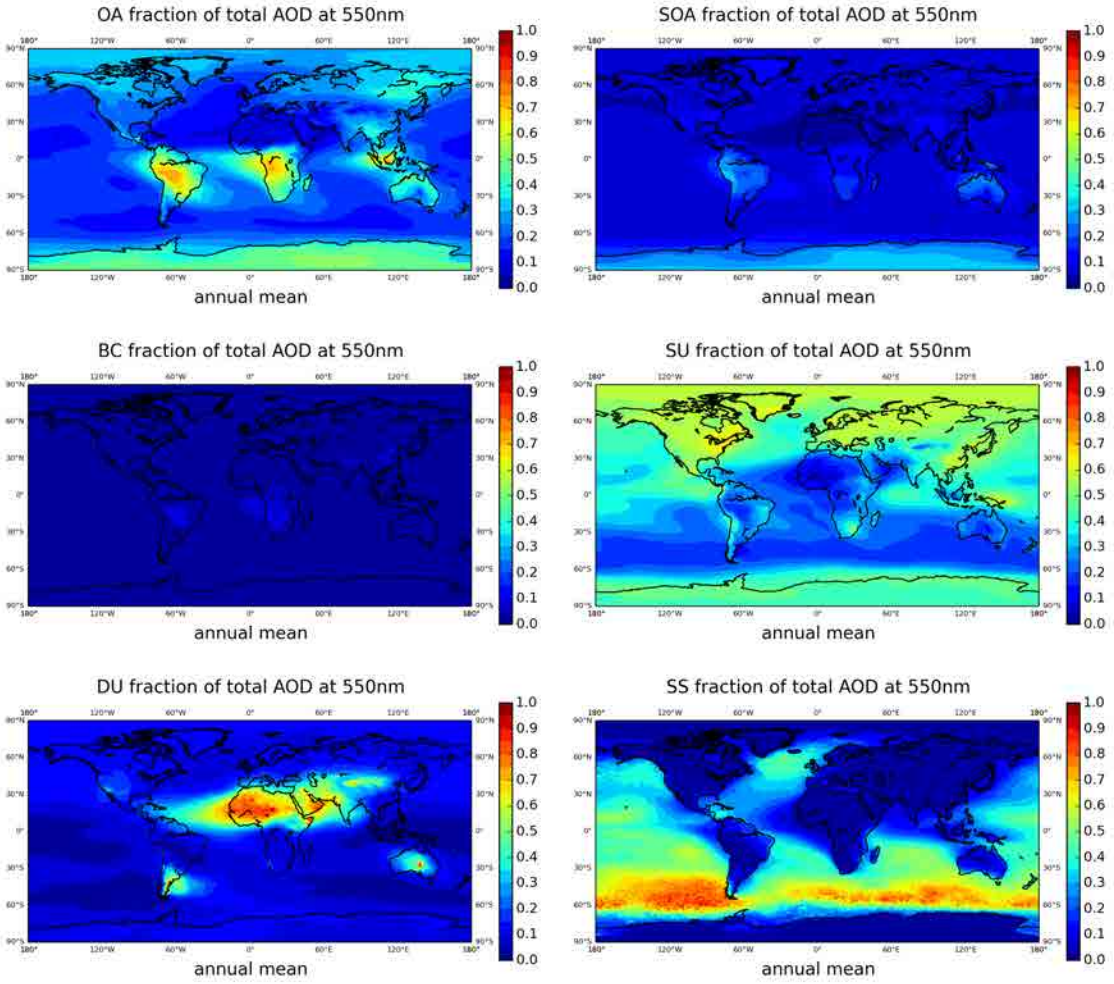

Figure 31: Annual mean fractions of the total all-sky AOD at 550nm due to the contribution of the different aerosol species (interannual average over 2002−2006).

to the combinations of different effects (DMS emissions and sulfate chemistry, off-line oxidants, transport, etc.). Fig. 33 (bottom panel) points out that the comparison with the AERONET AOD is confirming the discussion done for the comparison with satellite observations: the AOD is generally overestimated in regions characterized by dust emissions (see for ex. the Western Africa) and underestimated in sites dominated by the biomass-burning production of organic carbon (Central Africa and South America).
The overall (ALL) resuming scatterplot provided in Fig. 32 highlights the model tendency to overestimate high AOD values (due to dust overestimates) and to overestimate low AOD values (due to the overestimates of low sulfate concentrations in mountainous regions). Fig. 32 also illustrates how the problems in the Western US can be related with stations characterized by altitudes above 1000m and placed in regions affected by steep orographic gradients, which are difficult to be solved by the model at the given resolution. By avoiding these stations from the comparison, the correlation in North America (NA) raises from 0.72 to 0.81, which is close to maximum value achieved by the AC-II models and the normalized bias is reduced from +7.8% to -2.0%. In Europe (EU), the monthly correlation (0.70) reaches the maximum value presented by AC-II. In Eastern Asia (EA) we found a correlation (0.46) which lies in the lower part of the range achieved by the AC-II models; together with the negative bias (-21.1%), this is pointing out that the model is probably missing relevant aerosol emissions and/or species (such as the nitrate for ex.). The scatterplot related with the African region (AF) clearly shows how the higher monthly mean values (due to higher dust concentrations close to their sources) are overestimated by the model. This is due to the use of a dust emission tuning factor which was obtained to fit the Atlantic transport at the global resolution (according to Pérez et al. (2011)) which is affected by the overestimates in the size distribution applied of the emitted dust particles.

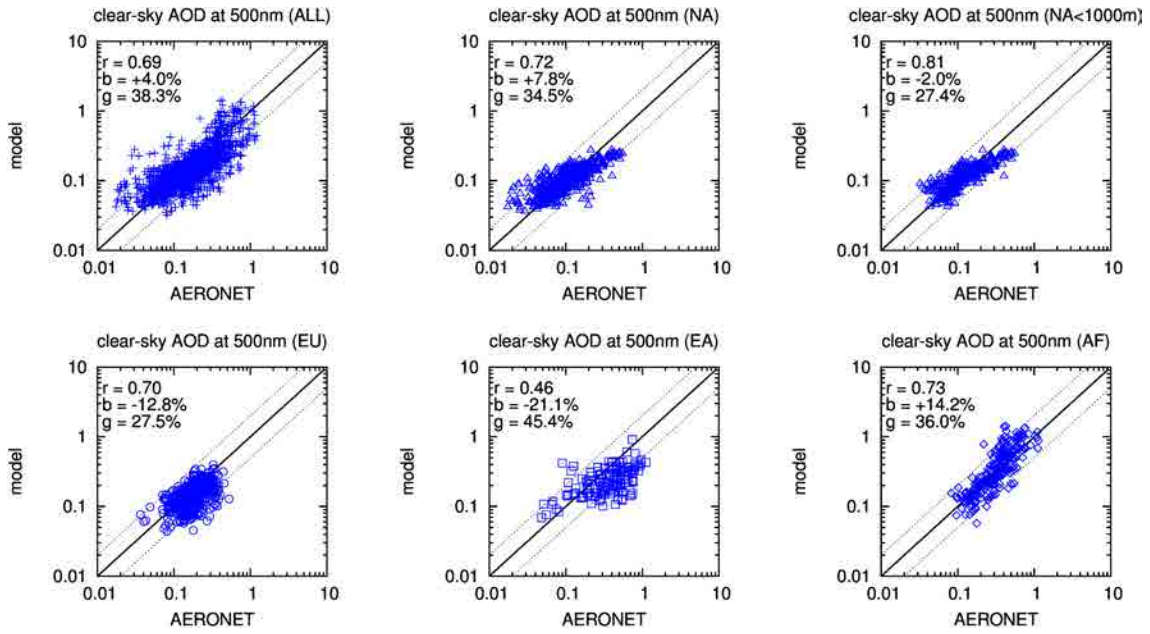

Figure 32: AOD at 500nm: scatterplot of simulated clear-sky AOD vs observed monthly mean AOD (ALL). Scatterplots of specific regions are also shown: Europe (EU), North America (NA), East Asia (EA), and Africa (AF). Observations are from the AERONET sunphotometer network. Model and AERONET monthly mean values have been averaged over the period 2002−2006. AERONET values have been considered only in sites with at least 3 years of available data. r, b, and g stand for mean correlation, normalized bias, and normalized gross error. 1:1 (black solid), 1:2 (black dotted), and 2:1 (black dotted) lines are also shown.

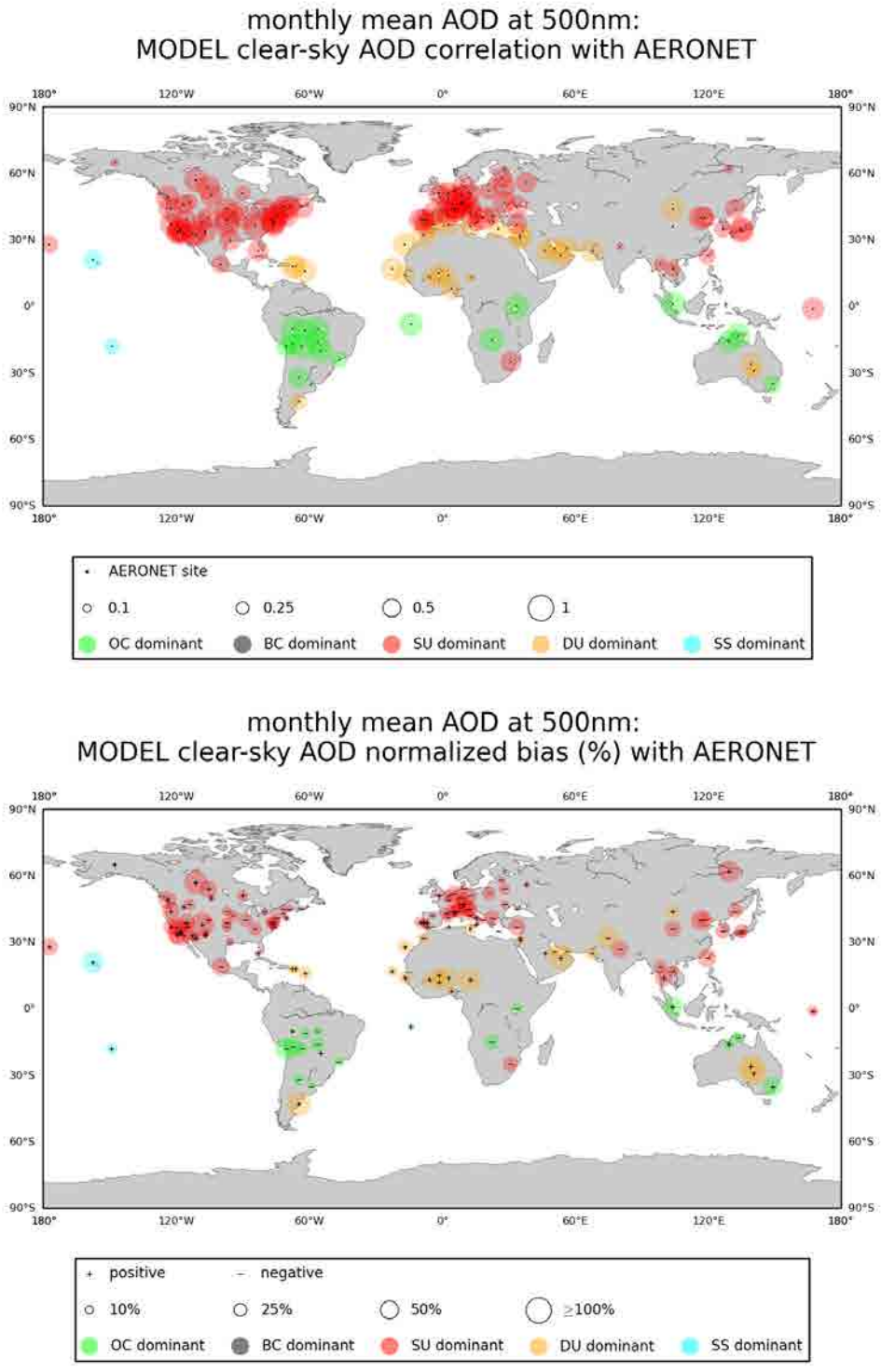

Figure 33: Top panel: correlation of simulated (clear-sky) and AERONET monthly mean AOD at 500nm. The correlation has been calculated only in sites with available data for the entire annual cycle. Black dots indicate AERONET measurement sites. Correlation value is indicated by the size of the circles. The color of the circles indicates the dominant contribution to the total all-sky AOD: lime (organic carbon), black (black carbon), red (sulfate), dark-yellow (dust), and cyan (sea-salt). Bottom panel: normalized bias of simulated and AERONET monthly mean AOD at 500nm. AERONET values have been considered only in sites with at least 3 years of available data. Positive and negative symbols indicate the bias sign. Bias value is indicated by the size of the circles, from 0 to 100% and more. Model and AERONET monthly mean values have been averaged over the period 2002−2006

Table 14: Summary of model performance statistics and comparison with other studies. r, b, g, and RMSE stand for correlation, normalized bias, normalized gross error, and root mean square error of monthly mean values (averages over 2002−2006), respectively. Results are shown as total mean values (all) and for specific regions: United States (US), North America (NA), Europe (EU), East Asia (EA), and Africa (AF). Square brackets indicate minimum, median, and maximum values provided by AC-II. Curly brackets indicate values provided by SH13. Note that AC-II and SH13 (with the exception of 2 models of SH13) AOD statistics refer to all-sky AOD calculations.

surface concentrations					
parameter	region	r	b	g	RMSE
OC ($\mu g/m^3$)	US	0.76	+41.9%	58.3%	0.39
		$[0.25, 0.47, 0.56]$	$[-69.5\%, +22.0\%, +51.0\%]$	–	$[0.73, 1.08, 1.59]$
OC ($\mu g/m^3$)	EU	0.05	-63.9%	70.4%	3.92
		$[0.02, 0.12, 0.30]$	$[-77.5\%, -54.7\%, -20.0\%]$	–	$[3.32, 3.84, 4.20]$
EC ($\mu g/m^3$)	US	0.45	+92.9%	108.5%	0.22
EC ($\mu g/m^3$)	EU	0.32	-5.8%	60.9%	1.91
		$[-0.26, -0.23, 0.41]$	$[-99.4\%, -99.2\%, +7.7\%]$	–	$[0.89, 360.00, 369.00]$
SU ($\mu g(S)/m^3$)	US	0.84	+61.9%	73.0%	0.28
		$[0.58, 0.86, 0.90]$	$[-26.8\%, +8.0\%, +118.4\%]$	–	$[0.22, 0.33, 1.21]$
SU ($\mu g(S)/m^3$)	EU	0.49	+11.3%	46.7%	0.75
		$[0.12, 0.37, 0.60]$	$[-41.0\%, -11.3\%, +279.3\%]$	–	$[0.43, 0.59, 2.94]$
SU ($\mu g(S)/m^3$)	EA	0.50	+33.1%	65.6%	0.976
clear-sky AOD at 500nm vs AERONET					
AOD	all	0.69	+4.0%	38.3%	0.13
		$[0.30, 0.65, 0.78]$	$[-47.3\%, -10.9\%, +139.1\%]$	–	$[0.12, 0.15, 0.47]$
		$\{0.44, 0.56, 0.69\}$	$\{-22\%, -3.5\%, +77\%\}$	–	–
AOD	NA	0.72	+7.8%	34.5%	0.06
		$[-0.01, 0.64, 0.83]$	$[-57.8\%, -2.5\%, +210.0\%]$	–	$[0.05, 0.07, 0.38]$
AOD	EU	0.70	-12.8%	27.5%	0.07
		$[0.01, 0.47, 0.71]$	$[-48.7\%, +9.2\%, +270.1\%]$	–	$[0.06, 0.09, 0.67]$
AOD	EA	0.46	-21.1%	45.4%	0.25
		$[0.27, 0.63, 0.73]$	$[-73.7\%, -35.0\%, +63.2\%]$	–	$[0.17, 0.25, 0.48]$
AOD	AF	0.73	+14.2%	36.0%	0.21
		$[0.54, 0.74, 0.80]^*$	$[-47.1\%, -11.5\%, +107.8\%]^*$	–	$[0.13, 0.15, 0.36]^*$
clear-sky AOD at 550nm vs MODIS					
AOD	all	0.59	-0.2%	24.1%	0.21
		$\{0.46, 0.55, 0.64\}$	$\{-28\%, -5.5\%, +54\%\}$	–	–
clear-sky AOD at 550nm vs MISR					
AOD	all	0.52	-9.4%	21.3%	0.05
		$\{0.49, 0.60, 0.67\}$	$\{-30\%, -9\%, +48\%\}$	–	–

Chapter 5 – Conclusions

Organic aerosols from tree emissions. Photo credits: pnnl.gov

5 Conclusions

In the previous Chapters we have described the development and the evaluation of a new aerosol module for the NMMB/BSC-CTM model. In particular, the objectives introduced in Section 1.2 have been achieved. They can be resumed in three main points:

i. An aerosol module designed to provide short and medium range forecast of aerosols has been implemented within the multiscale NMMB/BSC-CTM model. Sea-salt, organic aerosol (both primary and secondary), black carbon, and sulfate have been included, extending the BSC-Dust model.

ii. The aerosol module has been evaluated at global scale by comparing it with several observational datasets. Regional simulations of the sea-salt transport at coastal/orographic sites have been additionally performed to study the sensitivity to the model resolution.

iii. A 5-year simulation of the global distribution of sea-salt, carbonaceous and sulfate aerosols has been discussed. All-sky and clear-sky calculations of the total AOD (including the mineral dust contribution) have been also presented and discussed.

In the following we detail the specific conclusions achieved in each work:

Section 3.1.
In this Section we presented global simulations of the sea-salt aerosol global distribution with the multiscale model NMMB/BSC-CTM. Since the main uncertainties in sea-salt modeling are related to the parameterization of emissions, we implemented five different sea-salt emission schemes and analyzed their performance. We compared global simulations covering the period 2002–2006 with climatologies from the University of Miami Network and "sea-salt-dominated" stations from the AERONET sun photometer network. For the comparison with AERONET, we used the coarse fraction of the AOD.

1) We found a strong sensitivity of sea-salt aerosol lifetime to the emission scheme, ranging from 7.3 h to 11.3 h. The use of SST-dependent emission schemes produces an enhancement of the sea-salt lifetime, which increases from 7.3 h with Gong (2003) (G03) to 9.6 h with Jaeglé et al. (2011) (J11) and from 8.9 h with the combined Monahan et al. (1986)/Smith et al. (1993) (M86/SM93) to 10.4 h with the combined Mårtensson et al. (2003)/Monahan et al. (1986)/Smith et al. (1993) (MA03/M86/SM93).

2) The SST latitudinal modulation with J11 and MA03/M86/SM93 also leads to marked differences in the global patterns of surface concentration and AOD compared with M86, M86/SM93, and G03. In particular, maximum AOD values are reached at high latitudes with M86, M86/SM93, and G03, and in the tropics with J11 and MA03/M86/SM93.

3) SST-dependent emission schemes lead to a clear improvement of the simulated surface concentration, with a significant reduction of bias and gross error. In particular, J11 shows the best agreement with observations. However, the simulated coarse AOD with J11 and MA03/M86/SM93 is affected by positive biases at several AERONET sites located in the tropics. Factors that may explain the AOD overestimation include the use of all-sky model AOD in the comparison and the treatment of the water uptake, deposition, and optical properties in the model. Further research may aim at investigating SST effects upon particle size distribution.

4) As in previous studies, the model shows a strong overestimation in sites characterized by steep topography (e.g. Invercargill in New Zealand and Marion Island), independently from the applied emission scheme.

Section 3.2.
Following conclusion 4) of Section 3.1, we investigated the influence of model resolution on the simulation of sea-salt aerosol trends at global evaluation stations located in regions characterized by strong orographic gradients and/or complex sea/land interfaces. We selected four stations from the Univerisity of Miami Network where different global models presented significant errors when compared with sea-salt surface concentration climatologies.

5) We showed that an increase of model resolution from 1°x1.4° to 0.1°x0.1° without changing any model scheme resulted in a strong bias reduction from +63.7% to 3.3% and an increase in the overall correlation from 0.52 to 0.84. The improvement of model results may be related to a better reproduction of sea/land interfaces and the characterization of mesoscale circulations and precipitation. We note that model experiments at 0.5° and 0.25° (not reported here) did not show improvements with respect to the experiments at 1°x1.4°. Resolutions of at least 0.1° are needed to reproduce the observations at these sites.

6) Our results suggest that caution may be taken when evaluating and/or constraining sea-salt global models with measurements from sites affected by coastal/orographic effects. Systematic errors in these sites due to the use of coarse resolution in global models can strongly affect the interpretation of model results that compare sea-salt source functions of the open ocean.

Chapter 4.
In this Section we have presented the development of a new aerosol module, which is online integrated within the NMMB/BSC-CTM model. Organic aerosol (both primary and secondary), black carbon, and sulfate were introduced in the new system in addition to dust and sea-salt, that were already developed and evaluated in the works of Pérez et al. (2011) and Spada et al. (2013) (Chapter 3 of the present thesis), respectively. Due to its online implementation within the meterological core, the module benefits of the main features of the multiscale NMMB model and it is able to simulate from global to local scales and is designed to provide short-medium range forecast for a wide range of applications.
We performed a model evaluation at global scale by comparing with several worldwide datasets of monthly mean measurements, both for aerosol surface concentrations and AOD. In this study, we do not consider the direct radiative effect of aerosols, and we applied standardized emissions from the AEROCOM-ACCMIP inventory to produce a basic benchmark for future developments.

7) We found an overall good agreement of the simulated concentrations with observations, especially the organic carbon concentrations measured in US which are reproduced with a very high correlation (0.76), comparable to other state-of-the-art models. Since in this region the biogenic SOA are playing a very relevant role, we attribute this feature to the abilty of the implemented two-product scheme of Tsigaridis and Kanakidou (2007). Despite this achievement, it is clear that we are missing relevant organic aerosol sources in specific marine stations, sources that could be associated to marine (primary) and anthropogenic organic aerosol production (Karl et al., 2009; Tsigaridis et al., 2014) which are not considered in this work.

8) In agreement with the aerosol modeling community, we found that the simulation of black carbon is still affected by strong uncertainties (mainly related with the emission estimates and the modeling of removal processes), greater than for the other species considered in this work.

9) The scores in the simulation of sulfate concentration lie in the higher part of the AEROCOM (AEROCOM-II experiment, specifically the CTRL simulations of the year 2006 as reported in the AEROCOM web: `http://aerocom.met.no/cgi-bin/AEROCOM/aerocom/surfobs_annualrs.pl`, last check: 18/05/2015) models. Our results also suggest that the use of a higher resolution could be required in regions characterized by steep orography and transport of low concentrations (such as in the mountainous regions of the Western US). At marine stations, the sulfate production driven by DMS emissions is overestimated by the model during the boreal summer, probably due to overestimates in the DMS emission flux used in this work. The overestimates in the off-line oxidant fields (OH, O_3) during the boreal summer may also play a role. These key points in the simulation of the sulfur chemistry should be investigated in the future.

10) The clear-sky AOD simulated by the model (including the contribution of all the aerosol components) shows a good agreement with both AERONET and satellite observations. The overall correlation with AERONET (0.69) lies in the higher part of the results obtained by the AEROCOM (AEROCOM-II) [0.30 − 0.78] and ACCMIP (Shindell et al., 2013) [0.44 − 0.69] models. The comparison with AERONET and satellites indicates that the model tends to overestimate the AOD over desert dust sources and to overestimate AOD over regions affected by fires. The first problem can be attributed to the overestimates in the size distribution assumed for the emitted dust particles (Pérez et al., 2011). The latter problem can be related with the estimates of biomass-burning emissions, which are still an open issue and characterized by strong uncertainties (up to a factor of 4) (Kaiser et al., 2012). Further investigations on these two key points are mandatory to improve the simulation of the AOD.

11) The model underestimation of AOD in the Eastern Asia can be related with the absence of other aerosol species that are neglected by this model version (such as nitrate, that can contribute with AOD annual mean values up to 0.1 as found by Hauglustaine et al. (2014)) on the total AOD. The implementation of nitrate aerosol and its chemical feedbacks with sulfate is currently under development.

Way Forward.

We conclude this document with a list of suggestions for future investigations with the NMMB/BSC-CTM aerosol module.

As suggested by conclusions 3), investigations on the dependence on particle size have to be planned to properly include the SST-dependence in sea-salt emission schemes.

As suggested by conclusions 5) and 6), higher spatial resolution may be required to improve the overall understanding of the global aerosols. Currently we are planning 0.1°x0.1° simulations of the aerosol transport over the globe by taking advantage of the improved computational efficiency of the new MareNostrum-III machine hosted by the Barcelona Supercomputing Center.

As evidenced by conclusion 7), online sources of primary marine organic aerosol production should be explored in order to improve the simulation of organic aerosol at marine regions.

As suggested by conclusion 9), a specific study of the DMS emission and chemistry has to be planned to improve the model ability in the simulation of sulfate formation in marine environments. For example, in our modeling system, online DMS emissions could be calculated by triggering the iron deposition (driven by the mineral dust transport) over oceans. In this sense, the implementation of a dust mineralogy (Nickovic et al., 2013; Perlwitz et al., 2015) could also lead to a model improvement in the simulation of DMS.

As reported in conclusion 10), an improvement of the mineral dust distribution at emission is required. This issue is currently under investigation and a model upgrade is planned in the near future.

Due to uncertainties characterizing their estimates (highlighted in conclusion 10)), a study focused on the biomass-burning emissions (both emission fluxes and vertical distribution) is also planned. The use of the satellite estimates provided by the IS4FIRES could represent a very useful tool in this study.

As suggested by conclusion 11), the inclusion of ammonium/nitrate aerosol (and their coupling with the sulfur chemistry) in the module could be necessary for an accurate simulation of the total AOD in specific regions. The modeling of ammonium/nitrate aerosol is currently under development (although not presented in this work).

Although in this thesis we focused on the global scale, due to the coupling with the multiscale NMMB, the model is also designed to provide regional simulation of the aerosol transport (as stated in Section 1.2). As suggested by conclusion 9), a study focused on the use of the fully online-coupled gas/aerosol chemistry will be necessary.
Preliminary investigations (not shown here) also indicate that the inclusion of additional channels of SOA production (currently the module only account for biogenic precursors) could be a key point in the simulation of regions affected by anthropogenic emissions.
Note that, in order to perform operational forecasts, the module has also to be coupled with near-real time emission of fires.

A module evaluation with vertical distributed observations is planned. This evaluation is crucial to better understand the critical uncertainties related with the aerosol transport, such as for example those affecting the transport of black carbon particles towards the Arctic region and those affecting the parameterization of the wet deposition of particles.

The module simulation of the aerosol direct radiative effect is currently under investigation.

All the simulations were performed on the MareNostrum machine hosted by the Barcelona Supercomputing Center.

References

Aan de Brugh, J. M. J., Schaap, M., Vignati, E., Dentener, F., Kahnert, M., Sofiev, M., Huijnen, V., and Krol, M. C.: The European aerosol budget in 2006, Atmos. Chem. Phys., 11, 1117–1139, doi:10.5194/acp-11-1117-2011, 2011.

Abdul-Razzak, H. and Ghan, S. J.: A parameterization of aerosol activation 2. Multiple aerosol types, J. Geophys. Res., 105 (D5), 6837–6844, 2000.

Aiken, A. C., Decarlo, P. F., Kroll, J. H., Worsnop, D. R., Huffman, J. A., Docherty, K. S., Ulbrich, I. M., Mohr, C., Kimmel, J. R., Sueper, D., Sun, Y., Zhang, Q., Trimborn, A., Northway, M., Ziemann, P. J., Canagaratna, M. R., Onasch, T. B., Alfarra, M. R., Prevot, A. S. H., Dommen, J., Duplissy, J., Metzger, A., Baltensperger, U., and Jimenez, J. L.: O/C and OM/OC ratios of primary, secondary, and ambient organic aerosols with high-resolution time-of-flight aerosol mass spectrometry, Environ. Sci. Technol., 42, 4478–4485, doi:10.1021/es703009q, 2008.

Andreas, E. L.: A new sea spray generation functions for wind speeds up to $32\,\mathrm{m\,s^{-1}}$, J. Phys. Oceanogr., 28, 2175–2184, 1998.

Badia, A.: Implementation, development and evaluation of the gas-phase chemistry within the Global/Regional NMMB/BSC Chemical Transport Model (NMMB/BSC-CTM), PhD Thesis, B 5569-2015, Institut de Sostenibilitat – Universitat Politècnica de Catalunya (UPC), `http://www.tdx.cat/handle/10803/284886`, 2014.

Badia, A. and Jorba, O.: Gas-phase evaluation of the online NMMB/BSC-CTM model over Europe for 2010 in the framework of the AQMEII-Phase2 project, Atmos. Env., 115, 657–669, doi:10.1016/j.atmosenv.2014.05.055, 2015.

Balkanski, Y.: L'influence des aérosols sur le climat, Thèse d'habilitation à diriger des recherches, Université Versailles Saint Quentin, St Quentin en Yvelines, 2011.

Barth, M. C., Rasch, P. J., and Kiehl, J. T.: Sulfur chemistry in the National Center for Atmospheric Research Community Climate Model: Description, evaluation, features, and sensitivity yo aqueous chemistry, J. Geophys. Res., 105 (D1), 1387–1415, 2000.

Bauer, S. E., Wright, D. L., Koch, D., Lewis, E. R., Mc-Graw, R., Chang, L.-S., Schwartz, S. E., and Ruedy, R.: MATRIX (Multiconfiguration Aerosol TRacker of mIXing state): an aerosol microphysical module for global atmospheric models, Atmos. Chem. Phys., 8, 6003–6035, doi:10.5194/acp-8-6003-2008, 2008.

Beard, K. V.: Terminal velocity and shape of cloud and precipitation drops aloft, J. Atmos. Sci., 33, 851–864, 1976.

Bellouin, N., Rae, J., Jones, A., Johnson, C., Haywood, J., and Boucher, O.: Aerosol forcing in the Climate Model Intercomparison Project (CMIP5) simulations by HadGEM2-ES and the role of ammonium nitrate, J. Geophys. Res.-Atmos., 116, D20206, doi:10.1029/2011jd016074, 2011.

Benedetti, A., Morcrette, J. J., Boucher, O., Dethof, A., Engelen, R. J., Fisher, M., Flentje, H., Huneeus, N., Jones, L., Kaiser, J. W., Kinne, S., Mangold, A., Razinger, M., Simmons,

A. J., and Suttie, M.: Aerosol analysis and forecast in the European Centre for Medium-Range Weather Forecasts Integrated Forecast System: 2. Data assimilation, J. Geophys. Res.-Atmos., 114, D13205, doi:10.1029/2008jd011115, 2009.

Bessagnet, B., Hodzic, A., Vautard, R., Beekmann, M., Cheinet, S., Honoré, C., Liousse, C., and Rouil, L.: Aerosol modeling with CHIMERE - preliminary evaluation at the continental scale, Atmos. Env., 38, 2803–2817, 2004.

Bessagnet B., Menut, L., Curci, G., Hodzic, A., Guillaume, B., Liousse, C., Moukhtar, S., Pun, B., Seigneur, C., and Schulz, M.: Regional modelling of carbonaceous aerosols over Europe - Focus on Secondary Organic Aerosols, J. Atmos. Chem., 61, 175–202, 2009.

Betts, A. K.: A new convective adjustment scheme, Part I: Observational and theoretical basis., Q. J. Roy. Meteor. Soc., 112, 677–691, 1986.

Betts, A. K., and Miller, M. J.: A new convective adjustment scheme, Part II: Single column tests using GATE wave, BOMEX, ATEX and Artic air-mass data sets, Q. J. Roy. Meteor. Soc., 112, 693–709, 1986.

Binkowski, F. S. and Roselle, S. J.: Models-3 Community Multiscale Air Quality (CMAQ) model aerosol component 1. Model description, J. Geophys. Res., 108, D6, 4183, doi:10.1029/2001JD001409, 2003.

Bormann, N. and Marks, C. J.: Mesoscale Rainfall Forecasts over New Zealand during SALPEX96: Characterization and Sensitivity Studies, Mon. Weather Rev., 127, 2880–2893, doi:10.1175/1520-0493(1999)127<2880:MRFONZ>2.0.CO;2, 1999.

Byun, D., and Ching, J.: Science algorithms of the EPA Models-3 community multiscale air quality (CMAQ) modeling system, US Environmental Protection Agency, Office of Research and Development Washington, DC.

Caffrey, P. F., Hoppel, W. A., and Shi, J. J.: A one-dimensional sectional aerosol model integrated with mesoscale meteorological data to study marine boundary layer aerosol dynamics, J. Geophys. Res., 111, D24201, doi:10.1029/2006JD007237, 2006.

Cavalli, F., Viana, M., Yttri, K. E., Genberg, J., and Putaud, J.-P.: Toward a standardised thermal-optical protocol for measuring atmospheric organic and elemental carbon: the EUSAAR protocol, Atmos. Meas. Tech., 3, 79–89, doi:10.5194/amt-3-79-2010, 2010.

Chameides, W. L.: The photochemistry of a remote marine stratiform cloud, J. Geophys. Res., 89D, 4739–4755, 1984.

Chapman, E. G., Gustafson Jr., W. I., Easter, R. C., Barnard, J. C., Ghan, S. J., Pekour, M. S., and Fast, J. D.: Coupling aerosol-cloud-radiative processes in the WRF-Chem model: Investigating the radiative impact of elevated point sources, Atmos. Chem. Phys., 9, 945–964, doi:10.5194/acp-9-945-2009, 2009.

Chin, M., Rood, R. B., Lin, S. J., Mller, J. F., and Thompson, A. M.: Atmospheric sulfur cycle simulated in the global model GOCART: Model description and global properties, J. Geophys. Res.-Atmos., 105, 24671–24687, doi:10.1029/2000jd900384, 2000.

Chin, M., Ginoux, P., Kinne, S., Torres, O., Holben, B. N., Duncan, B. N., Martin, R. V., Logan, J. A., Higurashi, A., and Nakajima, T.: Tropospheric aerosol optical thickness from the GOCART model and comparisons with satellite and sun photometer measurements, J. Atmos. Sci., 59, 461–483, 2002.

Christensen, L. E., Okumura, M., Sander, S. P., Salawitch, R. J., Toon, G. C., Sen, B., Blavier, J.-F., and Jucks, K. W.: Kinetics of HO2 + HO2 → H2O2 + O2: Implications for stratospheric H2O2, Geophys. Res. Lett., 29, doi:10.1029/2001GL014525, 2002.

Chylek, P., Damiano, P., Kalyaniwalla, N., and Shettle, E. P.: Radiative properties of water clouds: Simple approximations, Atmos. Res., 35, 139–156, 1995.

Clarke, A. D., Owens, S. R., and Zhou, J.: An ultrafine sea-salt flux from breaking waves: implications for cloud condensation nuclei in the remote marine atmosphere, J. Geophys. Res., 111, D06202, doi:10.1029/2005JD006565, 2006.

Cooke, W. F. and Wilson, J. J. N.: A global black carbon aerosol model, J. Geophys. Res., 101, 19395–19409, 1996.

Croft, B., Lohmann, U., Martin, R. V., Stier, P., Wurzler, S., Feichter, J., Hoose, C., Heikkilä, U., Van Donkelaar, A., and Ferrachat, S.: Influences of in-cloud aerosol scavenging parameterizations on aerosol concentrations and wet deposition in ECHAM5-HAM, Atmos. Chem. Phys., 10, 1511–1543, 2010.

D'Almeida, G. A.: On the variability of desert aerosol radiative characteristics, J. Geophys. Res., 92, 3017–3026, doi:10.1029/JD092iD03p03017, 1987.

D'Almeida, G. A.: Atmospheric Aerosols, Deepak Publishing, Hampton, Virginia, 561 pp., 1991.

DeBell, L. J., Gebhart, K. A., Hand, J. L., Malm, W. C., Pitchford, M. L., Schichtel, B. A., and White, W. H.: Spatial and seasonal patterns and temporal variability of haze and its constituents in the United States Report IV, Cooperative Institute for Research in the Atmosphere, 217–218, 2006.

Dentener, F., Kinne, S., Bond, T., Boucher, O., Cofala, J., Generoso, S., Ginoux, P., Gong, S., Hoelzemann, J. J., Ito, A., Marelli, L., Penner, J. E., Putaud, J.-P., Textor, C., Schulz, M., van der Werf, G. R., and Wilson, J.: Emissions of primary aerosol and precursor gases in the years 2000 and 1750 prescribed data-sets for AeroCom, Atmos. Chem. Phys., 6, 4321–4344, doi:10.5194/acp-6-4321-2006, 2006.

de Leeuw, G., Neele, F. P., Hill, M., Smith, M. H., and Vignati, E.: Production of sea spray aerosol in the surf zone, J. Geophys. Res., 105, 29397–29409, 2000.

de Leeuw, G., Andreas, E. L., Anguelova, M. D., Fairall, C. W., Lewis, E. R., O'Dowd, C., Schulz, M., and Schwartz, S. E.: Production flux of sea spray aerosol, Rev. Geophys, 49, RG2001, doi:1029/2010RG000349, 2011.

Downing, H. D. and Williams, D.: Optical-constants of water in infrared, J. Geophys. Res., 80, 1656–1661, 1975.

Emmons, L. K., Walters, S., Hess, P. G., Lamarque, J.-F., Pfister, G. G., Fillmore, D., Granier, C., Guenther, A., Kinnison, D., Laepple, T., Orlando, J., Tie, X., Tyndall, G., Wiedinmyer, C., Baughcum, S. L., and Kloster, S.: Description and evaluation of the Model for Ozone and Related chemical Tracers, version 4 (MOZART-4), Geosci. Model Dev., 3, 43–67, doi:10.5194/gmd-3-43-2010, 2010.

Fan, T. and Toon, O. B.: Modeling sea-salt aerosol in a coupled climate and sectional microphysical model: mass, optical depth and number concentration, Atmos. Chem. Phys., 11, 4587–4610, doi:10.5194/acp-11-4587-2011, 2011.

Farina, S. C., Adams, P. J., and Pandis, S. N.: Modeling global secondary organic aerosol formation and processing with the volatility basis set: Implications for anthropogenic secondary organic aerosol, J. Geophys. Res.-Atmos., 115, D09202, doi:10.1029/2009jd013046, 2010.

Fels, S. B. and Schwarzkopf, M. D.: The simplified exchange approximation: a new method for radiative transfer calculations, J. Atmos. Sci., 32, 1475–1488, 1975.

Ferrier, B. S., Jin, Y., Lin, Y., Black, T., Rogers, E., and DiMego, G.: Implementation of a new frid-scale cloud and precipitation shceme in the NCEP Eta Model, in: Proc. 15th Conf. on Numerical Weather Prediction, San Antonio, 12–16 August 2002, TX, American Meteorological Society, 280–283, 2002.

Foley, K. M., Roselle, S. J., Appel, K. W., Bhave, P. V., Pleim, J. E., Otte, T. L., Mathur, R., Sarwar, G., Young, J. O., Gilliam, R. C., Nolte, C. G., Kelly, J. T., Gilliland, A. B., and Bash, J. O.: Incremental testing of the Community Multiscale Air Quality (CMAQ) modeling system version 4.7, Geosci. Model Dev., 3, 205–226, doi:10.5194/gmd-3-205-2010, 2010.

Fontoukis, C., and Nenes, A.: ISORROPIA II: A computationally efficient thermodynamic equilibrium model for K^+-Ca^{2+}-Mg^{2+}-NH^+-Na^+-SO_4^{2-}-NO_3^--Cl^--H_2O aerosols, Atmos. Chem. Phys., 7 (17), 4639–4659, doi:, 2007.

Fuchs, N. A.: The mechanics of Aerosols, Pergamon Press, New York, 1964.

Gerber, H.: Relative-humidity parameterization of the navy aerosol model (NAM), Tech. rep., Tech. Rep. 8956, National Research Laboratory, Washington DC, 1985.

Ghan, S. J., Chuang, C. C., and Penner, J. E.: A parameterization of cloud droplet nucleation, Part I, Single aerosol species, Atmos. Res., 30, 197–222, 1993.

Ghan, S. J., Laulainen, N., Easter, R. C., Wagener, R., Nemesure, S., Chapman, E., and Leung, Y. Z. R.: Evaluation of aerosol direct radiative forcing in MIRAGE, J. Geophys. Res., 106, 5295–5316, 2001.

Ginoux, P., Chin, M., Tegen, I., Prospero, J. M., Holben, B., Dubovik, O., and Lin, S. J.: Sources and distributions of dust aerosols simulated with the GOCART model, J. Geophys. Res.-Atmos., 106, 20255–20273, doi:10.1029/2000jd000053, 2001.

Grythe, H., Ström, J., Krejci, R., Quinn, P., and Stohl, A.: A review of sea spray aerosol source functions using a large global set of sea salt aerosol concentration measurements, Atmos. Chem. Phys. Discuss., 13, 20729–20781, doi:10.5194/acpd-13-20729-2013, 2013.

Gong, S. L.: A parameterization of sea-salt aerosol source function for sub and super-micron particles, Global Biogeochem. Cy., 17, 1097, doi:10.1029/2003GB002079, 2003.

Gong, S. L., Lavoué, D., Zhao, T. L., Huang, P., and Kaminski, J. W.: GEM-AQ/EC, an on-line global multi-scale chemical weather modelling system: model development and evaluation of global aerosol climatology, Atmos. Chem. Phys., 12, 8237–8256, doi:10.5194/acp-12-8237-2012, 2012.

Haustein, K., Pérez, C., Baldasano, J. M., Jorba, O., Basart, S., Miller, R. L., Janjic, Z., Black, T., Nickovic, S., Todd, M. C., Washington, R., Müller, D., Tesche, M., Weinzierl, B., Esselborn, M., and Schladitz, A.: Atmospheric dust modeling from meso to global scales with the online NMMB/BSC-Dust model – Part 2: Experimental campaigns in Northern Africa, Atmos. Chem. Phys., 12, 2933–2958, doi:10.5194/acp-12-2933-2012, 2012.

Goto, D., Nakajima, T., Takemura, T., and Sudo, K.: A study of uncertainties in the sulfate distribution and its radiative forcing associated with sulfur chemistry in a global aerosol model, Atmos. Chem. Phys., 11, 10889–10910, doi:10.5194/acp-11-10889-2011, 2011.

Grell, G., Peckham, S., Schmitz, R., McKeen, S., Frost, G., Skamarock, W. C., and Eder, B.: Fully coupled online chemistry within the WRF model, Atmos. Env., 39 (37), 6957–6975, 2005.

uenther, A., Karl, T., Harley, P., Wiedinmyer, C., Palmer, P. I., and Geron, C.: Estimates of global terrestrial isoprene emissions using MEGAN (Model of Emissions of Gases and Aerosols from Nature), Atmos. Chem. Phys., 6, 3181–3210, doi:10.5194/acp-6-3181-2006, 2006.

Hauglustaine, D. A., Balkanski, Y., and Schulz, M.: A global model simulation of present and future nitrate aerosols and their direct radiative forcing of climate, Atmos. Chem. Phys., 14, 11031–11063, doi:10.5194/acp-14-11031-2014, 2014.

Henze, D. K. and Seinfeld, J. H.: Global secondary organic aerosol from isoprene oxidation. Geophys. Res. Lett., 33, L09812, 2006.

Hess, M., Koepke, P., and Schult, I.: Optical properties of aerosols and clouds: The software package OPAC, Bulletin of the American Meteorological Society, 79, 831–844, 1998.

Hoffmann, M. R.: On the kinetics and mechanism of oxidation of aquated sulfur dioxide by ozone, Atmos. Environ., 20, 1145–1154, 1986.

Holben, B. N., Eck, T. F., Slutsker, I., Tanré, D., Buis, J. P., Setzer, A., Vermote, E., Reagan, J. A., Kaufman, Y., Nakajima, T., Lavenu, F., Jankowiak, I., and Smirnov, A.: AERONET – a federated instrument network and data archive for aerosol characterization, Remote Sens. Environ., 66, 1–16, 1998.

Hoose, C., Lohmann, U., Bennartz, R., Croft, B., Lesins, G.: Global simulations of aerosol processing in clouds, Atmos. Chem. Phys., 8, 6939-6963, 2008.

Hoose, C., Lohmann, U., Stier, P., Verheggen, B., and Weingartner, E.: Aerosol processing in mixedphase clouds in ECHAM5HAM: Model description and comparison to observations, J. Geophys. Res., 113, D07210, 2008.

Hoppel, W. A., Frick, G. M., and Fitzgerald, J. W.: Surface source function for sea-salt aerosol and aerosol dry deposition to the ocean surface, J. Geophys. Res., 107, 4382, doi:10.1029/2001JD002014, 2002.

Hoyle, C. R., Berntsen, T., Myhre, G., and Isaksen, I. S. A.: Secondary organic aerosol in the global aerosol – chemical transport model Oslo CTM2, Atmos. Chem. Phys., 7, 5675–5694, doi:10.5194/acp-7-5675-2007, 2007.

Hoyle, C. R., Myhre, G., Berntsen, T. K., and Isaksen, I. S. A.: Anthropogenic influence on SOA and the resulting radiative forcing, Atmos. Chem. Phys., 9, 2715–2728, doi:10.5194/acp-9-2715-2009, 2009.

Hoyle, C. R., Boy, M., Donahue, N. M., Fry, J. L., Glasius, M., Guenther, A., Hallar, A. G., Huff Hartz, K., Petters, M. D., Petäjä, T., Rosenoern, T., and Sullivan, A. P.: A review of the anthropogenic influence on biogenic secondary organic aerosol, Atmos. Chem. Phys., 11, 321–343, doi:10.5194/acp-11-321-2011, 2011.

Hsu, S. A., Meindl, E. A., and Gilhousen, D. B.: Determining the power law wind-profile exponent under near-neutral stability conditions at sea, Appl. Meteorol., 33, 757–765, doi:10.1175/1520-0450(1994)033<0757:DTPLWP>2.0.CO;2, 1994.

Huijnen, V., Williams, J., van Weele, M., van Noije, T., Krol, M., Dentener, F., Segers, A., Houweling, S., Peters, W., de Laat, J., Boersma, F., Bergamaschi, P., van Velthoven, P., Le Sager, P., Eskes, H., Alkemade, F., Scheele, R., Nédélec, P., and Pätz, H.-W.: The global chemistry transport model TM5: description and evaluation of the tropospheric chemistry version 3.0, Geosci. Model Dev., 3, 445–473, doi:10.5194/gmd-3-445-2010, 2010.

Hyvärinen, A.-P., Kolmonen, P., Kerminen, V.-M., Virkkula, A., Leskinen, A, Komppula, M., Hatakka, J., Burkhart, J., Stohl, A., Aalto, P., Kulmala, M., Lehtinen, K. E. J., Viisanen, Y., and Lihavainen, H.: Aerosol black carbon at five background measurement sites over Finland, a gateway to the Arctic, Atmos. Env., 45, 24, 4042–4050, doi:10.1016/j.atmosenv.2011.04.026, 2011.

IPCC: Climate change 2013: The physical science basis: Working Group I Contribution to the Fifth Assessment Report of the Intergovernmental Panel on Climate Change, Cambridge University Press, Cambridge and New York, 2013.

Jacobson, M. Z.: Studying the effects of calcium and magnesium on size-distributed nitrate and ammonium with EQUISOLV II, Atmos. Env., 33, 3635–3649, 1999.

Jaeglé, L., Quinn, P. K., Bates, T. S., Alexander, B., and Lin, J.-T.: Global distribution of sea salt aerosols: new constraints from in situ and remote sensing observations, Atmos. Chem. Phys., 11, 3137–3157, doi:10.5194/acp-11-3137-2011, 2011.

Janjic, Z. I.: Pressure gradient force and advection scheme used for forecasting with steep and small scale topography, Contributes to Atmospheric Physics, 150, 186–199, 1977.

Janjic, Z. I.: Forward-backward scheme modified to prevent two-grid interval noise and its application in sigma coordinate models, Contributes to Atmospheric Physics, 52, 69–84, 1979.

Janjic, Z. I.: Non-linear advection schemes and energy cascade on semi-staggered grids, Mon. Weather Rev., 112, 1234–1245, 1984.

Janjic, Z. I.: The step-mountain eta coordinate model: physical package, Mon. Weather Rev., 118, 1429–1443, 1990.

Janjic, Z. I.: The step-mountain eta coordinate model: further developments of the convection, viscous sublayer, and turbulence closure schemes, Mon. Weather Rev., 122, 927–945, 1994.

Janjic, Z. I.: The surface layer in the NCEP eta model, 11th Conference on Numerical Weather Prediction, Norfolk, VA, 19–23 August 1996; American Meteorological Society, Boston, MA, 354–355, 1996.

Janjic, Z. I.: Comments on "Development and evaluation of a convection scheme for use in climate models", J. Atmos. Sci., 57, 3686–3686, doi:10.1175/1520-0469(2000)057<3686:CODAEO>2.0.CO;2, 2000.

Janjic, Z. I.: Nonsingular implementation of the Mellor-Yamada Level 2.5 Scheme in the NCEP Meso model, Tech. rep., NOAA/NWS/NCEP Office Note No. 436, 61 pp., avalaible at: `http://www.emc.ncep.noaa.gov/officenotes/newernotes/on437.pdf` (last access: December 2012), 2001.

Janjic, Z. I.: A nonhydrostatic model based on a new approach, Meteorol. Atmos. Phys., 82, 271–285, doi:10.1007/s00703-001-0587-6, 2003.

Janjic, Z. I.: A unified model approach from meso to global scales, Geophys. Res. Abs., 7, SRef–ID: 1607–7962/gra/EGU05–A–05 582, 2005.

Janjic, Z. I. and Black, T.: A unified model approach from meso to global scales, Geophys, Res, Abs,, 7, SRef–ID: 1607–7962/gra/EGU2007–A–05 025, 2007.

Janjic, Z.: Further development of the unified multiscale Eulerian model for a broad range of spatial and temporal scales within the new National Environmental Modeling System, EGU General Assembly 2009, held 19–24 April 2009, Wien, Austria, abstract EGU2009-1587, 11, 1587 pp., 2009.

Janjic, Z. I. and Gall, R.: Scientific documentation of the NCEP nonhydrostatic multiscale model on the B grid (NMMB), Part 1 Dynamics, Tech. rep., NCAR/TN-489+STR, doi:10.5065/D6WH2MZX, availabe at: `http://nldr.library.ucar.edu/repository/collections/TECH-NOTE-000-000-000-857` (last access: December 2012), 2012.

Janjic, Z. I., Gerrity, J. P., and Nickovic, S.: An alternative approach to nonhydrostatic modeling, Mon. Weather Rev., 129, 1164–1178, doi:10.1175/1520-0493(2001)129<1164:AAATNM>2.0.CO;2, 2001.

Janjic, Z. I., Janjic, T., and Vasic, R.: A class of conservative fourth order advection schemes and impact of enhanced formal accuracy on extended range forecasts, Mon. Weather Rev., 139, 1556–1568, doi:10.1175/2010MWR3448.1, 2011.

Jathar, S. H., Farina, S. C., Robinson, A. L., and Adams, P. J.: The influence of semi-volatile and reactive primary emissions: on the abundance and properties of global organic aerosol, Atmos. Chem. Phys., 11, 7727–7746, doi:10.5194/acp-11-7727-2011, 2011.

Jimenez, J. L., Canagaratna, M. R., Donahue, N. M., Prevot, A. S. H., Zhang, Q., Kroll, J. H., DeCarlo, P. F., Allan, J. D., Coe, H., Ng, N. L., Aiken, A. C., Docherty, K. S., Ulbrich, K. S., Grieshop, A. P., Robinson, A. L., Duplissy, J., Smith, J. D., Wilson, K. R., Lanz, V. A., Hueglin, C., Sun, Y. L., Tian, J., Laaksonen, A., Raatikainen, T., Rautiainen, J., Vaattovaara, P., Ehn, M., Kulmala, M., Tomlison, J. M., Collins, D. R., Cubison, M. J., Dunlea, E. J., Huffman, J. A., Onasch, T. B., Alfarra, M. R., Williams, P. I., Bower, K., Kondo, Y., Schneider, J., Drewnick, F., Borrmann, S., Weimer, S., Demerjian, K., Salcedo, D., Cottrell, L., Griffin, R., Takami, A., Miyoshi, T., Hatakeyama, S., Shimono, A., Sun, J. Y., Zhang, Y. M., Dzepina, K., Kimmel, J. R., Sueper, D., Jayne, J. T., Herndon, S. C., Trimborn, A. M., Williams, L. R., Wood, E. C., Middlebrook, A. M., Kolb, C. E., Baltensperger, U., and Worsnop, D. R.: Evolution of Organic Aerosols in the Atmosphere, Science, 326, 1525, doi:10.1126/science.1180353, 2009.

Johnson, B. J., Betterton, E. A., and Craig, D.: Henry's law coefficients of formic and acetic acids, J. Atmos. Chem., 24, 113–119, 1996.

Jorba, O., Dabdub, D., Blaszczak-Boxe, C., Pérez, C., Janjic, Z., Baldasano, J. M., Spada, M., Badia, A., and Gonçalves, M.: Potential significance of photoexcited NO2 on global air quality with the NMMB/BSC chemical transport model, J. Geophys. Res., 117, D13301, doi:10.1029/2012JD017730, 2012.

Kahn, R. A., Gaitley, B. J., Martonchik, J. V., Diner, D. J., Crean, K. A., and Holben, B.: Multiangle Imaging Spectroradiometer (MISR) global aerosol optical depth validation based on 2 years of coincident Aerosol Robotic Network (AERONET) observations, J. Geophys. Res., 110, D10S04, doi:10.1029/2004JD004706, 2005.

Kaiser, J. W., Heil, A., Andreae, M. O., Benedetti, A., Chubarova, N., Jones, L., Morcrette, J.-J., Razinger, M., Schultz, M. G., Suttie, M., and van der Werf, G. R.: Biomass burning emissions estimated with a global fire assimilation system based on observed fire radiative power, Biogeosciences, 9, 527–554, doi:10.5194/bg-9-527-2012, 2012.

Kalnay, E., Kanamitsu, M., Kistler, R., Collins, W., Deaven, D., Gandin, L., Iredell, M., Saha, S., White, G., Woollen, J., Zhu, Y., Chelliah, M., Ebisuzaki, W., Higgins, W., Janowiak, J., Mo, K. C., Ropelewski, C., Wang, J., Leetmaa, A., Reynolds, R., Jenne, R., and Joseph, D.: The NCEP/NCAR 40-year reanalysis project, B. Am. Meteorol. Soc., 77, 437–470, doi:10.1175/1520-0477(1996)077%3C0437:TNYRP%3E2.0.CO;2, 1996.

Kanakidou, M., Seinfeld, J. H., Pandis, S. N., Barnes, I., Dentener, F. J., Facchini, M. C., Van Dingenen, R., Ervens, B., Nenes, A., Nielsen, C. J., Swietlicki, E., Putaud, J. P., Balkanski, Y., Fuzzi, S., Horth, J., Moortgat, G. K., Winterhalter, R., Myhre, C. E. L., Tsigaridis, K., Vignati, E., Stephanou, E. G., and Wilson, J.: Organic aerosol and global climate modelling: a review, Atmos. Chem. Phys., 5, 1053–1123, doi:10.5194/acp-5-1053-2005, 2005.

Karl, M., Tsigaridis, K., Vignati, E., and Dentener, F.: Formation of secondary organic aerosol from isoprene oxidation over Europe, Atmos. Chem. Phys., 9, 7003–7030, doi:10.5194/acp-9-7003-2009, 2009.

Katzfey, J. J.: Simulation of extreme New Zealand precipitation events. Part I. Sensitivity of orography and resolution, Mon. Weather. Rev., 123, 737–754, doi:10.1175/1520-0493(1995)123<0737;SOENZP>2.0.CO;2, 1995.

Katzfey, J. J.: Simulation of extreme New Zealand precipitation events. Part II. Mechanisms of precipitation development, Mon. Weather Rev., 123, 755–775, doi:10.1175/1520-0493(1995)123<0755;SOENZP>2.0.CO;2, 1995.

Kelly, J. T., Bhave, P. V., Nolte, C. G., Shankar, U., and Foley, K. M.: Simulating emission and chemical evolution of coarse sea-salt particles in the Community Multiscale Air Quality (CMAQ) Model, Geosci. Model Dev., 3, 257–273, doi:10.5194/gmd-3-257-2010, 2010.

Kettle, A. J., and Andreae, M. O.: Flux of dimethylsulfide from the oceans: A comparison of updated data sets and flux models, J. Geophys. Res., 105, 26793–26808, 2000.

Kinne, S., Schulz, M., Textor, C., Guibert, S., Balkanski, Y., Bauer, S. E., Berntsen, T., Berglen, T. F., Boucher, O., Chin, M., Collins, W., Dentener, F., Diehl, T., Easter, R., Feichter, J., Fillmore, D., Ghan, S., Ginoux, P., Gong, S., Grini, A., Hendricks, J., Herzog, M., Horowitz, L., Isaksen, I., Iversen, T., Kirkevåg, A., Kloster, S., Koch, D., Kristjansson, J. E., Krol, M., Lauer, A., Lamarque, J. F., Lesins, G., Liu, X., Lohmann, U., Montanaro, V., Myhre, G., Penner, J., Pitari, G., Reddy, S., Seland, Ø., Stier, P., Takemura, T., and Tie, X.: An AeroCom initial assessment – optical properties in aerosol component modules of global models, Atmos. Chem. Phys., 6, 1815–1834, doi:10.5194/acp-6-1815-2006, 2006.

Kircher, C. C. and Sander, S. P.: Kinetics and mechanism of HO2 and DO2 disproportionations, J. Phys. Chem., 88, 2082–2091, 1984.

Kirkevåg, A., Iversen, T., Seland, Ø., Hoose, C., Kristjánsson, J. E., Struthers, H., Ekman, A. M. L., Ghan, S., Griesfeller, J., Nilsson, E. D., and Schulz, M.: Aerosolclimate interactions in the Norwegian Earth System Model – NorESM1-M, Geosci. Model Dev., 6, 207–244, doi:10.5194/gmd-6-207-2013, 2013.

Kloster, S., Feichter, J., Maier-Reimer, E., Six, K. D., Stier, P., and Wetzel, P.: DMS cycle in the marine ocean-atmosphere system - a global model study, Biogeosciences, 3, 1, 29–51, doi:10.5194/bg-3-29-2006, 2006.

Koch, D.: Transport and direct radiative forcing of carbonaceous and sulfate aerosols in the GISS GCM, J. Geophys. Res., 106, D17, 20311–20332, 2001.

Koch, D., Jacob, D., Tegen, I., Rind, D., and Chin, M.: Tropospheric sulfur simulation and sulfate direct radiative forcing in the Goddard Institute for Space Studies general circulation model, J. Geophys. Res., 104 (D19), 23799–23822, 1999.

Koch, D., Park, J., and Del Genio, A.: Clouds and sulfate are anticorrelated: A new diagnostic for global sulfur models, J. Geophys. Res., 108 (D24), 4781, doi:10.1029/2003JD003621, 2003.

Koch, D., Schmidt, G. A., and Field, C. V.: Sulfur, sea salt, and radionuclide aerosols in GISS ModelE, J. Geophys. Res.-Atmos., 111, D06206, doi:10.1029/2004jd005550, 2006.

Koch, D., Bond, T. C., Streets, D., Unger, N., and van der Werf, G. R.: Global impacts of aerosols from particular source regions and sectors, J. Geophys. Res.-Atmos., 112, D02205, doi:10.1029/2005jd007024, 2007.

Köepke, P., Hess, M., Schult, I., and Shettle, E. P.: Global aerosol dataset, report, Tech. rep., Max-Planck Institute für Meteorologie, Hamburg, Germany, 1997.

Köhler, H.: The nucleus in the growth of hygroscopic droplets, Transactions of the Faraday Society, 32, 1152–1161, 1936.

Kok, J. F., Parteli, E. J. R., Michaels, T. I., and Bou Karam, D.: The physics of wind-blown sand and dust, Rep. Prog. Phys., 75, 106901, 2012.

Lacis, A. A. and Hansen, J. E.: A parameterization for the absorption of solar radiation in the Earth's atmosphere, J. Atmos. Sci., 31, 118–133, 1974.

Koo, B., Knipping, E., and Yarwood, G.: 1.5–Dimensional volatily basis set approach for modeling organic aerosol in CAMx and CMAQ, Atmos. Env., 95, 158–164, doi:10.1016/j.atmosenv.2014.06.031, 2014.

Lamarque, J.-F., Bond, T. C., Eyring, V., Granier, C., Heil, A., Klimont, Z., Lee, D., Liousse, C., Mieville, A., Owen, B., Schultz, M. G., Shindell, D., Smith, S. J., Stehfest, E., Van Aardenne, J., Cooper, O. R., Kainuma, M., Mahowald, N., McConnell, J. R., Naik, V., Riahi, K., and van Vuuren, D. P.: Historical (1850–2000) gridded anthropogenic and biomass burning emissions of reactive gases and aerosols: methodology and application, Atmos. Chem. Phys., 10, 7017–7039, doi:10.5194/acp-10-7017-2010, 2010.

Lee, Y. H. and Adams, P. J.: Evaluation of aerosol distributions in the GISS-TOMAS global aerosol microphysics model with remote sensing observations, Atmos. Chem. Phys., 10, 2129–2144, doi:10.5194/acp-10-2129-2010, 2010.

Lee, Y. H. and Adams, P. J.: A Fast and Efficient Version of the TwO-Moment Aerosol Sectional (TOMAS) Global Aerosol Microphysics Model, Aerosol Sci. Tech., 46, 678–689, doi:10.1080/02786826.2011.643259, 2012.

Lee, Y. H., Lamarque, J.-F., Flanner, M. G., Jiao, C., Shindell, D. T., Berntsen, T., Bisiaux, M. M., Cao, J., Collins, W. J., Curran, M., Edwards, R., Faluvegi, G., Ghan, S., Horowitz, L. W., McConnell, J. R., Ming, J., Myhre, G., Nagashima, T., Naik, V., Rumbold, S. T., Skeie, R. B., Sudo, K., Takemura, T., Thevenon, F., Xu, B., and Yoon, J.-H.: Evaluation of preindustrial to present-day black carbon and its albedo forcing from Atmospheric Chemistry and Climate Model Intercomparison Project (ACCMIP), Atmos. Chem. Phys., 13, 2607–2634, doi:10.5194/acp-13-2607-2013, 2013.

Lee, Y. H., Adams, P. J., and Shindell, D. T.: ModelE2-TOMAS development and evaluation using aerosol optical depths, mass and number concentrations, Geosci. Model Dev. Discuss., 7, 5831–5918, doi:10.5194/gmdd-7-5831-2014, 2014.

Lewis, E. R. and Schwartz, S. E.: Sea Salt Aerosol Production: Mechanisms, Methods, Measurements, and Models, American Geophysical Union, Washington DC, 9–13, 2004.

Liao, H., Henze, D. K., Seinfeld, J. H., Wu, S. L., and Mickley, L. J.: Biogenic secondary organic aerosol over the United States: Comparison of climatological simulations with observations, J. Geophys.Res.-Atmos., 112, D06201, doi:10.1029/2006JD007813, 2007.

Lin, H. and Leaitch, R.: Development of an in-cloud aerosol activation parameterization for climate modelling, paper presented at Workshop on Measurements of Cloud Properties for Forecast of Weather, Air Quality and Climate, World Meteorological Society, Mexico City, 1997.

Lin, G., Penner, J. E., Sillman, S., Taraborrelli, D., and Lelieveld, J.: Global modeling of SOA formation from dicarbonyls, epoxides, organic nitrates and peroxides, Atmos. Chem. Phys., 12, 4743–4774, doi:10.5194/acp-12-4743-2012, 2012.

Lind, J. A. and Kok, G. L.: Correction to Henry's law determinations for aqueous solutions of hydrogen peroxide, methylhydroperoxide, and peroxyacetic acid, J. Geophys. Res., 99D, 21 119, 1994.

Liu, X., Penner, J. E., and Herzog, M.: Global simulation of aerosol dynamics: Model description, evaluation, and interactions between sulphate and nonsulphate aerosols, J. Geophys. Res., 110(D18), D18206, doi:10.1029/2004JD005674, 2005.

Liu, X., Easter, R. C., Ghan, S. J., Zaveri, R., Rasch, P., Shi, X., Lamarque, J.-F., Gettelman, A., Morrison, H., Vitt, F., Conley, A., Park, S., Neale, R., Hannay, C., Ekman, A. M. L., Hess, P., Mahowald, N., Collins,W., Iacono, M. J., Bretherton, C. S., Flanner, M. G., and Mitchell, D.: Toward a minimal representation of aerosols in climate models: description and evaluation in the Community Atmosphere Model CAM5, Geosci. Model Dev., 5, 709–739, doi:10.5194/gmd-5-709-2012, 2012.

Loosmore, G. A., and Cederwall, R. T.: Precipitation scavenging of atmospheric aerosols for emergency response applications: Testing an updated model with new real-time data, Atmos. Environ., 38, 993–1003, doi:10.1016/j.atmosenv.2003.10.055, 2014.

Mårtensson, E. M., Nilsson, E. D., de Leeuw, G., Cohen, L. H., and Hansson, H.-C.: Laboratory simulations and parameterization of the primary marine aerosol production, J. Geophys. Res., 108, 4297, doi:10.1029/2002JD002263, 2003.

Marticorena, B. and Bergametti, G.: Modeling the atmospheric dust cycle: 1. design of a soil-derived dust emission scheme, J. Geophys. Res., 100, 16415–16430, doi:10.1029/95JD00690, 1995.

Marticorena, B., Bergametti, G., Aumont, B., Callot, Y., N'Doume, C., and Legrand, M.: Modeling the atmospheric dust cycle 2. simulation of Saharan dust sources, J. Geophys. Res., 102, 4387–4404, doi:10.1029/96JD02964, 1997.

Martin, L. R. and Damschen, D. E.: Aqueous oxidation of sulfur dioxide by hydrogen peroxide at low pH, Atmos. Environ., 15, 1615–1621, 1981.

Martin, M. V., Logan, J. A., Kahn, R. A., Leung F.-Y., Nelson, D. L., and Diner, D. J.: Smoke injection heights from fires in North America: analysis of 5 years of satellite observations, Atmos. Chem. Phys, 10, 1–18, 2010.

Mayol-Bracero, O. L., Gabriel, R., Andreae, M. O., Kirchstetter, T. W., Novakov, T., Ogren, J., Sheridan, P., and Streets, D. G.: Carbonaceous aerosols over the Indian Ocean during the Indian Ocean Experiment (INDOEX): Chemical characterization, optical properties, and probable sources, J. Geophys. Res., 107, 8030, doi:10.1029/2000JD000039, 2002.

McCauley, M. P. and Sturman, A. P.: A study of orographic blocking and barrier wind development upstream of the Southern Alps, New Zealand, Meteorol. and Atmos. Phys., 70, 121–131, 1999.

Mellor, G. L. and Yamada, T.: Development of a turbulence closure model for geophysical fluid problems, Rev. Geophys. Space Phys., 20, 851–875, 1982.

Menut, L., Bessagnet, B., Khvorostyanov, D., Beekmann, M., Blond, N., Colette, A., Coll, I., Curci, G., Foret, G., Hodzic, A., Mailler, S., Meleux, F., Monge, J. L., Pison, I., Siour, G., Turquety, S., Valari, M., Vautard, R., and Vivanco, M. G.: CHIMERE 2013: a model for regional atmospheric composition modelling, Geosci. Model Dev., 6, 981–1028, doi:10.5194/gmd-6-981-2013, 2013.

Metzger, S. M., Dentener, F. J., Lelieveld, J., and Pandis, S. N.: Gas/aerosol partitioning: I. A computationally efficient model, J. Geophys. Res., 107, D16, doi:10.1029/2001JD001102, 2002.

Mishchenko, M. I., Travis, L. D., and Lacis, A. A.: Scattering, Absorption, and Emission of Light by Small Particles, Cambridge University Press, Cambridge, 2002.

Mitchell, D. L.: Paramtetrization of the Mie Extinction and Absorption Coefficients for Water Clouds, J. Atmos. Sci., 57, 1311–1326, 1999.

Mlawer, E. J., Taubman, S. J., Brown, P. D., Iacono, M. J., and Clough, S. A.: Radiative transfer for inhomogeneous atmosphere: RRTM, a validated correlated-k model for the longwave, J. Geophys. Res., 102, 16663–16682, 1997.

Monahan, E. C., Spiel, D. E., and Davidson, K. L.: A model of marine aerosol generation via whitecaps and wave disruption, in: Oceanic Whitecaps, edited by: Monahan, E. C. and Mac Niocaill, G., 167–174, D. Reidel, Norwell, Massachusetts, 1986.

Monin, A. S. and Obukhov, A. M.: Basic laws of turbulent mixing in the surface layer of the atmosphere, Contrib. Geophys. Inst. Acad. Sci. USSR, 151, 163–187, 1954 (in Russian).

Morcrette, J. J., Boucher, O., Jones, L., Salmond, D., Bechtold, P., Beljaars, A., Benedetti, A., Bonet, A., Kaiser, J. W., Razinger, M., Schulz, M., Serrar, S., Simmons, A. J., Sofiev, M., Suttie, M., Tompkins, A. M., and Untch, A.: Aerosol analysis and forecast in the European Centre for Medium-RangeWeather Forecasts Integrated Forecast System: Forward modeling, J. Geophys. Res.-Atmos., 114, D06206, doi:10.1029/2008jd011235, 2009.

Myhre, G., Berglen, T. F., Johnsrud, M., Hoyle, C. R., Berntsen, T. K., Christopher, S. A., Fahey, D. W., Isaksen, I. S. A., Jones, T. A., Kahn, R. A., Loeb, N., Quinn, P., Remer, L., Schwarz, J. P., and Yttri, K. E.: Modelled radiative forcing of the direct aerosol effect with multi-observation evaluation, Atmos. Chem. Phys., 9, 1365–1392, doi:10.5194/acp-9-1365-2009, 2009.

Myhre, G., Samset, B. H., Schulz, M., Balkanski, Y., Bauer, S., Berntsen, T. K., Bian, H., Bellouin, N., Chin, M., Diehl, T., Easter, R. C., Feichter, J., Ghan, S. J., Hauglustaine, D., Iversen, T., Kinne, S., Kirkevåg, A., Lamarque, J.-F., Lin, G., Liu, X., Lund, M. T., Luo, G., Ma, X., van Noije, T., Penner, J. E., Rasch, P. J., Ruiz, A., Seland, Ø., Skeie, R. B., Stier, P., Takemura, T., Tsigaridis, K., Wang, P., Wang, Z., Xu, L., Yu, H., Yu, F., Yoon, J.-H., Zhang, K., Zhang, H., and Zhou, C.: Radiative forcing of the direct aerosol effect from AeroCom Phase II simulations, Atmos. Chem. Phys., 13, 1853–1877, doi:10.5194/acp-13-1853-2013, 2013.

Nickovic, S., Vukovic, A., and Vujadinovic, M.: Atmospheric processing of iron carried by mineral dust, Atmos. Chem. Phys., 13, 9169–9181, doi:10.5194/acp-13-9169-2013, 2013.

O'Dowd, C. D. and de Leeuw, G.: Marine aerosol production: a review of the current knowledge, Philos. T. Roy. Soc. A, 365, 1753–1774, doi:10.1098/rsta.2007.2043, 2007.

Partanen, A.-I., Dunne, E. M., Bergman, T., Laakso, A., Kokkola, H., Ovadnevaite, J., Sogacheva, L., Baisnée, D., Sciare, J., Manders, A., O'Dowd, C., de Leeuw, J., and Korhonen, H.: Global modelling of direct and indirect effects of sea spray aerosol using a source function encapsulating wave state, Atmos. Chem. Phys., 14, 4537–4597, doi:10.5194/acp-14-4537-2014, 2014.

Peckham, S., Grell, G. A., McKeen, S. A., Barth, M., Pfister, G., Wiedinmyer, C., Fast, J. D., Gustafson, W. I., Zaveri, R., Easter, R. C., Barnard, J., Chapman, E., Hewson, M., Schmitz, R., Salzmann, M., and Freitas, S.: WRF/Chem Version 3.3 User's Guide, NOAA Technical Memo., 98pp., 2011.

Pérez, C., Nickovic, S., Pejanovic, G., Baldasano, J. M., and Özsoy, E.: Interactive dust-radiation modeling: a step to improve weather forecasts, J. Geophys. Res., 111, D16206, doi:10.1029/2005JD006717, 2006.

Pérez, C., Haustein, K., Janjic, Z., Jorba, O., Huneeus, N., Baldasano, J. M., Black, T., Basart, S., Nickovic, S., Miller, R. L., Perlwitz, J. P., Schulz, M., and Thomson, M.: Atmospheric dust modeling from meso to global scales with the online NMMB/BSC-Dust model – Part 1: Model description, annual simulations and evaluation, Atmos. Chem. Phys., 11, 13001–13027, doi:10.5194/acp-11-13001-2011, 2011.

Perlwitz, J. P. and Pérez García-Pando, C. and Miller, R. L.: Predicting the mineral composition of dust aerosols – Part 1: Representing key processes, Atmos. Chem. Phys. Discuss., 15, 3493–3575, doi:10.5194/acpd-15-3493-2015, 2015.

Petelski, T., Piskozub, J., and Paplinska-Swerpel, B.: Sea spray emission from the surface of the open Baltic Sea, J. Geophys. Res., 110, C10023, doi:10.1029/2004JC002800, 2005.

Presto, A. A., Huff Hartz, K.E., and Donahue, N.M.: Secondary organic aerosol production from terpene ozonolysis. 2. Effect of NOx concentration. Env. Sci. and Tech., 39, 7046–7054, 2005.

Prospero, J. M., Landing, W. M., and Schulz, M.: African dust deposition to Florida: Temporal and spatial variability and comparisons to models, J. Geophys. Res. Atmos., 115, D13304, doi:10.1029/2009JD012773, 2010.

Quinn, P. K. and Bates, T. S.: Regional aerosol properties: Comparisons of boundary layer measurements from ACE1, ACE2, aerosols99, INDOEX, ACE asia, TARFOX, and NEAQS, J. Geophys. Res., 110, D14202, doi:10.1029/2004JD004755, 2005.

Quinn, P. K., Coffman, D. J., Kapustin, V. N., Bates, T. S., and Covert, D. S.: Aerosol optical properties in the marine boundary layer during the First Aerosol Characterization Experiment (ACE1) and the underlying chemical and physical aerosol properties, J. Geophys. Res., 103, 16547–16563, 1998.

Reid, J. S., Jonsson, H. H., Smith, M. H., and Smirnov, A.: Evolution of the vertical profile and flux of large sea-salt particles in a coastal zone, J. Geophys. Res., 34, 12039–12053, 2001.

Revell, M. J. and Copeland, J. H. and Larsen, H. R. and Wratt, D. S.: Barrier jets around the Southern Alps of New Zealand and their potential to enhance alpine rainfall, Atmos. Res., 61, 277–298, doi:10.1016/S0160-8095(01)00142-9, 2002.

Ridley, D. A. and Heald, C. L. and Pierce, J. R. and Evans, M. J.: Toward resolution-independent dust emissions in global models: Impacts on the seasonal and spatial distribution of dust, Geophys. Res. Lett., 40, 2873–2877, doi:10.1002/grl.50409, 2013.

Rieger, D., Bangert, M., Bischoff-Gauss, I., Förstner, J., Lundgren, K., Reinert, D., Schröter, J., Vogel, H., Zängl, G., Ruhnke, R., and Vogel, B.: ICON-ART 1.0 – a new online-coupled model system from the global to regional scale, Geosci. Model Dev., 8, 1659–1676, doi:10.5194/gmd-8-1659-2015, 2015.

Roe, G. H.: Orographic Precipitation, Ann. Rev. Earth and Planet. Sci., 33, 645–671, doi:10.1146/annurev.earth.33.092203.122541, 2005.

Roselle, S. J. and Binkowski, F. S.: Cloud Dynamics and Chemistry, in Science algorithms of the EPA Models-3 community multiscale air quality (CMAQ) modeling system, edited by D. W. Byun and J. K. S. Ching, Rep. EPA/600/R-99, 30, Research Triangle Park, NC, 1999.

Rotstayn, L. D., and Lohmann, U.: Simulation of the tropospheric sulfur cycle in a global model with a physically based cloud scheme, J. Geophys. Res., 107(D21), 4592, doi:10.1029/2002JD002128, 2002.

Rouault, M. and Mélice, J.-L. and Reason, C. J. C. and Lutjeharms, T. R. E.: Climate variability at Marion Island, Southern Ocean, since 1960, J. Geophys. Res., 110, C05007, doi:10.1029/2004JC002492, 2005.

Russell, A. and Dennis, R.: NARSTO critical review of photochemical models and modeling, Atmos. Env., 34, 2283–2324, 2000.

Sander, R.: Compilation of Henry's Law Constants for Inorganic and Organic Species of Potential Importance in Environmental Chemistry, Version 3.0, `http://www.mpch-mainz.mpg.de/~sander/res/henry.html`, 1999.

Sander, S. P., Friedl, R. R., Golden, D. M., Kurylo, M. J., Moortgat, G. K., Keller-Rudek, H., Wine, P. H., Ravishankara, A. R., Kolb, C. E., Molina, M. J., Finlayson-Pitts, B. J.,

Huie, R. E., and Orkin, V. L.: Chemical Kinetics and Photochemical Data for Use in Atmospheric Studies, Evaluation Number 15, JPL Publication 06-2, Jet Propulsion Laboratory, Pasadena, CA, 2006.

Sander, R., Baumgaertner, A., Gromov, S., Harder, H., Jöckel, P., Kerkweg, A., Kubistin, D., Regelin, E., Riede, H., Sandu, A., Taraborrelli, D., Tost, H., and Xie, Z.-Q.: The atmospheric chemistry box model CAABA/MECCA-3.0, Geosci. Model Dev., 4, 373–380, doi:10.5194/gmd-4-373-2011, 2011.

Sandwell, D. T. and Agreen, R. W.: Seasonal variation in wind speed and sea state from global satellite measurements, J. Geophys. Res., 89, 2041–2051, 1984.

Savoie, D. L. and Prospero, J. M.: Aerosol concentration statistics for the Northern Tropical Atlantic, J. Geophys. Res., 82, 5954–5964, doi:10.1029/JC082i037p05954, 1977.

Sayer, A. M., Munchak, L. A., Hsu, N. C., Levy, R. C., Bettenhausen, C., and Jeong, M.-J.: MODIS Collection 6 aerosol products: Comparison between Aqua's e-Deep Blue, Dark Target, and "merged" data sets, and usage recommendations, J. Geophys. Res. Atmos., 119, 13965–13989, doi:10.1002/2014JD022453, 2014.

Schultz, M. G., Backman, L., Balkanski, Y., Bjoerndalsaeter, S., Brand, R., Burrows, J. P., Dalsoeren, S., de Vasconcelos, M., Grodtmann, B., Haughustaine, D. A., Heil, A., Hoelzemann, J. J., Isaksen, I. S. A., Kaurola, J., Knorr, W., Ladstaetter-Weißenmayer, A., Mota, B., Oom, D., Pacyna, J., Panasiuk, D., Pereira, J. M. C., Pulles, T., Pyle, J., Rast, S., Richter, A., Savage, N., Schnadt, C., Schulz, M., Spessa, A., Staehelin, J., Sundet, J. K., Szopa, S., Thonicke, K., van het Bolscher, M., van Noije, T., van Velthoven, P., Vik, A. F., andWittrock, F.: REanalysis of the TROpospheric chemical composition over the past 40 years (RETRO) A long-term global modeling study of tropospheric chemistry, Final Report, Jülich/Hamburg, Germany, 2007 (Published as report no. 48/2007 in the series Reports on Earth System Science of the Max Planck Institute for Meteorology, Hamburg, ISSN 1614-1199), 2007.

Schulz, M., Prospero, J. M., Baker, A. R., Dentener, F., Ickes, L., Liss, P. S., Mahowald, N. M., Nickovic, S., Pérez García-Pando, C., Rodríguez, S., Sarin, M., Tegen, I., and Duce, R. A.: Atmospheric Transport and Deposition of Mineral Dust to the Ocean: Implications for Research Needs, Environ. Sci. Technol., 46 (19), 10390–10404, doi:10.1021/es300073u, 2012.

Seaman, N. L.: Meteorological Modeling for Air-Quality Assessments: A NARSTO Review, Atmos. Env., 34, 2231–2260, 1998.

Sessions, W. R., Reid, J. S., Benedetti, A., Colarco, P. R., da Silva, A., Lu, S., Sekiyama, T., Tanaka, T. Y., Baldasano, J. M., Basart, S., Brooks, M. E., Eck, T. F., Iredell, M., Hansen, J. A., Jorba, O. C., Juang, H.-M. H., Lynch, P., Morcrette, J.-J., Moorthi, S., Mulcahy, J., Pradhan, Y., Razinger, M., Sampson, C. B., Wang, J., and Westphal, D. L.: Development towards a global operational aerosol consensus: basic climatological characteristics of the International Cooperative for Aerosol Prediction Multi-Model Ensemble (ICAP-MME), Atmos. Chem. Phys., 15, 335–362, doi:10.5194/acp-15-335-2015, 2015.

Shao, Y. P.: Physics and Modelling of Wind Erosion, 2nd ed. (Heidelberg: Springer), 2008.

Shindell, D. T., Lamarque, J.-F., Schulz, M., Flanner, M., Jiao, C., Chin, M., Young, P. J., Lee, Y. H., Rotstayn, L., Mahowald, N., Milly, G., Faluvegi, G., Balkanski, Y., Collins, W. J., Conley, A. J., Dalsoren, S., Easter, R., Ghan, S., Horowitz, L., Liu, X., Myhre, G., Nagashima, T., Naik, V., Rumbold, S. T., Skeie, R., Sudo, K., Szopa, S., Takemura, T., Voulgarakis, A., Yoon, J.-H., and Lo, F.: Radiative forcing in the ACCMIP historical and future climate simulations, Atmos. Chem. Phys., 13, 2939–2974, doi:10.5194/acp-13-2939-2013, 2013.

Simmons, A. J. and Burridge, D. M.: An energy and angular momentum conserving vertical finite-difference scheme and hybrid vertical coordinates, Mon. Weather Rev., 109, 758–766, 1981.

Sinclair, M.R. and Wratt, D. S. and Henderson, R. D. and Gray, W. R.: Factors affecting the distribution and spillover of precipitation in the Southern Alps of New Zealand a case study, J. Appl. Meteorol., 36, 428–442, doi:10.1175/1520-0450(1997)036<0428:FATDAS>2.0.CO;2, 1997.

Slinn, W. G. N.: Predictions for particle deposition to vegetative canopies, Atmos. Environ., 16, 1785–1794, 1982.

Slinn, W. G. N.: Precipitation scavenging, in: Atmospheric Science and Power Production, edited by: Randerson, D., 466–532, OSTI, Oak Ridge, 1984.

Slinn, W. G. N., Hasse, L., Hicks, B. B., Hogan, A. W., Lal, D., Liss, P. S., Munnich, K. O., Sehmel, G. A., and Vittori, O.: Some aspects of the transfer of atmospheric trace constituents past the air-sea surface, Atmos. Env., 12, 2055–2087, 1978.

Smirnov, A., Holben, B. N., Eck, T. F., Dubovik, O., and Slutsker, I.: Cloud screening and quality control algorithms for the AERONET data-base, Remote Sens. Environ., 73, 337–349, doi:10.1016/S0034-4257(00)00109-7, 2000.

Smirnov, A., Holben, B. N., Giles, D. M., Slutsker, I., O'Neill, N. T., Eck, T. F., Macke, A., Croot, P., Courcoux, Y., Sakerin, S. M., Smyth, T. J., Zielinski, T., Zibordi, G., Goes, J. I., Harvey, M. J., Quinn, P. K., Nelson, N. B., Radionov, V. F., Duarte, C. M., Losno, R., Sciare, J., Voss, K. J., Kinne, S., Nalli, N. R., Joseph, E., Krishna Moorthy, K., Covert, D. S., Gulev, S. K., Milinevsky, G., Larouche, P., Belanger, S., Horne, E., Chin, M., Remer, L. A., Kahn, R. A., Reid, J. S., Schulz, M., Heald, C. L., Zhang, J., Lapina, K., Kleidman, R. G., Griesfeller, J., Gaitley, B. J., Tan, Q., and Diehl, T. L.: Maritime aerosol network as a component of AERONET – first results and comparison with global aerosol models and satellite retrievals, Atmos. Meas. Tech., 4, 583–597, doi:10.5194/amt-4-583-2011, 2011.

Smith, M. H. and Harrison, N. M.: The sea spray generation function, J. Atmos. Sci., 29, 189–190, 1998.

Smith, M. H., Park, P. M., and Consterdine, I. E.: Marine aerosol concentrations and estimated fluxes over the sea, Q. J. Roy. Meteor. Soc., 809–824, 1993.

Soares, J., Sofiev, M., and Hakkarainen, J.: Uncertainties of wild-land fires emission in AQMEII phase 2 case study, Atmos. Env., in press, 1–10, doi:10.1016/j.atmosenv.2015.01.068, 2015.

Sofiev, M., Ermakova, T., and Vankevich, R.: Evaluation of the smoke-injection height from wild-land fires using remote-sensing data, Atmos. Chem. Phys., 12, 1995–2006, doi:10.5194/acp-12-1995-2012, 2012.

Solazzo, E., Bianconi, R., Pirovano, G., Matthias, V., Vautard, R., Moran, M. D., Appel, K. W., Bessagnet, B., Brandt, J., Christensen, J. H., Chemel, C., Coll, I., Ferreira, J., Forkel, R., Francis, X. V., Grell, G., Grossi, P., Hansen, A. B., Miranda, A. I., Nopmongcol, U., Prank, M., Sartelet, K. N., Schaap, M., Silver, J. D., Sokhi, R. S., Vira, J., Werhahn, J., Wolke, R., Yarwood, G., Zhang, J., Rao, S. T., Galmarini, S.: Operational model evaluation for particulate matter in Europe and North America in the context of AQMEII, Atmos. Env., 53, 75–92, doi:10.1016/j.atmosenv.2012.02.045, 2012.

Spada, M., Jorba, O., Pérez García-Pando, C., Janjic, Z., and Baldasano, J. M.: Modeling and evaluation of the global sea-salt aerosol distribution: sensitivity to size-resolved and sea-surface temperature dependent emission schemes, Atmos. Chem. Phys., 13, 11735–11755, doi:10.5194/acp-13-11735-2013, 2013.

Spada, M., Jorba, O., Pérez García-Pando, C., Janjic, Z., and Baldasano, J. M.: On the evaluation of global sea-salt aerosol models at coastal/orographic sites, Atmos. Env., 101, 41–48, doi:10.1016/j.atmosenv.2014.11.019, 2015.

Staudinger, J. and Roberts, P. V.: A critical compilation of Henry's law constant temperature dependence relations for organic compounds in dilute aqueous solutions, Chemosphere, 44, 561–576, 2001.

Stier, P., Feichter, J., Kinne, S., Kloster, S., Vignati, E., Wilson, J., Ganzeveld, L., Tegen, I., Werner, M., Balkanski, Y., Schulz, M., Boucher, O., Minikin, A., and Petzold, A.: The aerosol-climate model ECHAM5-HAM, Atmos. Chem. Phys., 5, 1125–1156, doi:10.5194/acp-5-1125-2005, 2005.

Takemura, T., Okamoto, H., Maruyama, Y., Numaguti, A., Higurashi, A., and Nakajima, T.: Global three-dimensional simulation of aerosol optical thickness distribution of various origins, J. Geophys. Res.-Atmos., 105, 17853–17873, 2000.

Takemura, T., Uno, I., Nakajima, T., Higurashi, A., and Sano, I.: Modeling study of long-range transport of Asian dust and anthropogenic aerosols from East Asia, Geophys. Res. Lett., 29, 2158–2158, 2002.

Takemura, T., Nozawa, T., Emori, S., Nakajima, T. Y., and Nakajima, T.: Simulation of climate response to aerosol direct and indirect effects with aerosol transport-radiation model, J. Geophys. Res.-Atmos., 110, D02202, doi:10.1029/2004jd005029, 2005.

Takemura, T., Egashira, M., Matsuzawa, K., Ichijo, H., Oishi, R., and Abe-Ouchi, A.: A simulation of the global distribution and radiative forcing of soil dust aerosols at the Last Glacial Maximum, Atmos. Chem. Phys., 9, 3061–3073, doi:10.5194/acp-9-3061-2009, 2009.

Textor, C., Schulz, M., Guibert, S., Kinne, S., Balkanski, Y., Bauer, S., Berntsen, T., Berglen, T., Boucher, O., Chin, M., Dentener, F., Diehl, T., Easter, R., Feichter, H., Fillmore, D., Ghan, S., Ginoux, P., Gong, S., Grini, A., Hendricks, J., Horowitz, L., Huang, P., Isaksen, I., Iversen, I., Kloster, S., Koch, D., Kirkevåg, A., Kristjansson, J. E., Krol, M.,

Lauer, A., Lamarque, J. F., Liu, X., Montanaro, V., Myhre, G., Penner, J., Pitari, G., Reddy, S., Seland, Ø., Stier, P., Takemura, T., and Tie, X.: Analysis and quantification of the diversities of aerosol life cycles within AeroCom, Atmos. Chem. Phys., 6, 1777–1813, doi:10.5194/acp-6-1777-2006, 2006.

Textor, C., Schulz, M., Guibert, S., Kinne, S., Balkanski, Y., Bauer, S., Berntsen, T., Berglen, T., Boucher, O., Chin, M., Dentener, F., Diehl, T., Feichter, J., Fillmore, D., Ginoux, P., Gong, S., Grini, A., Hendricks, J., Horowitz, L., Huang, P., Isaksen, I. S. A., Iversen, T., Kloster, S., Koch, D., Kirkevåg, A., Kristjansson, J. E., Krol, M., Lauer, A., Lamarque, J. F., Liu, X., Montanaro, V., Myhre, G., Penner, J. E., Pitari, G., Reddy, M. S., Seland, Ø., Stier, P., Takemura, T., and Tie, X.: The effect of harmonized emissions on aerosol properties in global models – an AeroCom experiment, Atmos. Chem. Phys., 7, 4489–4501, doi:10.5194/acp-7-4489-2007, 2007.

Tie, X., Brasseur, G., and Emmons, L.: Effects of aerosols on tropospheric oxidants: A global model study, J. Geophys. Res., 106 (D19), 22931–22964, 2001.

Tørseth, K., Aas, W., Breivik, K., Fjæraa, A. M., Fiebig, M., Hjellbrekke, A. G., Myhre, C., Solberg, S., and Yttri, K. E.: Introduction to the European Monitoring and Evaluation Programme (EMEP) and observed atmospheric composition change during 1972–2009, Atmos. Chem. Phys., 12, 5447–5481, doi:10.5194/acp-12-5447-2012, 2012.

Tsigaridis, K. and Kanakidou, M.: Secondary organic aerosol importance in the future atmosphere, Atmos. Env., 41 4682–4692, , doi:10.1016/j.atmosenv.2007.03.045, 2007.

Tsigaridis, K., Koch, D., and Menon, S.: Uncertainties and importance of sea spray composition on aerosol direct and indirect effects, J. Geophys. Res., 118, 220–235, doi:10.1029/2012JD018165, 2013.

Tsigaridis, K., Daskalakis, N., Kanakidou, M., Adams, P. J., Artaxo, P., Bahadur, R., Balkanski, Y., Bauer, S. E., Bellouin, N., Benedetti, A., Bergman, T., Berntsen, T. K., Beukes, J. P., Bian, H., Carslaw, K. S., Chin, M., Curci, G., Diehl, T., Easter, R. C., Ghan, S. J., Gong, S. L., Hodzic, A., Hoyle, C. R., Iversen, T., Jathar, S., Jimenez, J. L., Kaiser, J. W., Kirkevåg, A., Koch, D., Kokkola, H., Lee, Y. H, Lin, G., Liu, X., Luo, G., Ma, X., Mann, G. W., Mihalopoulos, N., Morcrette, J.-J., Müller, J.-F., Myhre, G., Myriokefalitakis, S., Ng, N. L., O'Donnell, D., Penner, J. E., Pozzoli, L., Pringle, K. J., Russell, L. M., Schulz, M., Sciare, J., Seland, Ø., Shindell, D. T., Sillman, S., Skeie, R. B., Spracklen, D., Stavrakou, T., Steenrod, S. D., Takemura, T., Tiitta, P., Tilmes, S., Tost, H., van Noije, T., van Zyl, P. G., von Salzen, K., Yu, F., Wang, Z., Wang, Z., Zaveri, R. A., Zhang, H., Zhang, K., Zhang, Q., and Zhang, X.: The AeroCom evaluation and intercomparison of organic aerosol in global models, Atmos. Chem. Phys., 14, 10845–10895, doi:10.5194/acp-14-10845-2014, 2014.

Tsyro, S., Aas, W., Soares, J., Sofiev, M., Berge, H., and Spindler, G.: Modelling of sea salt concentrations over Europe: key uncertainties and comparison with observations, Atmos. Chem. Phys., 11, 10367–10388, doi:10.5194/acp-11-10367-2011, 2011.

Turpin, B. J. and Lim, H. J.: Species contributions to PM2.5 mass concentrations: Revisiting common assumptions for estimating organic mass, Aerosol Sci. Tech., 35, 602–610, doi:10.1080/02786820152051454, 2001.

van Noije, T. P. C., Le Sager, P., Segers, A. J., van Velthoven, P. F. J., Krol, M. C., and Hazeleger, W.: Simulation of tropospheric chemistry and aerosols with the climate model EC-Earth, Geosci. Model Dev. Discuss., 7, 1933–2006, doi:10.5194/gmdd-7-1933-2014, 2014.

Vignati, E., Wilson, J., and Stier, P.: M7: a size resolved aerosol mixture module for the use in global aerosol models, J. Geophys. Res., 109, D22202, doi:10.1029/2003JD004485, 2004.

Wang, W. and Seaman, N. L.: A comparison study of convective parameterization schemes in a mesoscale model, Mon. Weather Rev., 125, 252-278, 1997.

Wang, M., S. Ghan, R. Easter, M. Ovchinnikov, X. Liu, E. Kassianov, Y. Qian, W.I. Gustafson, V.E. Larson, D.P. Schanen, M. Khairoutdinov, and H. Morrison, 2011: The multi-scale aerosol-climate model PNNL-MMF: Model description and evaluation. Geosci. Mod. Dev., 4, 137–168, doi:10.5194/gmd-4-137-2011, 2011.

Wesely, M.: Parameterization of surface resistances to gaseous dry deposition in regional-scale numerical models, Atmospheric Environment, 23 (6), 1293–1304, 1989.

Witek, M. L., Flatau, P. J., Quinn, P. K., and Westphal, D. L.: Global sea-salt modeling: results and validation against multicampaign shipboard measurements, J. Geophys. Res., 112, D08215, doi:10.1029/2006JD007779, 2007.

Witek, M. L., Flatau, P. J., Teixeira, J., and Markowicz, K. M.: Numerical investigation of sea salt aerosol size bin partitioning in global transport models: implications for mass budget and optical depth, Aerosol Sci. Tech., 45, 401–414, doi:10.1080/02786826.2010.541957, 2011.

Wratt, D. S. and Revell, M. J. and Sinclair, M. R. and Gray, W. R. and Henderson, R. D. and Chater, A. M.: Relationships between air mass properties and mesoscale rainfall in New Zealands Southern Alps, Atmos. Res., 52, 261–282, 2000.

Wratt, D. S. and Tait, A. and Griffiths, G. and Espie, P. and Jessen, M. and Keys, J. and Ladd, M. and Lew, D. and Lowther, N. and Mitchell, N. and Morton, J. and Reid, J. and Reid, S. and Richardson, A. and Sansom, J. and Shankar, U.: Climate for crops: integrating climate data with information about soils and crop requirements to reduce risks in agricultural decision-making, Meteorol. Appl., 13, 305–315, doi:10.1017/S1350482706002416, 2006.

Zakey, A. S., Solmon, F., and Giorgi, F.: Implementation and testing of a desert dust module in a regional climate model, Atmos. Chem. Phys., 6, 4687–4704, doi:10.5194/acp-6-4687-2006, 2006.

Zender, C. S., Bian, H., and Newman, D.: Mineral dust entrainment and deposition (DEAD) model: description and 1990s dust climatology, J. Geophys. Res., 108, 4416, doi:10.1029/2002JD002775, 2003.

Zhang, Y.: Impact of aerosol size representation on modeling aerosol-cloud interactions, J. Geophys. Res., 107 (D21), 4558, doi:10.1029/2001JD001549, 2002.

Zhang, Y.: Online-coupled meteorology an chemistry models: history, current status and outlook, Atmos. Chem. Phys., 8, 2895–2932, 2008.

Zhang, J. and Reid, J. S.: MODIS Aerosol product analysis for data assimilation: assessment of level 2 aerosol optical thickness retrievals, J. Geophys. Res., 111, D22207, doi:10.1029/2005JD006898, 2006.

Zhang, Y., Seigneur, C., Seinferld, J. H., Jacobson, M. Z., and Binkowski, F. S.: Simulation of Aerosol Dynamics: A Comparative Review of Algorithms Used in Air Quality Models, Aero. Sci. Tech., 31, 487–514, 1999.

Zhang, L., Gong, S., Padro, J., and Barrie, L.: A size-segregated particle dry deposition scheme for an atmospheric aerosol module, Atmos. Environ., 35, 549–560, 2001.

Zhang, H., Wang, Z., Wang, Z., Liu, Q., Gong, S., Zhang, X., Shen, Z., Lu, P., Wei, X., Che, H., and Li, L.: Simulation of direct radiative forcing of aerosols and their effects on East Asian climate using an interactive AGCM-aerosol coupled system, Clim. Dynam., 38, 1675–1693, doi:10.1007/s00382-011-1131-0, 2012.

Zhang, K., ODonnell, D., Kazil, J., Stier, P., Kinne, S., Lohmann, U., Ferrachat, S., Croft, B., Quaas, J., Wan, H., Rast, S., and Feichter, J.: The global aerosol-climate model ECHAM-HAM, version 2: sensitivity to improvements in process representations, Atmos. Chem. Phys., 12, 8911–8949, doi:10.5194/acp-12-8911-2012, 2012.

Zhang, Y., Karamchandani, P., Glotfelty, T., Streets, D. G., Grell, G., Nenes, A., Yu, F.-Q., and Bennartz, R.: Development and Initial Application of the Global-Through-Urban Weather Research and Forecasting Model with Chemistry (GU-WRF/Chem), J. Geophys. Res., 117, D20206, doi:10.1029/2012JD017966, 2012.

Zilitinkevich, S. S.: Bulk characteristics of turbulence in the atmospheric planetary boundary layer, Trudy GGO, 167, 49–52, 1965.